Synthesis and Catalytic Applications of Mesoporous Metal Oxides

Quanchang Li

Anorganisch-chemisches Institut Technische Universität München

Synthesis and Catalytic Applications of Mesoporous Metal Oxides

Quanchang Li

Vollständiger Abdruck der Fakultät für Chemie der Technischen Universität München zur

Erlangung des akademischen Grades eines

Doktors der Naturwissenschaften

genehmigten Dissertation.

Vorsitzender: Univ.-Prof. Dr. K. Köhler

Prüfer der Dissertation   1.   Priv.-Doz. Dr. P. Härter

                           2.   Univ.-Prof. Dr. J. A. Lercher

Die Dissertation wurde am 29.05.2001 bei der Technischen Universität München eingereicht

und durch die Fakultät für Chemie am 26.06.2001 angenommen.

Synthesis and Catalytic Applications of Mesoporous Metal Oxides

Quanchang Li

Die vorliegen Arbeit entstand der Zeit von Jan. 1999 bis Juli 2001 am Anorganisch-chemischen Institut der Technischen Universität München.

I would like to express my deep gratitude to my academic supervisors

Prof. Dr. Dr. h.c. mult. Wolfgang A. Herrmann

and

Priv.-Doz. Dr. P. Härter

For the advice and the continuous support of my work.

To Wen-Mei

With deep love and gratitude

Acknowledgements

I would like to express my sincere gratitude to Prof. Dr. Wolfgang A. Herrmann for giving me the opportunity to work in his group. Also my heartfelt gratitude goes to Dr. Peter Härter for his supervision, guidance and help throughout the course of my research work and for his valuable comments on this thesis.

I sincerely appreciate the generous help of Dr. Fritz E. Kühn in every respect to my family and me.

Mr. Markus Gitter is gratefully acknowledged for the fruitful co-operation in the project of catalytic dehydrogenation of benzyl alcohol. Dr. Julius A. Nickl in GWP company is acknowledged for the co-operation in catalytic $DeNO_x$. Prof. Dr. Klaus Köhler is acknowledged for introduction in TGA and DSC measurements. Dr. Gabriele Raudaschl-Sieber is acknowledged for the help in ^{31}P MAS NMR measurements and discussions in chemistry. Mr. M. Barth and his team are greatly acknowledged for the excellent elemental analysis service. Dr. Horst Schneider and Dr. Markus Widenmeyer are specially acknowledged for the patient help in BET measurement and discussions in chemistry. Mr. Klaus Lehmbacher, my lab-mate, and Mr. Jens Scheidel are acknowledged for the friendship and their help with our life in Munich.

Dr. Michelle Groarke is deeply appreciated for proof reading this thesis. Dr. Paula C. Ferreira is appreciated for the helpful suggestions and discussions in solid state chemistry. To both of them I would like to thank for their loyal friendship with my family.

Mrs. Irmgard Grötsch, Mrs. Renate Schuhbauer-Gerl, Mrs. Maria Huber and Mrs. Roswitha Kaufmann in the secretary's office are acknowledged for their help with organisations and bureaucratic matters.

I wish to express my thanks to all the members of Prof. Dr. Wolfgang A. Herrmann's group for their cooperativeness, as well as to all the people that in some way contributed to this thesis.

My wife, Wen-Mei, is appreciated for not only her help with chemistry but also her unconditional love and support throughout the years. Sorry to David, my son, that I didn't have enough time to spend with you as I would have liked.

Finally I would like to thank my parents for their understanding and encouragement despite going through serious health problems. I hope this thesis will comfort and cheer my mother who is still on her sick bed at present.

Abbreciations

ana	anatase
BET	Brunauer, Emmett and Teller
BJH	Barrett-Joyner-Halenda
CMC	critical micelle concentration
$DeNO_x$	decomposition of nitrogen oxides
EA	elemental analysis
EDTA	ethylenediaminetetraacetic acid
FTIR	Fourier transform infrared spectroscopy
GC	gas chromatography
HC-SCR	hydrocarbon-selective catalytic reduction
LC	liquid crystal
LCT	liquid crystal templating
meso	mesoporous
MS	mass spectroscopy
NMR	nuclear magnetic resonance
ppm	parts per million
RT	room temperature
TBHP	*tert*-butyl hydroperoxide
TEM	transmission electron microscopy
TEOS	tetraethylorthosilicate
TGA	thermogravimetric analysis
TMOS	tetramethylorthosilicate
wt.	weight
XRD	X-ray diffraction

Contents

Chapter 1. Introduction and Objectives

Research in supramolecular-templated mesoporous materials began in the early 1990s with the announcement of MCM-41 and the M41S family of molecular sieves by the researchers at Mobil Research and Development Corporation.[1,2] These materials are highly unusual in their textural characteristics: well-defined pore sizes of 15 – 100 Å, high surface areas in excess of 1000 m^2g^{-1}, and long-range ordering of the packing of pores. The unique physical properties of MCM-41 and its derivatives have made these materials highly desirable for catalytic applications. The extremely high surface areas are conductive to high catalytic activity. The large pore size (relative to that of microporous zeolites) allows for the fixation of large active complexes, reduces diffusional restriction of reactants, and enables reactions involving bulky molecules to take place. Many researchers have been involved in this field, particularly in modifying synthetic techniques, elucidating the mechanisms of mesostructure formation, extending to transition metal oxide analogues, and exploring their applications, etc. Various aspects of M41S and related mesoporous materials have been reviewed by Brinker (recent advances in porous inorganic materials),[3] Vartuli et al. (synthesis of the M41S family),[4] Stucky et al. (biomimetic synthesis of mesoporous materials),[5] Raman et al. (porous silicates templated by surfactants and organosilicate precursors),[6] Antonelli et al. (mesoporous transition metal oxide (TMS) family),[7] Behrens (mesoporous transition metal oxides),[8] Zhao et al. (aluminosilicate MCM-41),[9] Sayari (catalytic applications of MCM-41),[10] Schüth et al. (ordered mesoporous materials)[11] and Ying et al. (synthesis and applications of supramolecular-templated mesoporous materials).[12]

Our specific interest in this field is focused on mesoporous titanium oxide, zirconium oxide and aluminum oxide, as well as their applications in catalysis.

1.1. Mesoporous Molecular Sieves

Porous solids are traditionally used as adsorbents, catalysts and catalyst supports owing to their high surface areas and selective framework. According to the IUPAC definition,[13] porous materials are divided into three classes: microporous (< 2 nm), mesoporous (2 - 50 nm) and macroporous (> 50 nm) materials. Examples of these porous materials are presented in Table 1.1.[14] Zeolites are important and well-known members of the microporous class. These materials exhibit excellent catalytic properties by virtue of their crystalline aluminosilicate network. However, their applications are limited by the relatively small pore openings. Thus pore enlargement is one of the main aims in zeolite chemistry. Larger pores are found in porous glasses and porous gels, which were known as mesoporous materials at the time of the discovery of MCM-41.[1] The extremely high surface areas (> 1000 $m^2 g^{-1}$) and the precise tuning of pore sizes are among many of the desirable properties that have made

Table 1.1 Pore-size regimes and representative porous inorganic materials.[14]

Pore-size regimes	Definition	Examples	Actual size range
macroporous	> 500 Å	glasses	> 500 Å
mesoporous	20-500 Å	aerogels	> 100 Å
		pillared layered clays	10 Å, 100 Å[a]
		M41S	16-100 Å
microporous	< 20 Å	zeolites, zeotypes	< 14.2 Å
		activated carbon	6 Å

[a] Bimodal pore-size distribution.

such materials the focus of great interest. The family of molecular sieves M41S also ushered in a new approach in materials synthesis, where, instead of using single molecules as templating agents, as in the case of zeolites, self-assembled molecular aggregates and supramolecular assemblies are employed as the structure-directing agents.

1.1.1. Characterization

Reliable characterization of porous structures requires the use of three independent techniques: X-ray diffraction (XRD), transmission electron microscopy (TEM) and adsorption analysis (BET method).[15]
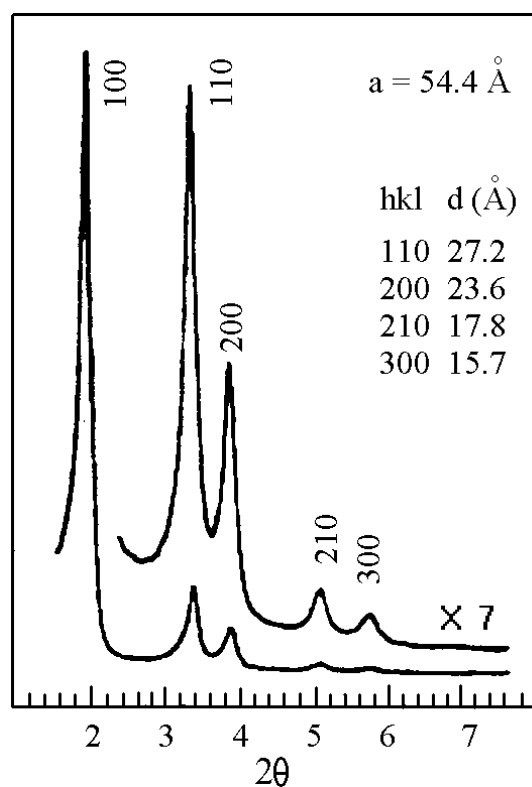
Figure 1.1 X-ray diffraction pattern of a high-quality calcined MCM-41 reported by Huo et al.[19]

The typical XRD pattern of MCM-41 shows three to five reflections between $2\theta = 2°$ and 5° (Fig. 1.1), although samples with more reflections have also been reported.[16,17] The reflections are due to the ordered hexagonal array of parallel silica tubes, and they can be indexed assuming a hexagonal unit cell as (100), (110), (200), (210) and (300). Since the materials are not crystalline at the atomic level, no reflections at higher angles are observed. These reflections would only be very weak in any case, owing to a strong decrease of the structure factor at high angles. By means of X-ray diffraction it is not possible to quantify the purity of materials. Samples with only one distinct reflection have also been found to contain substantial amounts of MCM-41.[18]

Transmission electron microscopy (TEM) is usually used to elucidate information on pore structures. Fig. 1.2 shows a TEM image of the hexagonal arrangement of uniform, 5 nm sized pores in a sample of MCM-41.[1] The exact analysis of pore sizes and thickness of pore walls is not possible without additional simulations because of the focus problem. Chen et al. demonstrated for MCM-41 that the thickness of the features (pore sizes and wall thickness) depends strongly on the focus conditions, and careful modeling is necessary for precise analysis.[20] Moreover, most MCM-41 samples show, not only ordered regions, but also disordered regions, lamellar and fingerprint like structures.[21]

Adsorption of probe molecules has been widely used to determine the surface area and to characterize the pore-size distribution of solid catalysts. The physisorption of gases such as N_2, O_2 and Ar has been used to characterize the porosities of MCM-41 upon its preparation.[22-25] The nitrogen adsorption isotherm for MCM-41, with pores of around 4.0 nm, which belongs to type IV in the IUPAC classification (Fig. 8.1),[26] shows two distinct features: (1) a sharp capillary condensation step at a relative pressure of 0.4 and (2) no hysteresis between adsorption and desorption branches (Fig. 1.3).[22] However, well-defined hysteresis loops were
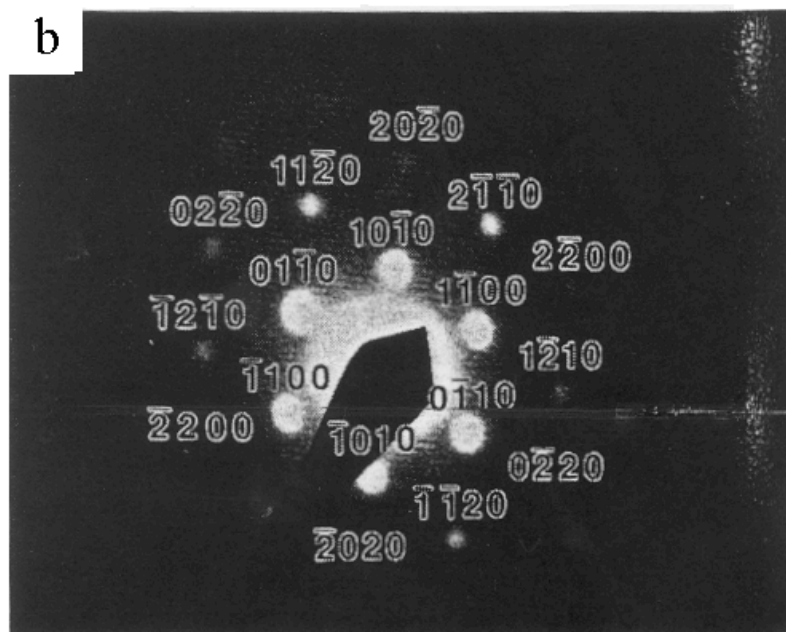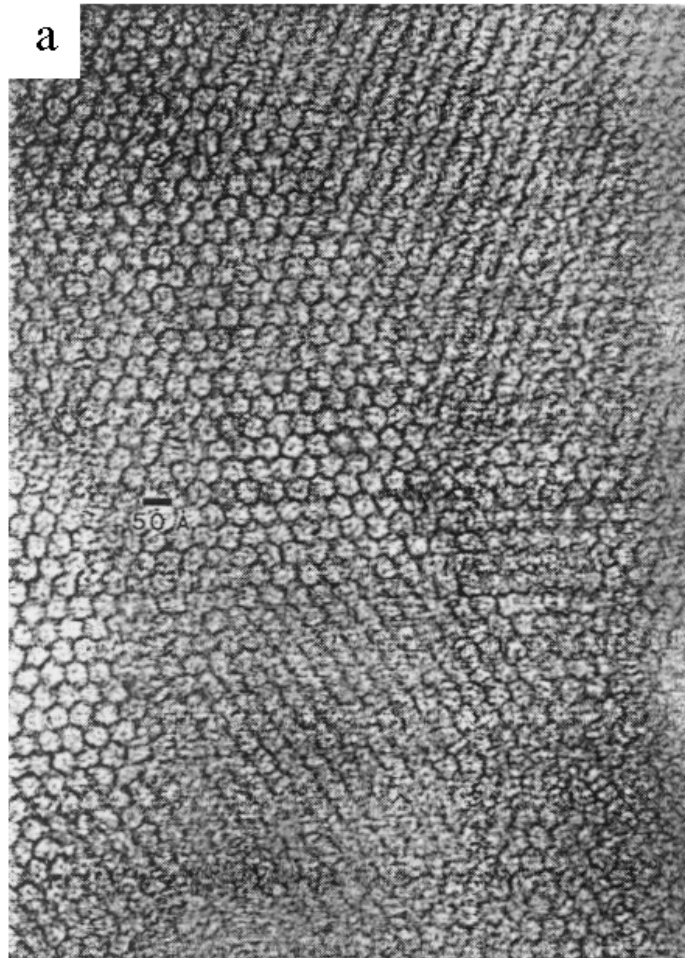
Figure 1.2 (a) Representative transmission electron micrograph of MCM-41, and (b) representative electron micrograph of MCM-41.[1]
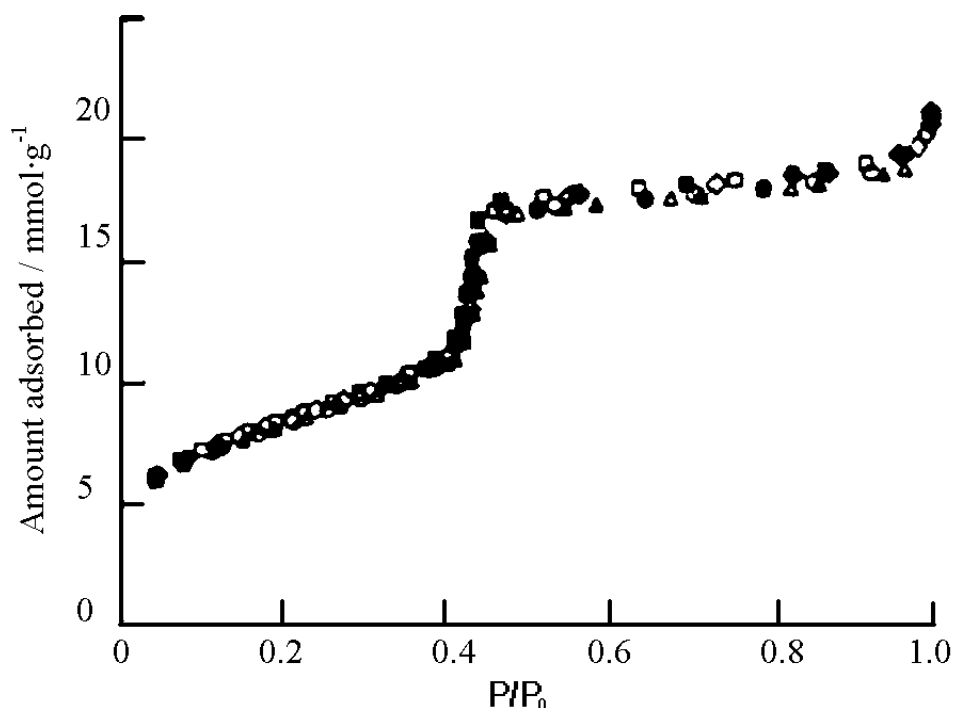
Figure 1.3 Nitrogen adsorption isotherm on MCM-41 with 4.0 nm pores at 77 K.[22]

observed in many cases. The presence and size of the hysteresis loops depend on the adsorbate,[23] pore size[27] and temperature.[28]

Several methods are known to determine the pore-size distributions in cylindrical pores, based on geometrical considerations,[29] thermodynamics[26] and a statistical thermodynamic approach.[30] In addition, freezing point depression can be used and followed by nuclear magnetic resonance (NMR) spectroscopy in the case of MCM-41.[31] The traditional method for analyzing pore-size distributions in the mesopore range is the Barrett-Joyner-Halenda (BJH) method[32,33] which is based on the Kelvin equation.

The wall thickness can be calculated by the difference between the lattice parameter (a = $2d(100)/3^{1/2}$) determined by X–ray diffraction and the pore size obtained by nitrogen adsorption analysis. Nevertheless, one should bear in mind that the values are only estimates, because so far no reliable means for pore-size analysis exists. Moreover, the lattice parameters are usually calculated from quite broad reflections and, therefore, do not correspond to an exact value. However, independent studies have shown, in the case of the

original MCM-41 synthesis, that the wall thickness of around 1.0 nm remains constant if the pore sizes are varied in the range between 2.5 and 10.0 nm.[2,34]

The characterization of pore walls focuses on two aspects: (1) structural properties and (2) surface chemistry. A very powerful method for the characterization of framework locations is solid-state NMR spectroscopy, such as ^{28}Si-NMR.[35] The surface properties of pore walls have been studied by adsorption of molecules on the surface and by using Fourier transform infrared (FTIR) spectroscopy. By adsorbing polar or non-polar molecules on surfaces, it is possible to measure the hydrophilic or hydrophobic properties of surfaces.[2, 35,36]

1.1.2. Formation Mechanism

A number of models have been used to explain the formation of mesoporous materials and to provide a rational basis for the various synthetic routes. Commonly, these models are predicated based on the presence of surfactants in a solution to guide the formation of the inorganic mesostructure from the solubilized inorganic precursors. Surfactants containing a hydrophilic head group and a long hydrophobic tail group within the same molecule will self-organize in such a way as to minimize contact between the incompatible ends. How the inorganic precursor interacts with the surfactant is an issue whereby the models diverge; the type of interaction between the surfactant and the inorganic precursor will be seen as a significant difference among the various synthetic routes, the formation models, and the resulting classes of mesoporous materials.

There have been a few proposed formation mechanisms about pure silicate composition since 1992: liquid crystal templating mechanism,[1] generalized liquid crystal templating mechanism,[19,37] formation of non-hexagonal mesophases,[38] hydrogen-bonding interaction,[39] true liquid crystal templating mechanism[40] and formation of other mesophases.[41]

Liquid crystal templating (LCT) mechanism

A liquid crystal templating (LCT) mechanism was proposed by the Mobil researchers, based on the similarity between liquid crystalline surfactant assemblies and M41S.[1] The common traits were the mesostructure dependence on the hydrocarbon chain length of the surfactant tail group,[42] the effect of variation of the surfactant concentrations, and the influence of organic swelling agents. With MCM-41 as the representative M41S material, two mechanistic pathways were postulated (Scheme 1.1):

(1) The aluminosilicate precursor species occupied the space between a preexisting hexagonal lyotropic liquid crystal (LC) phase and deposited on the micellar rods of the LC phase.

(2) The inorganics mediated, in some manner, the ordering of the surfactants into the hexagonal arrangement.
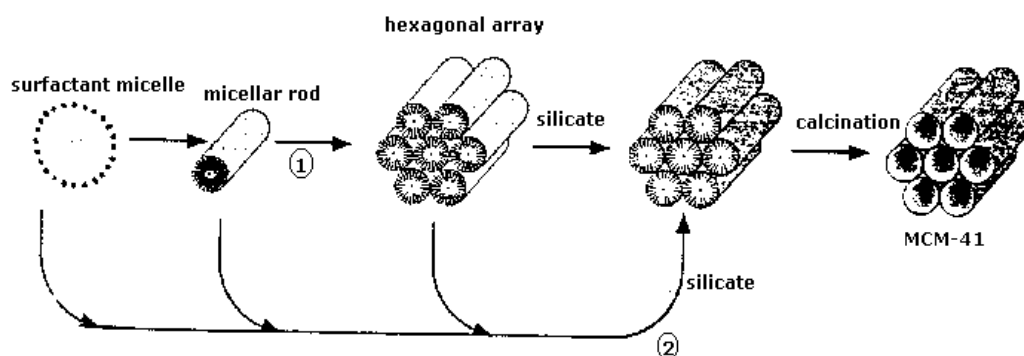
Scheme 1.1 Two possible pathways for the LCT mechanism.[32]

It was subsequently known that pathway (1) did not take place because the surfactant concentrations used were far below the critical micelle concentration (CMC) required for hexagonal LC formation.[43] However, recently this mechanistic pathway was demonstrated possible under different synthetic conditions.

The second mechanistic pathway of LCT was vaguely postulated as a cooperative self-assembly of the ammonium surfactant and the silicate precursor species below the CMC. It

has been known that no preformed LC phase is necessary for MCM-41 formation but, to date, the actual details of MCM-41 formation have not yet been fully agreed upon. Several mechanistic models have been postulated which share the basic idea that the silicate species promote LC phase formation below the CMC: "silicate rod assembly",[44] "silicate layer puckering",[45] "charge density matching",[46,47] "folding sheets",[48] "silicatropic liquid crystals"[49-51] and "silicate rod clusters"[52].

Generalized Liquid Crystal Templating Mechanism: Electrostatic Interaction

A generalized mechanism of formation based on the specific type of electrostatic interaction between a given inorganic precursor I and a surfactant head group S was proposed by Huo and co-workers.[37,53] Based on the nomenclature, pathway (2) of the original LCT mechanism (Scheme 1.1) which involved anionic silicate species and cationic quaternary ammonium surfactant, can be categorized as the S^+I^- pathway. By extension, the other charge-interaction pathways are S^-I^+, $S^+X^-I^+$ (X^- is a counteranion), and $S^-M^+I^-$ (M^+ is a metal cation). This classification system is useful, especially when other types of inorganic-organic interactions are considered (Fig. 1.4).[4]

Formation of Non-Hexagonal Mesophases

There are two synthetic routes for the derivation of silicate mesoporous molecular sieves

of various mesophases: the basic route (S^+I^-) and the acidic route ($S^+X^-I^+$). Synthesized in basic medium, the M41S family is made up of three well-defined mesostructures: MCM-41,

a) I = Si

$I^{\ominus}S^{\oplus}$〰〰〰 S = trimethylammunium

b) I = Sb

$I^{\oplus}S^{\ominus}$〰〰〰 S = sulfonate

c) I = Si

$I^{\oplus}X^{\ominus}S^{\oplus}$〰〰〰 X = Cl
                                            S = trimethylammonium

d) I = Al

$I^{\ominus}M^{\oplus}S^{\ominus}$〰〰〰 M = Na
                                            S = phosphate

e) I = Si

I^0--S^0〰〰〰 S = amine

f) I = Si

I^0--N^0〰〰〰 N = polyethylene oxide

g) I = Nb, Ta

I--S〰〰〰 S = amine
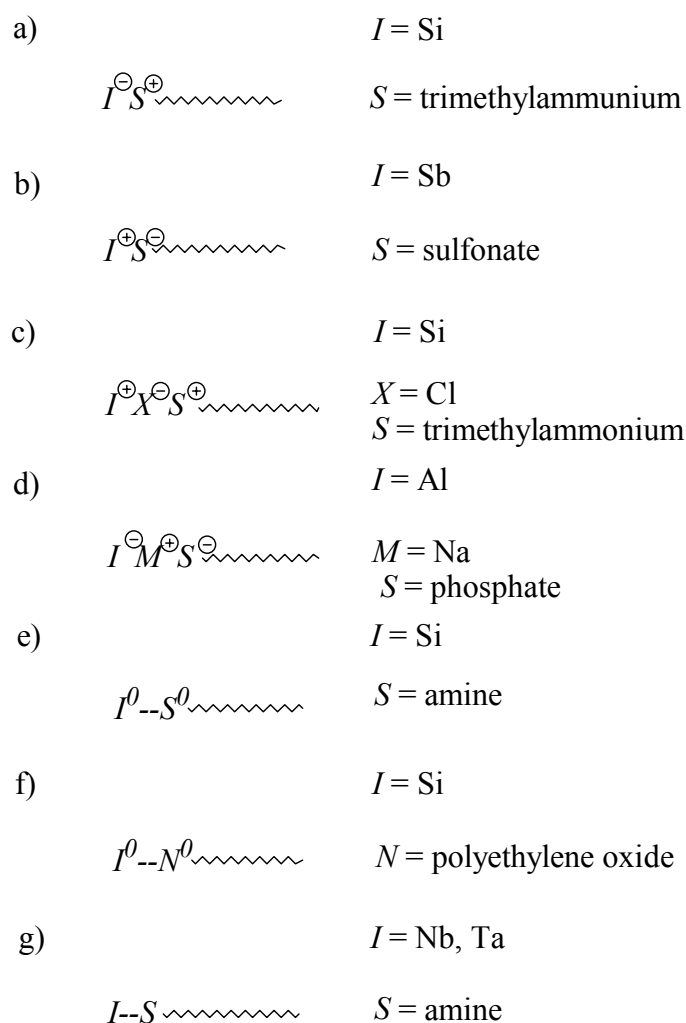
Figure 1.4 Schematic representation of the various types of inorganic-surfactant head group interactions: electrostatic: (a) $S^{+}I^{-}$, (b) $S^{-}I^{+}$, (c) $S^{+}X^{-}I^{+}$ and (d) $S^{-}M^{+}I^{-}$; hydrogen bonding: (e) $S°I°$ and (f) $N°I°$; and covalent bonding: (g) S-I.[4]

MCM-48, and MCM-50[38] (Fig. 1.5). MCM-41 has a hexagonally packed array of noninterconnecting cylindrical pores. The structure of MCM-48 belongs to the cubic space group. MCM-50 contains a lamellar structure in the uncalcined form; a mesoporous pillared layered structure forms when the surfactant is removed after post-synthetic treatment with TEOS.[54] Through the acidic route, APM materials termed SBA have been synthesized.[19] SBA-1 is cubic (Fig. 1.6),[19,53] but not bicontinuous as MCM-48; SBA-3 is the APM mesostructural analogue of MCM-41. The acid-derived materials have thicker pore walls and

a framework charge different from the base-derived mesoporous materials, due to the different precipitation conditions and charge balance requirements.

<div align="center">(a)   (b)   (c)</div>
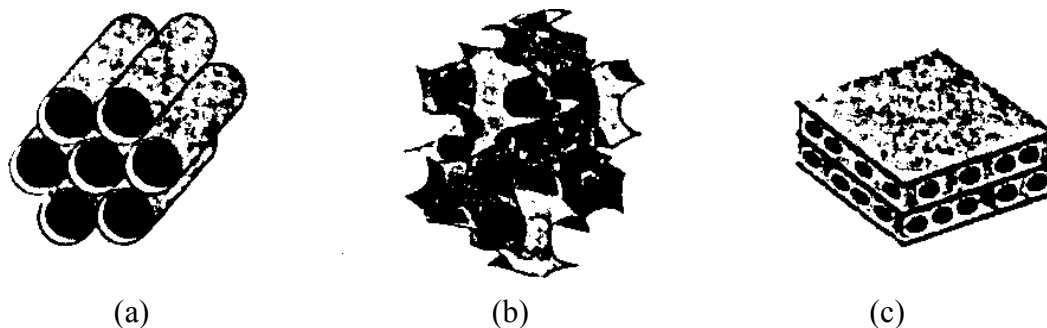
Figure 1.5 Illustrations of mesoporous M41S materials: (a) MCM-41, (b) MCM-48 and (c) MCM-50.[4]
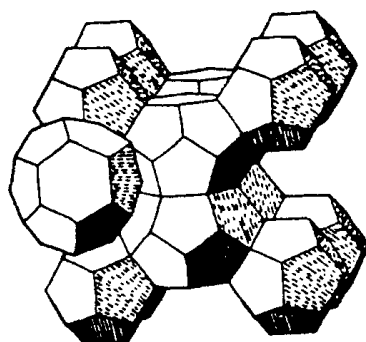
Figure 1.6 The cubic phase, in which the polyhedra represent micelles.[12]

Hydrogen-Bonding Interaction

Hydrogen-bonding interaction model was first postulated by Tanev and Pinnavaia.[39] They found that mesoporous silica could be prepared by the hydrogen-bonding interaction between an alkylamine (S^0) head group and hydroxylated TEOS (I^0). The materials lacked long-range ordering of pores and had higher amounts of interparticle mesoporosity, because the long-range effects of the electrostatic interaction that would normally control the packing of micellar rods were absent. Bagshaw and Pinnavaia[55] reported another hydrogen-bonding synthetic route using surfactant with a polyethylene oxide head group. The polyethylene

oxide head group is nonionic (N^0), unlike the amine head group (S^0) which is uncharged and can be ionized. The nonionic route (N^0I^0) seemed to provide greater pore ordering than the neutral route (S^0I^0), but still lacked long-range hexagonal packing order. The pores were more "wormlike" than rodlike cylinders.

True Liquid Crystal Templating Mechanism

By operating in the liquid crystal phase region of a polyethylene oxide surfactant solution, Attard et al.[40] showed that monolithic mesoporous silicates could be prepared. Tetramethylorthosilicate (TMOS) was gelled in the LC solution with removal of the LC-destabilizing methanol, to produce a hexagonal mesophase; the MCM-48 and layered phases were found possible also, depending on the chain length of the tail group. This synthesis approach could be considered a true LCT route, which supports the viability of pathway (1) of the originally proposed LCT mechanism for MCM-41 (Scheme 1.1). In this method of preparation, the organic-inorganic interaction was less important than the actual presence of a LC phase.

Formation of Other Mesophases

Mesoporous silicates with pore systems not as well-defined as those of the M41S and SBA materials could result when an additional salt is added to the synthesis mixture. The structures of these materials deviate from the ideal hexagonal pore packing of MCM-41, as detected by XRD and TEM. The long-range ordering of the materials is not definitive proof for "better" materials. Fig. 1.7 shows a "sponge" phase (L_3) of mesoporous silicates which exists in lyotropic surfactant solutions but has no long-range ordering.[41] Ryoo and co-workers added ethylenediaminetetraacetic acid (EDTA) to a high pH synthesis mixture, to create a hydrothermally stable mesoporous silicate with a highly branched network of pores similar to the L_3 surfactant phase (termed KIT-1).[56] It was proposed that the EDTA polyacid salt caused

the transformation of the hexagonal phase to the L_3-like mesophase. For these disordered mesoporous materials, at least one strong XRD peak could still be detected in the low-angle region.
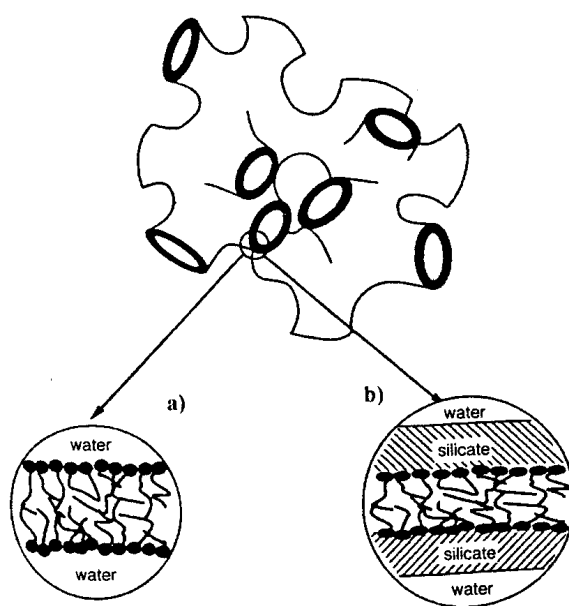
Figure 1.7 The silicate framework separates the water from the surfactants in the L_3 phase.[41]

Doped Silicate Compositions

The interest in doping mesoporous silicates with metals lies primarily in the development of catalytically active materials. The incorporation of a metal is seemingly straightforward in light of the various mechanistic pathways, but the amount of dopant incorporation, the reproduction of the mesophase that is obtained in the pure silica system and the stability of the resulting mesoporous material cannot be predicted. The development of catalytically active materials has been the main driving force in the research of doped mesoporous silicates with metals. Numerous investigations concerning the doping of MCM-

Table 1.2 Reports of dopant incorporation in silicate M41S materials.[12]

Authors	Metal dopant	Si/dopant molar ratio	Synthesis route[a]
Beck et al.[2]	Al	15	S^+I^-
Corma et al.[57]	Ti	56	S^+I^-
Reddy et al.[58]	V	60	S^+I^-
Tanev et al.[59]	Ti	100[b]	S^0I^0
Sayari et al.[60]	B	6.25[b]	S^+I^-
Luan et al.[61]	Al	10	S^+I^-
Fu et al.[62]	Al	≈ 1[b]	S^+I^-
Zhao et al.[63]	Mn	11	S^+I^-
Abdel-Fattah et al.[64]	Sn	99	S^0I^0
Cheng et al.[65]	Ga	30	S^+I^-
Cheng et al.[66]	Ga, Al	57, 57	S^+I^-
Koyano et al.[67]	Ti	80	S^+I^- (MCM-48)
Tuel et al.[68]	Al	6	S^0I^0
	Ga	31	S^0I^0
	Fe	55	S^0I^0
	B	17	S^0I^0
Tuel et al.[69]	Zr	17	S^0I^0
Ulagappan et al.[70]	Cr	30[b]	S^+I^-
Zhang et al.[71]	Ti	50[b]	S^+I^- (MCM-48)
	Cr	50[b]	S^+I^- (MCM-48)
	V	50[b]	S^+I^- (MCM-48)
Zhang et al.[72]	Ti	277, 76	S^+XI^+, S^0I^0
	V	434, 131	S^+XI^+, S^0I^0
	Cr	163, 70	S^+XI^+, S^0I^0
	Mn	3332, 118	S^+XI^+, S^0I^0
	Mo	95, 199	S^+XI^+, S^0I^0
Echchahed ed al.[73]	Fe	40	S^+I^- (MCM-48)
He et al.[74]	Fe	52	S^0I^0
Jones et al.[75]	Zr	25	S^+I^-
Zhang et al.[76]	Nb	10	S^+I^-
Wong et al.[77]	Zr	5	S^+XI^+

[a] MCM-41 structure, unless otherwise noted. [b] Molar ratio values of precursor mixtures, not of calcined materials.

41 with a variety of metals have appeared (Table 1.2).[12]

In general, the formation mechanisms for the non-silicate compositions have been classified into: generalized liquid crystal templating mechanism,[37] a modified sol-gel method,[78] and ligand-assisted templating method.[79] Various mechanisms have also been proposed in the cases of mesoporous alumina,[80] aluminophosphates,[81,82]

vanadophosphates,[83,84] zirconia[85-88] and metal sulfides.[89,90] The formation mechanisms of mesoporous titania, alumina and zirconia are specifically outlined in the following sections.

1.1.3. Mesoporous Titanium Oxide

MCM-41 analogues of transition metal oxides are anticipated useful as adsorbents and catalysts in a wide variety of processes such as NO_x decomposition, oxidation reactions, acid-catalyzed reactions, hydroxylation reactions and polymerization reactions.[12,10] Although MCM-41 analogues of mesoporous Nb,[79,91] Ta,[92] Zr,[86,87,93] Hf[94] and Mn[95] oxides have been synthesized, the extension to titanium oxide and its derivatives still remain elusive. Antonelli and Ying synthesized Ti-TMS1 by a modified sol-gel process using alkylphosphate as surfactant and titanium isopropoxide bis-acetylacetonate as metal center, representing the first example of non-alumina/non-silica based mesoporous material (Fig. 1.8).[78] The BET surface area of this material was ca. 200 m^2g^{-1} after calcination at 350 °C. Transmission electron microscopy (TEM) illustrated that there was still considerable retention of the hexagonal pore structure for the Ti-TMS1 sample after calcination. Since a significant amount of phosphate remained in the structure, the material was described as a titanium oxo-phosphate by Antonelli.[96]

Thieme and Schüth prepared a mesoporous titanium oxo-phosphate *via* a non-ionic surfactant route. A low-cost industrial polyethylenoxide (Dodecanol + 5 EO) (BASF) was used as a non-ionic surfactant. The formation of the mesoporous structure was dominated by hydrogen bonding between self-assembled surfactant micelles and inorganic precursors. BET surface area was reported as 350 m^2g^{-1} (Fig. 1.9).[97] The thermal stability of this material was high up to 550 °C, due to the stabilization effect of post-synthetic treatment with phosphoric
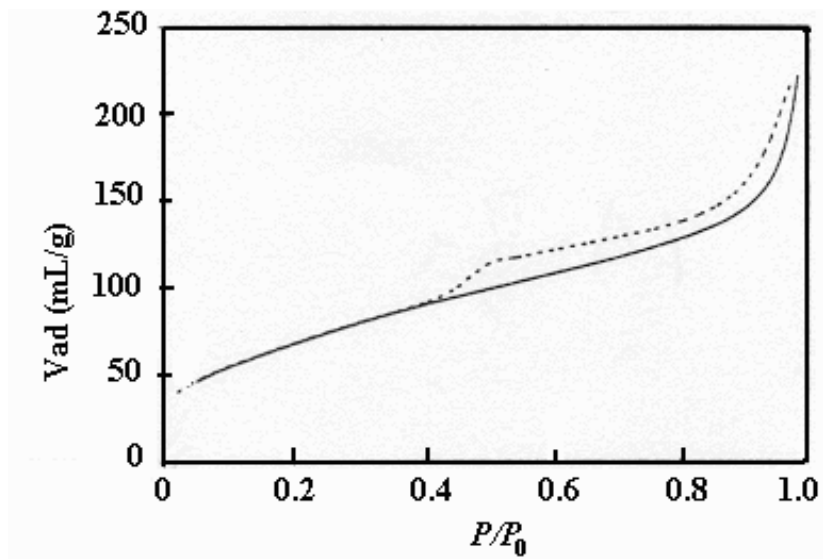
(a)
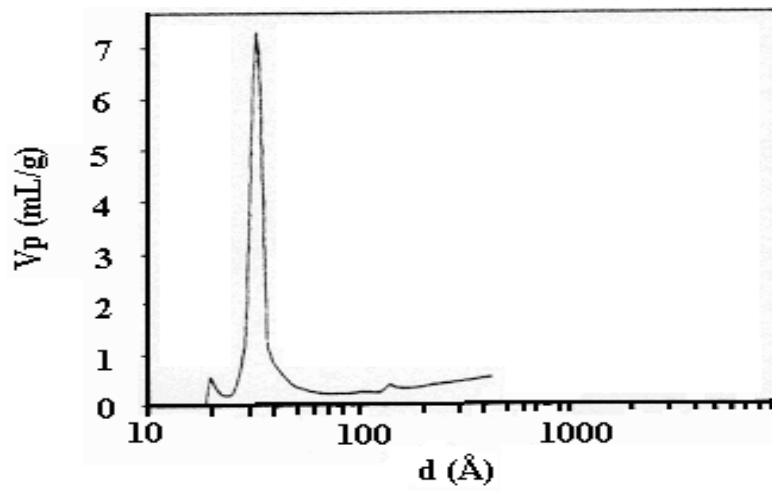
(b)
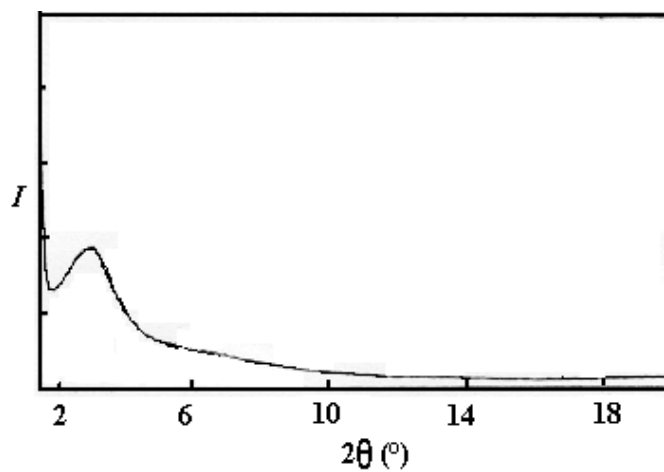
(c)

Figure 1.8 (a) Nitrogen adsorption-desorption isotherm, (b) BJH desorption pore size distribution and (c) XRD pattern for Ti-TMS1.[78]

acid. In contrast to the MCM-41 materials, there was no well-defined hexagonal pore structure. A disordered pore arrangement of the calcined titanium oxo-phosphate was confirmed by TEM studies.
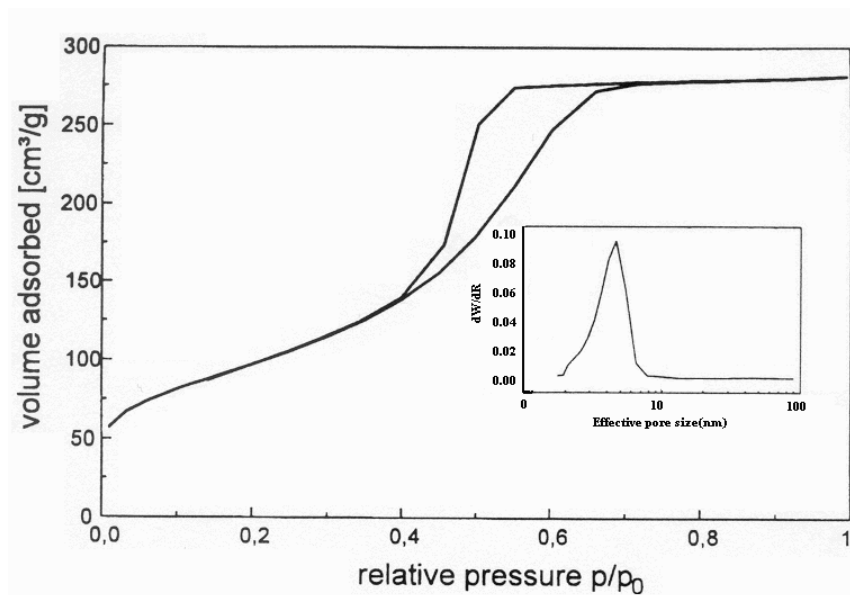
(a)
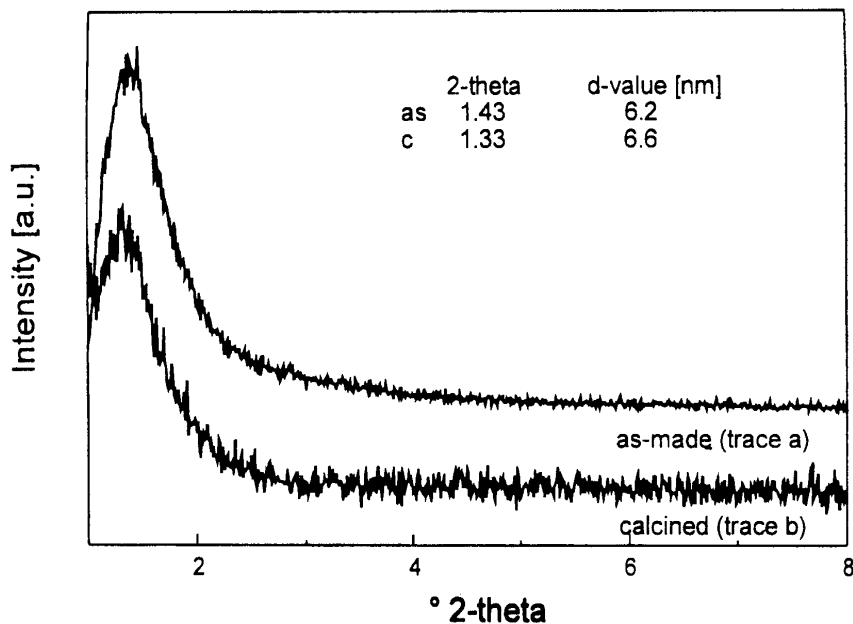
(b)

Figure 1.9 (a) Nitrogen adsorption-desorption isotherm, BJH desorption pore size distribution and (b) XRD pattern for a mesoporous titanium oxo-phosphate.[97]

(a)

(b)
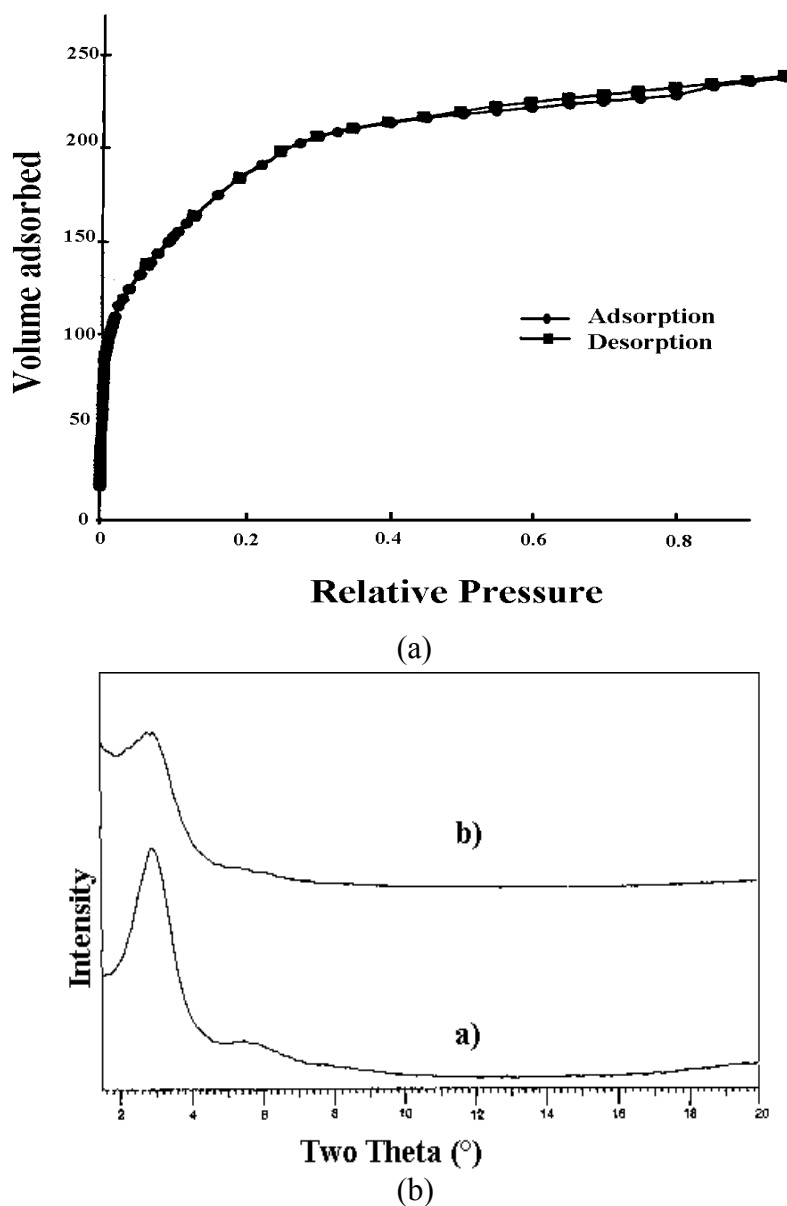
Figure 1.10 (a) Nitrogen adsorption-desorption isotherm and (b) XRD pattern for a phosphorus-free mesoporous titania.[96]

The first example of a phosphorous-free mesoporous titania, namely pure mesoporous titania, was recently reported by Antonelli (Fig. 1.10).[96] The synthesis of this material was accomplished by a modification of ligand-assisted templating route in which the higher-temperature aging was conducted in the absence of water. This material showed a high BET surface area of 700 m^2g^{-1}, but a low thermal stability. The BET surface area decreased to 180 m^2g^{-1} after calcination at 300 °C.
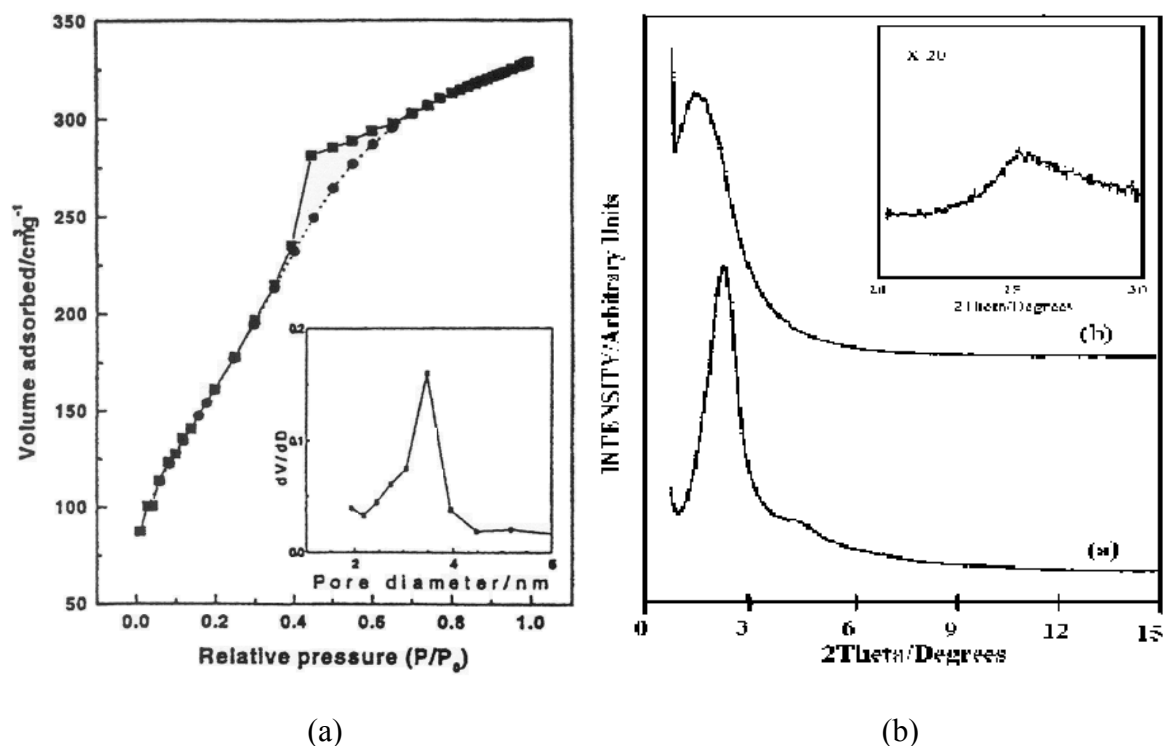
Figure 1.11 (a) Nitrogen adsorption-desorption isotherm and (b) XRD pattern for a mesoporous ICMUV-4 material.[98]

Cabrera et al.[98] recently reported a thermally stable pure mesoporous titania with a high surface area of 606 m^2g^{-1} (Fig. 1.11). The synthetic approach is based on the equilibrium between the hydrolysis and condensation reactions of the inorganic species and the organic-inorganic self-assembling process. The titanatrane complexes were used to retard the hydrolysis and condensation reactions. Unfortunately no detailed elemental analysis data were reported to confirm the purity of the material.

1.1.4. Mesoporous Zirconium Oxide

Zirconium oxide is an intriguing material in catalysis, and much effort has been devoted to the generation of a mesoporous form. Hudson and Knowles[85] utilized

alkyltrimethylammonium halide to template zirconium hydroxide to produce pure mesoporous zirconia with a high surface area. The templating effect was not seen in this synthesis, which resulted in a broad pore-size distribution. A "scaffolding" mechanism was then proposed in which the occluded surfactant basically acted as a filler to prevent the zirconia framework from collapsing during heat treatment. Reddy and Sayari[86] reported that a zirconium oxide mesostructure could be produced by using zirconium sulfate as the inorganic precursor in a S^+XI^+ synthetic route. However, the material collapsed upon calcination. Ciesla etc.[87] and Liu etc.[88] reported that a microporous zirconium oxo-phosphate was obtained by ion-exchanging the occluded sulfate counteranions with phosphates. Ciesla etc.[87] also described that a microporous zirconium oxide, stabilized with sulfates, could be produced by use of a different precursor, *e.g.* zirconium *n*-propoxide at low pH. A microporous oxide form of hafnium, a heavier congener of zirconium, was similarly derived.[94]

Fig. 1.12 illustrates a proposed amphoteric surfactant templating route for hexagonal mesophase formation. In this case, the carboxylate group accomodates the bonding of the surfactant with the inorganic species and the quaternary ammonium group maintains a large head-group area for hexagonal mesophase formation.[99]

Pure zirconium oxide is a weakly acidic catalyst and is not useful for reactions that demand strong acidity. To increase acidic strength, modification of the pure zirconium oxide with anions or metal dopants is required. Mesoporous phosphated zirconium oxide, a moderately acidic material, was prepared through a one-pot synthesis by the reaction of zirconium *n*-propoxide and alkylphosphates.[93,100] The phosphate groups that remained after calcination enhanced the thermal stability (as in the case of microporous zirconium oxo-phosphates) and increased the acidic strength of the zirconia framework.
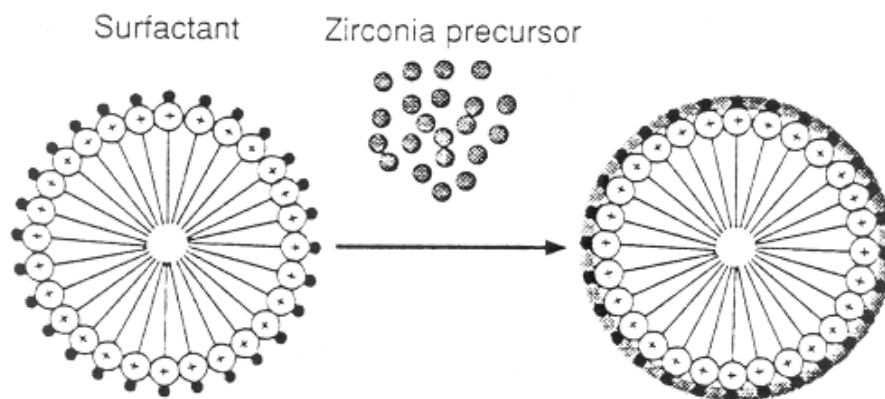
Figure 1.12 A proposed formation mechanism for mesoporous zirconia.[99]

1.1.5. Mesoporous Aluminum Oxide

Activated aluminas are attractive catalysts for processes such as petroleum hydrodesulfurization, the Claus reaction, dehydrogenation of butane to butene, dehydrogenation of alcohols to alkenes, and $DeNO_x$ reaction, etc. On the other hand, the properties of these widely used phases are limited, as they only possess textural porosity and lack the selective framework/confined pore structure characteristic of a molecular sieve. Therefore, the synthesis of mesoporous aluminas is of significant industrial interest.

The original synthesis of Mobil M41S mesoporous molecular sieves was accomplished by electrostatic interactions between a positively charged surfactant and a negatively charged inorganic precursor to assemble the mesostructure.[1,2] Attempts to prepare other mesoporous aluminas by electrostatic assembly pathways have failed,[37,53,101] as attempts to remove the surfactant resulted in product collapse.

Pinnavaia and co-workers demonstrated that mesostructure assembly could be achieved through hydrogen bonding interactions between neutral inorganic precursors and neutral alkylamine or nonionic polyethylene oxide surfactants.[39,55] By this method, using nonionic polyethylene oxide as surfactant, the first examples of mesoporous alumina molecular sieves,

which had BET surface areas in the range of 420 to 535 m^2g^{-1} and BJH pore diameter of 24 to 47 Å, were obtained. The corresponding d spacing and the pore size increased as the surfactant size increased (Fig. 1.13).[80]

Davis and co-workers described the synthesis of a pure mesoporous alumina that exhibited a BET surface area as high as 710 m^2g^{-1} and a narrow pore size distribution centered at ca. 20 Å by using sodium dodecylbenzenesulfonate as an anionic surfactant. They found that an approximately constant pore diameter (ca. 20 Å) could not be tailored by changing the surfactant length (Fig. 1.14).[102]

A new method recently being reported found that self-assembling processes leading to the formation of mesoporous aluminas could be controlled by adjusting the processes *i.e.* the hydrolysis and condensation reactions occurring in the inorganic phase. Interestingly, by this method pore sizes can be tuned by the sole adjustment of the molar ratio of the reactants (Fig. 1.15).[103]

Thermal stability is one of the important criteria for mesoporous materials. Pinnavaia etc.[104] reported that the incorporation of 1.0-5.0 mol% of Ce^{3+} or La^{3+} ions in MSU-X alumina molecular sieves, which were prepared through a N^0I^0 assembly pathway, dramatically improved their thermal stability without altering the mesopore size and the wormhole channel motif. (Fig. 1.16, Table 1.3). By means of ion-pair interactions of an aluminophosphate species with a cationic surfactant [$C_{16}H_{33}NMe_3Cl$] in the presence of tetramethylammonium hydroxide, a mesoporous aluminophosphate with BET surface area of 772 m^2g^{-1} after calcination at 550 °C was obtained by Kevan etc.[105]

(a)

(b)

(c)
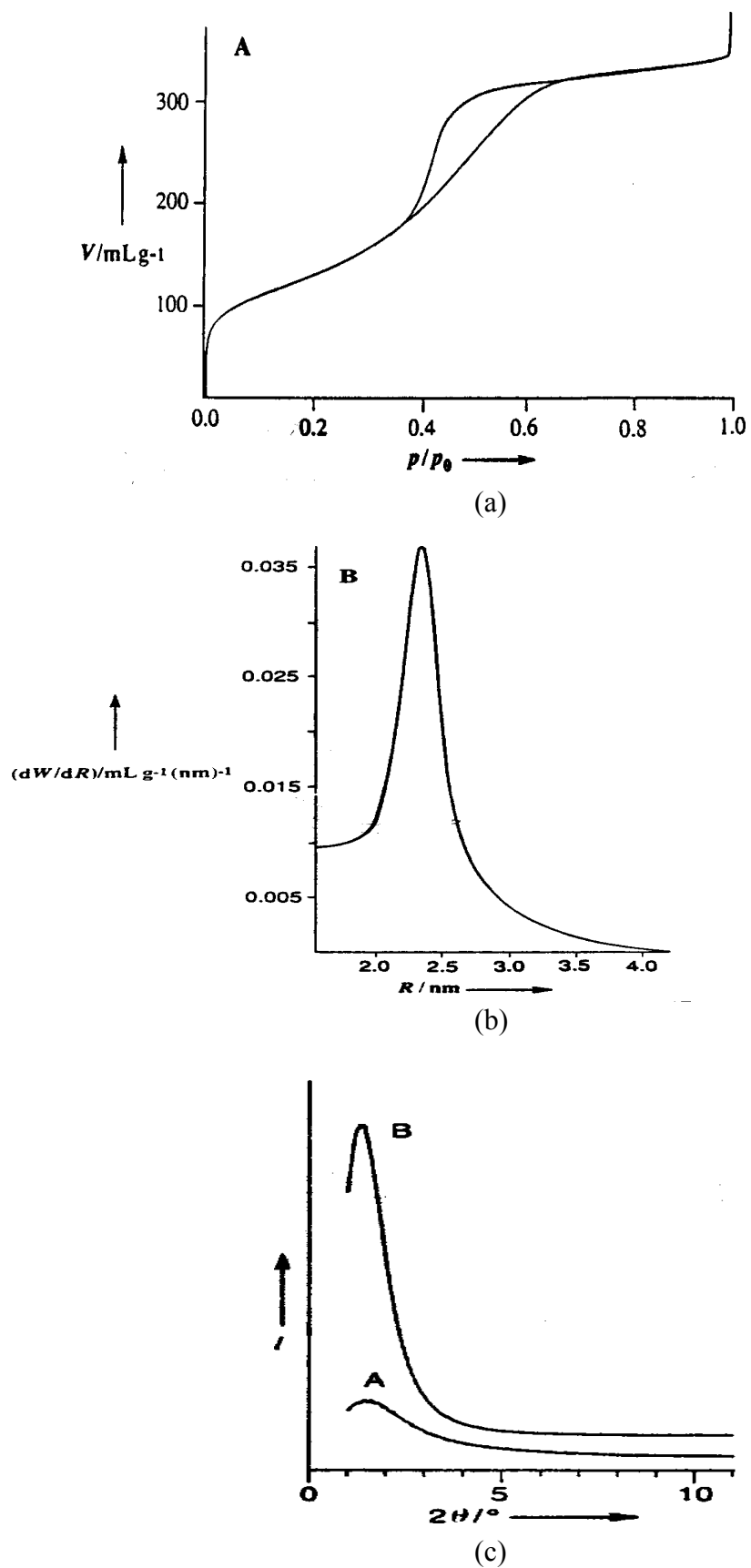
Figure 1.13 (a) Nitrogen adsorption-desorption isotherm, (b) BJH adsorption pore size distribution and (c) XRD pattern for a mesoporous alumina MSU-3.[80]
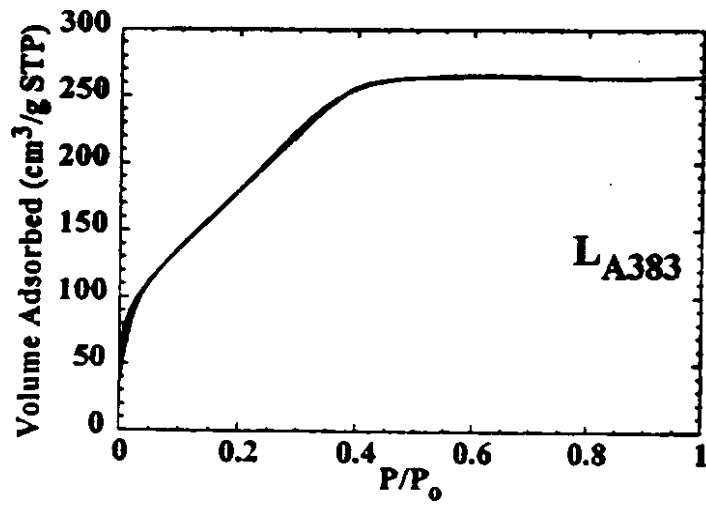
(a)
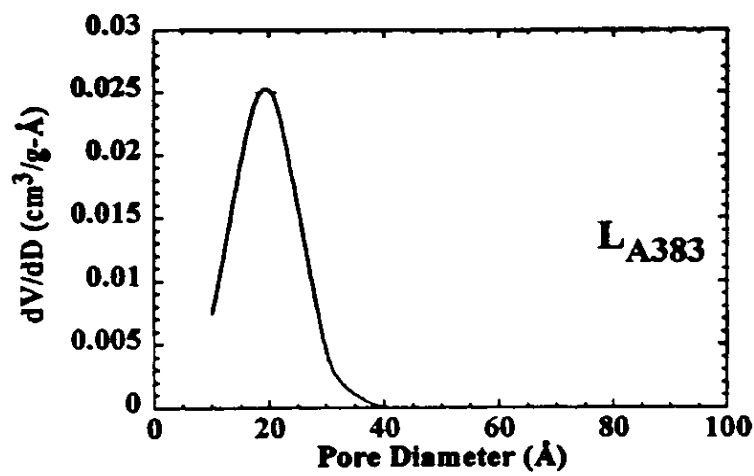
(b)
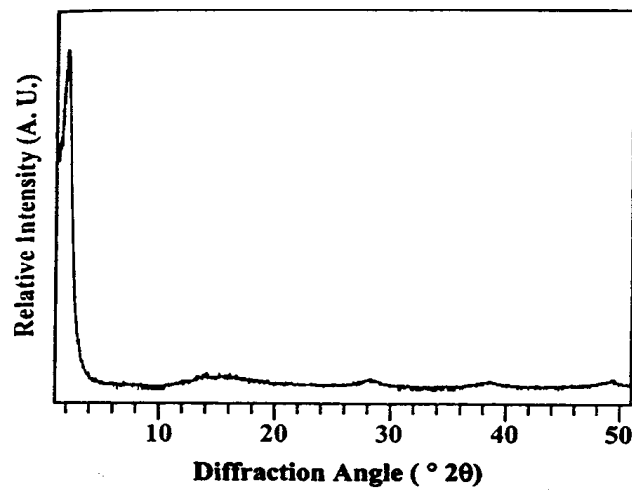
(c)

Figure 1.14 (a) Nitrogen adsorption-desorption isotherm, (b) BJH pore size distribution and (c) XRD pattern for a mesoporous alumina.[102]
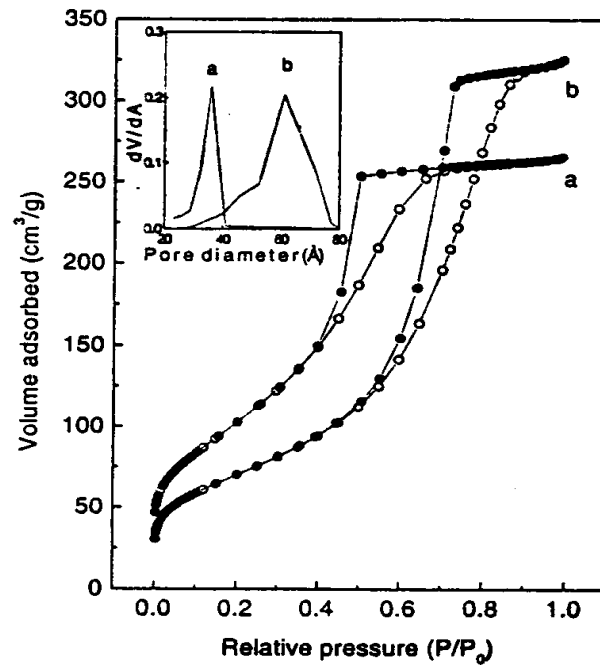
(a)
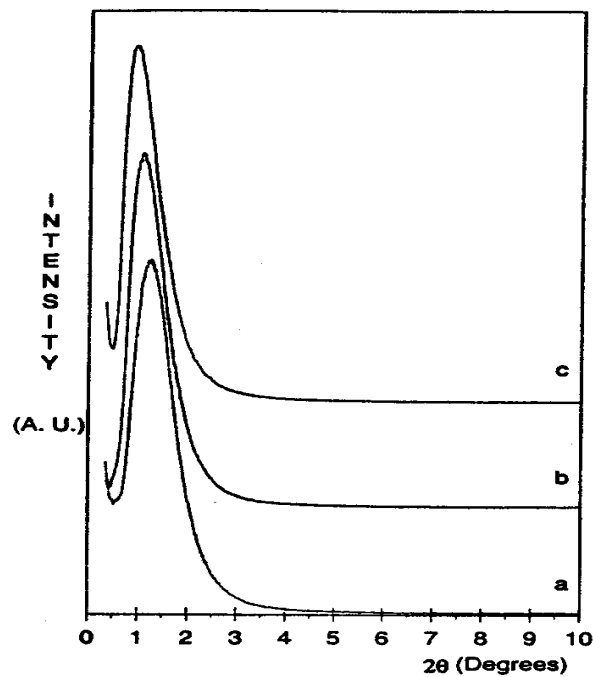
(b)

Figure 1.15. (a) Representative N_2-adsorption-desorption isotherms and pore size distributions (inserted) for ICMUV-1 aluminas isolated with water/TEA ratios of 7.4 (trace a) and 44.5 (trace b); (b) representative XRD powder diffractions of mesoporous ICMUV-1 aluminas synthesized with water/TEA ratios of 7.4 (trace a; d = 69 Å), 22.1 (trace b; d = 79 Å) and 44.5 (trace c; d = 95 Å).[103]
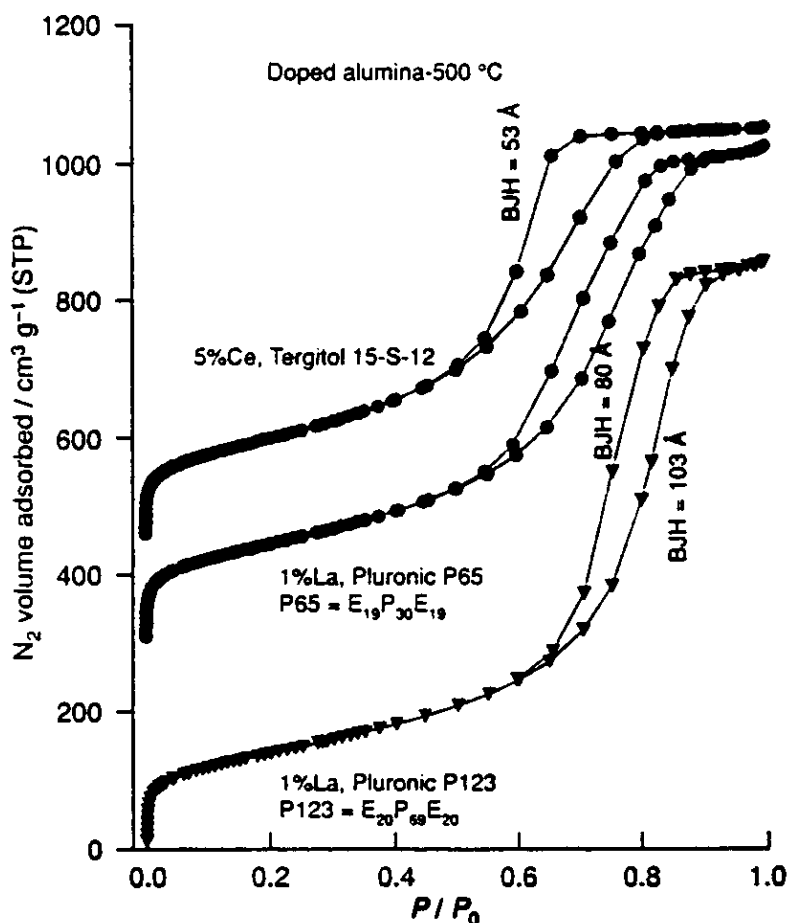
Figure 1.16 N_2 adsorption-desorption isotherms of rare earth stabilized MSU-X alumina molecular sieves assembled by using the non-ionic surfactants Tergitol 15-S-12, Pluronic P65, and Pluronic P123 as structure directors and calcined at 500 °C. The BJH pore size distributions obtained from the desorption isotherms are included for comparison.[104]

1.1.6. Objectives

The general objective of our research is to explore a convenient synthetic methodology for mesoporous titanium oxide and mesoporous aluminum oxide that possess not only high BET surface area but also high thermal stability. For this purpose, the following respects are going to be investigated:

Table 1.3 Physical properties of mesoporous MSU-X molecular sieves.[104]

Surfactant	Rare earth mol%	$T_{calcination}$[a] °C	S_{BET} m^2g^{-1}	D_{BJH} Å	V_{liquid} cm^3g^{-1}	d_{XRD} nm
15-S-12	0	500	391	50	0.48	7.8
15-S-12	0	600	267	55	0.31	8.0
15-S-12	5 (Ce)	500	530	53	0.2	8.0
15-S-12	5 (Ce)	600	357	54	0.65	8.0
P65	1 (La)	500	517	80	1.11	> 8.3
P123	1 (La)	500	487	108	1.31	> 10.0

[a] All the samples were calcined in air for 6 h.

(1) Metal-surfactant interaction. We believe that a strong interaction between a metal center and a surfactant is an essential factor for the synthesis of a high-quality mesoporous material. Taking titanium as an initial entry, proper choice of inorganic precursor and organic surfactant, for the purpose of resulting in strong metal-template interaction, is going to be investigated in detail.

(2) Method of surfactant removal. This is a key step to keep the mesoporous structures from collapsing. Basic methods include organic solvent extraction, acid treatment, base treatment and calcination. In our research, the methodology of surfactant removal is going to be optimized, in order to produce mesoporous titanium oxide with high surface area and high thermal stability.

(3) Extension of synthesis strategy for the mesoporous titanium oxide to zirconium oxide and aluminum oxide. Aluminum and zirconium oxides in mesoporous form are also our research interest. It is intriguing and worthwhile to extend the successful synthetic methodology to the preparation of mesoporous aluminum and zirconium oxides.

1.2. Catalytic Applications of Mesoporous Molecular Sieves

The unique physical properties of MCM-41 have made these materials highly desirable for catalytic applications. The catalytic applications of MCM-41 type materials have been comprehensively reviewed.[11,106,108]

The first catalytic studies with mesoporous molecular sieves focused on metal-substituted MCM-41 materials in which the active species was incorporated into the silicate matrix. The reactions studied were mainly oxidation and acid catalysis reactions. The next stage of development of MCM-41-based catalysts involved the deposition of heteroatoms onto the surface of the mesoporous framework. Since then, a wide variety of applications have been established and the field is rapidly expanding. More recently, research has been devoted to the fixation of catalytically active complexes onto the wall of the MCM-41 porous framework thereby combining the advantages of homogeneous catalysis with a heterogeneous catalyst support. Although extensive research efforts have been undertaken to explore the catalytic applications of modified MCM-41 materials, its industrial use has so far been limited. It is yet to be determined whether commercial applications of these systems will become economically feasible.

When MCM-41 was first discovered, there were great expectations for applications in the petroleum industry, for instance in processing of heavy residues. It was assumed that the aluminosilicate materials exhibited acid site strengths comparable to those of zeolites. As the incorporation of aluminum into silica structures is known to form acidic sites in the framework, mesoporous aluminosilicates were tested in acid catalysis.[109-112] However, MCM-41 materials show only weak acidity which is comparable to amorphous aluminosilicates independent of the aluminum content in the framework. Therefore, they are only promising for reactions that do not require very strong acidity.

To enhance the catalytic potential, several metal ions have been isomorphously substituted, *e.g.* titanium,[113-118] zirconium,[119] vanadium,[120-123] iron,[124-126] cobalt,[127] boron,[128-131] tin[132] and platinum[133]. Promising catalytic activities have been observed for Ti-MCM-41 in the selective oxidation of large organic molecules in the presence of *tert*-butyl hydroperoxide (TBHP) or dilute H_2O_2. Ti-MCM-41 is more active than Ti-Beta, a large-pore zeolite, in these reactions because of lower diffusion limitations. However, with the exception of Ti-MCM-41, the properties of metal-incorporated MCM-41 leave much to be desired.

Whereas isomorphous substitution is used as a method to tailor zeolite properties, this technique does not seem to be applicable to mesoporous materials, probably due to the amorphous walls. New methods to incorporate metals have had to be developed beyond the traditional ones such as ion exchange and incipient wetness impregnation. Maschmeyer and Thomas[134,135] prepared a catalyst by grafting metallocene complexes onto mesoporous silica. Large concentrations of accessible, well-spaced and structurally well-defined active sites were achieved. This approach has also been successfully used for vanadium incorporation.[136] Another way of ensuring a high dispersity of the catalytically active sites onto the support MCM-41 has been achieved.[137] Well-defined metal clusters like Pd_{561} and Au_{55} have been used as precursors of the active components. Since these metal clusters are stabilized by hydrophobic ligands, an *in situ* synthesis proved possible to incorporate the clusters, which interact with the hydrophobic surfactant chain. After calcination to remove both the surfactant and the ligands, very small (2 to 4 nm) metal clusters were found to be highly dispersed on the MCM-41 inner and outer surfaces. However, so far it is not clear whether MCM-41 as a support for noble metals will have advantageous properties as compared with optimized amorphous silica supports.

Except for the catalytic applications of silica-based mesoporous materials, many non-siliceous materials with mesopores are potentially interesting as catalysts or catalyst support for various reactions. Alumina has been known as a catalyst support for a long time.[138] The

availability of this support with high surface area and regular pore distribution should in many cases, lead to substantial advantages. Larger molecules may possibly be transformed with shape-selectivity like that zeolites demonstrate for small molecules. Transition metal oxides introduce their redox activity as an additional component and could possibly be used directly as redox catalysts.[108]

1.2.1. Catalysts for DeNO$_x$ Reaction

Nitrogen oxides (NO$_x$) are emitted primarily from transportation and other industrial sources and significantly contribute to a variety of environmental problems, *e.g.* the formation of acid rain and the resultant acidification of aquatic systems, ground-level ozone (smog), and general atmospheric visibility degradation. Therefore, legislation requires that the emission of NO$_x$ is strictly limited. Fig. 1.17 shows a few processes of chemical transformations of atmospheric NO$_x$.

During the past decade, various aspects of DeNO$_x$ catalysts have been reviewed by Traa et al.,[107] Busca et al.,[140] Fritz et al.,[141] Kharas et al.[142] and Shelef.[143]

The catalytic methods for removing NO$_x$ from engine exhaust gases are usually classified into three classes: (1) non-selective reduction, (2) selective reduction and (3) decomposition. We are currently very interested in the so-called hydrocarbon selective catalytic reduction (HC-SCR) of nitrogen oxide process. From the literature, three types of catalysts are active for the HC-SCR: zeolites, metal oxides and noble metals.

The group of zeolite catalysts can be divided into two classes, the first containing the Cu-ZSM-5, while the second comprises the ZSM-5 framework with copper substituted by a large variety of cations or other zeolitic structures. The former, under certain experimental conditions, exhibited a good activity and high selectivity towards nitrogen. However, these catalysts are subject to hydrothermal deactivation and are only active at temperatures too high

to be considered for diesel applications. The substitution of copper by other metals or the use of a zeolite structure other than ZSM-5 has lead to the development of formulations that exhibit acceptable conversions even at high space velocity.
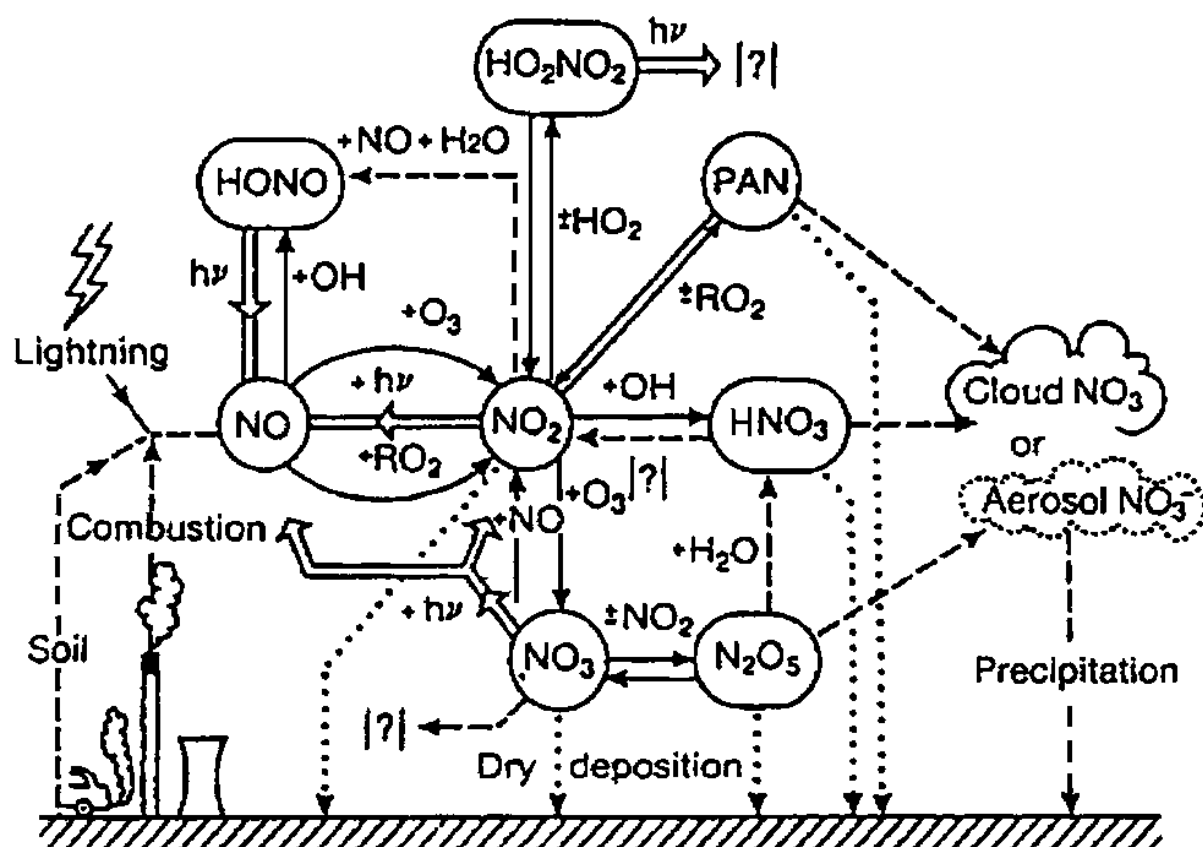
Figure 1.17. Chemical transformations of atmospheric NO_x: photochemical processes, thermal gas-phase processes, dry deposition and heterogeneous reactions.[139]

A wide variety of metal oxides (bulk or supported) exhibited a moderate activity for HC-SCR. A major advantage of these catalysts is that a large selection of reducing agents can be used. The drawbacks lie in the high operation temperature (> 673 K), the low activity at high space velocity, and the deactivation of the catalysts by sulphur dioxide and thermal aging due to loss of specific area.

Noble metal catalysis has proved a very challenging area of research. Originally, it was not realized that this group was very active for HC-SCR in strongly oxidizing conditions and with high space velocities. A high activity was generally observed at low temperatures, but within too narrow a range. For most of the examples, the efficiency is only slightly affected by the presence of water, though it is known that noble metals show some resistance to sulphur dioxide poisoning.

In the past decade, the sol-gel process offers the advantage of the preparation of high-purity materials with a mesoporous pore distribution and a high surface area. Such materials have ideal properties for applications as catalyst supports. A number of catalytic reductions of NO_x have been carried out on mesoporous molecular sieves.[145-150,152] However, sol-gel-processed materials have not found applications in automotive catalysts due to the cost considerations and the loss of beneficial properties of the materials at elevated temperatures. Thus, the materials can only be used in applications where temperatures are not extremely high or the cost is offset by a reduced use of platinum group metals.

1.2.2. Catalysts for Dehydrogenation of Alcohols

The oxidation of alcohols to the corresponding aldehydes and ketones is one of the most fundamental and important processes in the organic synthesis and the chemical industry. Many of the methods currently employed necessitate the use of a stoichiometric or excess amount of heavy metals (e.g., Cu, Cr, Mn, etc.) or expensive oxidants (e.g., DCC, oxalyl chloride, NCS, etc.). From economical and environmental points of view, the advantage of gas-phase catalytic oxidation is apparent.[151] Therefore, considerable research in the field of alcohol dehydrogenation has focused on the application of SiO_2, Al_2O_3 and zeolites supported metal/metal-ion/metal-oxide catalysts.[152-161] Tsuruya investigated the vapor-phase oxidation of benzyl alcohol over Cu(II) ion-exchanged NaZSM-5 type zeolite.[152] The yield was only

27% at 723 K. Subsequently they reported that alkali-metal addition to Cu-NaZSM-5 promoted the oxidation activity, the yield of benzaldehyde was 21% at 673 K.[154,157] They also investigated the promotion effect of doping Cu/SiO_2 catalyst with alkali-metal.[155] Yield of benzaldehyde of 78% was attained with $Na-Cu/SiO_2$ where the Na/Cu atomic ratio was 4. Chang synthesized Cu/Al_2O_3 catalysts by electrolysis plating technique.[156,158] These catalysts exhibit a higher dispersion and a more even spread of copper on the Al_2O_3 surface, thereby rendering a better dehydrogenation ability than the catalysts prepared by the impregnation and precipitation methods.

1.2.3. Objectives

In the chemical process industry, catalysts with high activity, selectivity and long lifetime are essential. The mesoporous materials are reasonably expected to be excellent candidates as catalysts and catalyst supports, due to their unique physical properties, *i.e.* large and uniform pore sizes (relative to that of microporous zeolites) and high surface areas. Our specific interest lies in the applications of mesoporous titanium oxide and aluminum oxide in $DeNO_x$ and dehydrogenation of alcohols. Using mesoporous titania and mesoporous alumina as catalysts or catalyst supports, our research is directing towards preparing catalysts which have high activity, high selectivity and long life-time.

References

1. C. T. Kresge, M. E. Leonowicz, W. J. Roth, J. C. Vartuli, J. S. Beck, *Nature* **1992**, *359,* 710.

2. J. S. Beck, J. C. Vartul, W. J. Roth, M. E. Leonowicz, C. T. Kresge, K. D. Schmitt, C. T.-W. Chu, D. H. Olson, E. W. Sheppard, S. B. McCullen, J. B. Higgins, J. L. Schlenker, *J. Am. Chem. Soc.* **1992**, *114*, 10834.

3. C. J. Brinker, *Curr. Opin. Solid State Mater. Sci.* **1996**, *1*, 798.

4. J. C. Vartuli, C. T. Kresge, W. J. Roth, S. B. McCullen, J. S. Beck, K. D. Schmitt, M. E. Leonowicz, J. D. Lutner, E. W. Sheppard, *Advanced Catalysts and Nanostructured Materials: Modem Synthesis Methods* (Ed.: W. R. Moser), Academic Press, New York, **1996**, pp. 1-19.

5. G. D. Stucky, Q. Huo, A. Firouzi, B. F. Chmelka, S. Schacht, I. G. Voigt-Martin, F. Schüth, *Progress in Zeolite and Microporous Materials, Studies in Surface Science and Catalysis*, Vol. 105 (Ed. H. Chon, S.-K. Ihm, Y. S. Uh), Elsevier, Amsterdam, **1997**, pp. 3-28.

6. N. K. Raman, M. T. Anderson, C. J. Brinker, *Chem. Mater.* **1996**, *8*, 1682.

7. D. M. Antonelli, J. Y. Ying, *Curr. Opin. Coll. Interf. Sci.* **1996**, *1*, 523.

8. P. Behrens, *Angew. Chem. Int. Ed. Engl.* **1996**, *35*, 515.

9. X. S. Zhao, G. Q. Lu, G. J. Millar, *Ind. Eng. Chem. Res.* **1996**, *35*, 2075.

10. A. Sayari, *Chem. Mater.* **1996**, *8*, 1840.

11. U. Ciesla, F. Schüth, *Micro. Meso. Mater.* **1999**, *27*, 131.

12. J. Y. Ying, C. P. Mehnert, M. S. Wong, *Angew. Chem. Int. Ed.* **1999**, *38*, 56.

13. K. S. W. Sing, D. H. Everett, R. H. W. Haul, L. Moscou, R. A. Pierotti, J. Rouquerol, T. Siemieniewska, *Pure Appl. Chem.* **1985**, *57*, 603.

14.   P. Behrens, *Adv. Mater*. **1993**, *5*, 127.

15.   U. Ciesla, M. Grün, T. Isajeva, A. A. Kurganov, A. V. Neimark, P. Ravikovitch, S. Schacht, F. Schüth, K. K. Unger, *Access in Nanoporous Materials*, T. J. Pinnavaia, M. F. Thorpe (Eds.), Plenum Press, New York, **1995**.

16.   K. J. Edler, J. W. White, *Chem. Mater*. **1997**, *9*, 1226.

17.   D. Khushalani, A. Kuperman, N. Coobs, G. A. Ozin, *Chem. Mater*. **1996**, *8*, 2188.

18.   A. Corma, *Chem. Rev*. **1997**, *97*, 2373.

19.   Q. Huo, D. I. Margolese, G. D. Stucky, *Chem. Mater*. **1996**, *8*, 1147.

20.   C. Y. Chen, S.-Q. Xiao, M. E. Davis, *Microporous Mater*. **1995**, *4*, 1.

21.   V. Alfredsson, M. Keng, A. Monnier, G. D. Stucky, K. K. Unger, F. Schüth, *J. Chem. Soc., Chem. Commun*. **1994**, 921.

22.   P. J. Branton, P. G. Hall, K. S. W. Sing, *J. Chem. Soc., Chem. Commun*. **1993**,1257.

23.   P. J. Branton, P. G. Hall, K. S. W. Sing, H. Reichert, F. Schüth, K. K. Unger, *J. Chem. Soc., Faraday Trans*. **1994**, *90*, 2956.

24.   O. Franke, G. Schulz-Ekloff, J. Rathousky, J. Starck, A. Zukal, *J. Chem. Soc., Chem. Commun.* **1993**, 724.

25.   R. Schmidt, M. Stöcker, E. Hansen, D. Akporiaye, O. H. Ellestad, *Microporous Mater*. **1995**, *3*, 443.

26.   S. J. Gregg, K. S. W. Sing, *Adsorption, Surface Area and Porosity*, 2nd edn, Academic Press, London, **1995**.

27.   P. L. Llewellyn, Y. Grillet, F. Schüth, Reichert, K. K. Unger, *Microporous Mater*. **1994**, *3*, 345.

28.   J. Rathousky, A. Zukal, O. Franke, G. Schulz-Ekloff, *J. Chem. Soc., Faraday Trans*. **1995**, *91*, 937.

29.   M. Kruk, M. Jaroniec, A. Sayari, *J. Phys. Chem*. **1997**, *101*, 583.

30.   P. I. Ravikovitch, S. C. O'Domhnaill, A. V. Neimark, F. Schüth, K. K. Unger, *Languir* **1995**, *11*, 4765.

31.   D. Akporiaye, E. W. Hansen, R. Schmidt, M. Stöcker, *J. Phys. Chem*. **1994**, *98*, 1926.

32.   E. P. Barrett, L. G. Joyner, P. P. Halenda, *J. Am. Chem. Soc*. **1951**, *73*, 373.

33.   M. Kruk, M. Jaroniec, A. Sayari, *Languir* **1997**, *13*, 6267.

34.   A. Corma, Q. Kann, M. T. Navarro, J. Perez-Pariente, F. Rey, *Chem. Mater*. **1997**, 9, 2123.

35.   C.-Y. Chen, H.-X, Li, M. E. Davis, *Microporous Mater*. **1993**, *2*, 17.

36.   P. L. Llewellyn, F. Schüth, Y. Grillet, F. Rouquerd, J. Rouquerol, K. K. Unger, *Languir* **1995**, *11*, 574.

37.   Q. Huo, D. I. Margolese, U. Ciesla, P. Feng, T. E. Gier, P. Sieger, R. Leon, P. M. Petroff, F. Schüth , G. D. Stucky, *Nature* **1994**, *368*, 317.

38.   J. C. Vartuli, K. D. Schmitt, C. T. Kresge, W. J. Roth, M. E. Leonowicz, S. B. McCullen, S. D. Hellring, J. S. Beck, J. L. Schlenker, D. H. Olsen, E. W. Sheppard, *Chem. Mater*. **1994**, *6*, 2317.

39.   P. T. Tanev, T. J. Pinnavaia, *Science* **1995**, *267*, 865.

40.   G. S. Attard, J. C. Glyde, C. G. Göltner, *Nature* **1995**, *378*, 366.

41.   K. M. McGrath, D. M. Dabbs, N. Yao, I. A. Aksay, S. M. Gruner, *Science* **1997**, *277*, 552.

42.   J. S. Beck, J. C. Vartuli, G. J. Kennedy, C. T. Kresge, W. J. Roth, S. E. Schramm, *Chem. Mater*. **1994**, *6*, 1816.

43.   J. C. Vartuli, C. T. Kresge, M. E. Leonowicz, A. S. Chu, S. B. McCullen, I. D. Johnson, E. W. Sheppard, *Chem. Mater*. **1994**, *6*, 2070.

44.   C.-Y. Chen, S. L. Burkett, H.-X, Li, M. E. Davis, *Microporous Mater*. **1993**, *2*, 27.

45.   A. Steel, S. W. Carr, M. W. Anderson, *J. Chem. Soc., Chem. Commun*. **1994**, 1571.

46. A. Monnie, F. Schüth, Q. Huo, D. Kumar, D. Margolese, R. S. Maxwell, G. D. Stucky, M. Krishnamurty, P. Petroff, A. Firouzi, M. Janicke, B. F. Chmelka, *Science* **1993**, *261*, 1299.

47. G. D. Stucky, A. Monnie, F. Schüth, Q. Huo, D. Margolese, D. Kumar, M. Krishnamurty, P. Petroff, A. Firouzi, M. Janicke, B. F. Chmelka, *Mol. Cryst. Liq. Cryst.* **1994**, *240*, 187.

48. (a) T. Yanagisawa, T. Shimizu, K. Kuroda, C. Kato, *Bull. Chem. Soc. Jpn*. **1990**, *63*, 988; (b) S. Inagaki, Y. Fukushima, K. Kuroda, *J. Chem. Soc., Chem. Commun*. **1993**, 680; (c) Y. Fukushima, S. Inagaki, *Mater. Sci. Eng. A.* **1996**, *217*, 116.

49. A. Firouzi, D. Kumar, L. M. Bull, T. Besier, P. Sieger, Q. Huo, S. A. Walker, J. A. Zasadzinski, C. Glinka, J. Nicol, D. Margolese, G. D. Stucky, B. F. Chmelka, *Science* **1995**, *267*, 1138.

50. S. Ikeda, *Surfactants in Solution*, Vol. 2 (Eds.: K. L. Mittal, B. Lindman), Plenum, New York, **1984**, pp. 825.

51. A. Firouzi, F. Atef, A. G. Oertli, G. D. Stucky, B. F. Chmelka, *J. Am. Chem. Soc*. **1997**, *119*, 3596.

52. O. Regev, *Langmuir* **1996**, *12*, 4940.

53. Q. Huo, D. I. Margolese, U. Ciesla, D. G. Demuth, P. Feng, T. E. Gier, P. Sieger, A. Firouzi, B. F. Chmelka, F. Schüth, G. D. Stuck, *Chem. Mater*. **1994**, *6*, 1176.

54. J. C. Vartuli, C. T. Kresge, W. J. Roth, S. B. McCullen, J. S. Beck, K. D. Schmitt, M. E. Leonowicz, J. D. Lutner, E. W. Sheppard, *Proceedings of the 209th ACS National Meeting, Division of Petroleum Chemistry* **1995**, pp. 21.

55. S. A. Bagshaw, E. Prouzert, T. J. Pinnavaia, *Science*, **1995**, *269*, 1242.

56. (a) R. Ryoo, J. M. Kim, C. H. Ko, C. H. Shin, *J. Phys. Chem*. **1996**, *100*, 17718; (b) R. Ryoo, J. M. Kim, C. H. Shin, J. Y. Lee, *Progress in Zeolite and Microporous Materials,*

Studies in Surface Science and Catalysis, Vol. 105 (Eds.: H. Chon, S.-K. Ihm, Y. S. Uh), Elsevier, Amsterdam, **1997**, pp. 45.

57.   A. Corma, M. T. Navarro, J. Perez-Pariente, *J. Chem. Soc., Chem. Commum.* **1994,** 147.

58.   J. S. Reddy, I. L. Moudrakovski, A. Sayari, *J. Chem. Soc., Chem. Commum.* **1994,** 1059.

59.   P. T. Tanev, M. Chibwe, T. J. Pinnavaia, *Nature* **1994**, *368*, 321.

60.   A. Sayari, C. Danumah, I. L. Moudrakovski, *Chem. Mater.* **1995**, *7*, 813.

61.   Z. Luan, C.-F. Cheng, W. Zhou, J. Klinowski, *J. Phys. Chem.* **1995**, *99*, 1018.

62.   G. Fu, C. A. Fyfe, W. Schwieger, G. T. Kokotailo, *Angew. Chem. Int. Ed. Engl.* **1995**, *34*, 1499.

63.   D. Zhao, D. Goldfarb, *J. Chem. Soc., Chem. Commum.* **1995,** 875.

64.   T. M. Abdel-Fattah, T. J. Pinnavaia, *Chem. Commum.* **1996,** 665.

65.   C.-F. Cheng, H. He, W, Zhou, J. Klinowski, J. A. S. Goncalves, L. F. Gladden, *J. Phys. Chem.* **1996**, *100*, 390.

66.   C.-F. Cheng, J. Klinowski, *J. Chem. Soc., Faraday Trans.* **1996**, *92*, 289.

67.   K. A. Koyano, T. Tatsumi, *Chem. Commum.* **1996,** 145.

68.   A. Tuel, S. Gontier, *Chem. Mater.* **1996**, *8*, 114.

69.   A. Tuel, S. Gontier, R. Teissier, *Chem. Commum.* **1996,** 651.

70.   N. Ulagappan, C. N. R. Rao, *Chem. Commum.* **1996,** 1047.

71.   W. Zhang, T. J. Pinnavaia, *Catal. Lett.* **1996**, *38*, 261.

72.   W. Zhang, J. Wang, P. T. Tanev, T. J. Pinnavaia, *Chem. Commum.* **1996,** 979.

73.   B. Echchahed, A. Moen, D. Nicholson, L. Bonneviot, *Chem. Mater.* **1997**, *9*, 1716.

74.   N.-Y. He, J.-M. Cao, S.-L. Bao, Q.-H. Xu, *Mater. Lett.* **1997**, *31*, 133.

75.   D. J. Jones, J. Jiménez-Jiménez, A. Jiménez-López, P. Maireles-Torres, P. Olivera-Pastor, E. Rodriguez-Castellón, J. Rozière, *Chem. Commum.* **1997,** 431.

76. L. Zhang, J. Y. Ying, *AIChE J.* **1997**, *43*, 2793.

77. M. S. Wong, H. C. Huang, J. Y. Ying, unpublished results.

78. D. M. Antonelli, J. Y. Ying, *Angew. Chem. Int. Ed. Engl.* **1995**, *34*, 2014.

79. D. M. Antonelli, J. Y. Ying, *Angew. Chem. Int. Ed. Engl.* **1996**, *35*, 426.

80. S. A. Bagshaw, T. J. Pinnavaia. *Angew. Chem. Int. Ed. Engl.* **1996**, *35*, 1102.

81. A. Sayari, I. L. Moudrakovski, J. S. Reddy, C. I. Ratcliffe, J. A. Ripmeester, K. F. Preston, *Chem. Mater.* **1996**, *8*, 2080.

82. A. Sayari, V. R. Karra, J. S. Reddy, I. L. Moudrakovski, *Chem. Commum.* **1996,** 411.

83. T. Abe. A. Taguchi, M. Iwamoto, *Chem. Mater.* **1995,** *7*, 1429.

84. T. Doi, T. Miyake, *Chem. Commum.* **1996,** 1635.

85. M. J. Hudson, J. A. Knowles, *J. Mater. Chem.* **1996**, *6*, 89.

86. J. S. Reddy, A. Sayari, *Catal. Lett.* **1996**, *38*, 219.

87. U. Ciesla, S. Schacht, G. D. Stucky, K. K. Unger, F. Schüth, *Angew. Chem. Int. Ed. Engl.* **1996**, *35*, 541.

88. P. Liu, J. S. Reddy, A. Adnot, A. Sayari, *Mater. Res. Soc. Symp. Proc.* **1996**, *431*, 101.

89. (a) P. V. Braun, P. Osenar, S. I. Stupp, *Nature* **1996**, *380*, 325; (b) V. Tohver, P. V. Braun, M. U. Pralle, S. I. Stupp, *Chem. Mater.* **1997**, *9,* 1495.

90. J. Li, L. Delmotte, H. Kessler, *Chem. Commun.* **1996**, 1023.

91. D. M. Antonelli, A. Nakahira, J. Y. Ying, *Inorg. Chem.* **1996**, *35*, 3126.

92. D. M.Antonelli, J. Y. Ying, *Chem. Mater.* **1996**, *8*, 874.

93. M. S. Wong,; D. M. Antonelli, J. Y. Ying, *Nanostruc. Mater.* **1997**, *9*, 165.

94. P. Liu, J. Liu, A. J. Sayari, *Chem. Commun.* **1997**, 577.

95. Z. R. Tian, J. Y. Wang, N. G. Duan, V. V. Krishnan, S. L. Suib, *Science* **1997**, *276*, 926.

96. D. M. Antonelli, *Micro. Meso. Mater.* **1999**, *30*, 315.

97. M. Thieme, F. Schüth, *Micro. Meso. Mater.* **1999,** *27*, 193.

98. S. Cabrera, J. E. Haskouri, A. Beltrán-Porter, D. Beltrán-Porter, M. D. Marcos, P. Amorós, *Solid State Science* **2000**, *2*, 513.

99. A. Kim, P. Bruinsma, Y. Chen, L.-Q. Wang, J. Liu, *Chem. Commun.* **1997**, 161.

100. M. S. Wong, J. Y. Ying, *Chem. Mater.* **1998**, *10*, 2067.

101. U. Cielsa, D. Demuth, R. Leon, P. M. Petroff, G. Stucky, K. Unger, F. Schüth, *J. Chem. Soc., Chem. Commun.* **1994**, 1387.

102. F. Vaudry, S. Khodabandeh, M. E. Davis, *Chem. Mater.* **1996**, *8*, 1451.

103. S. Cabrera, J. El Haskouri, J. Alamo, A. Beltrán, D. Beltrán, S. Mendioroz, M. Dolores Marcos and P. Amorós, *Adv. Mater.* **1999**, *11*, 379.

104. W. Zhang, T. J. Pinnavaia, *Chem. Commun.* **1998**, 1185.

105. D. Zhao, Z. Luan, L. Kevan, *Chem. Commun.* **1997**, 1009.

106. J. Y. Ying, C. P. Mehnert, M. S. Wong, *Angew. Chem. Int. Ed.* **1999**, *38*, 56.

107. Y. Traa, B. Urger, J. Weitkamp, *Micro. Meso. Mater.* **1999**, *30*, 3.

108. F. Schüth, *Ber. Bunsenges. Phys. Chem.* **1995**, *99*, 1306.

109. A. Corma, M. S. Grande, V. Gonzales-Alfaro, A. V. Orchilles, *J. Catal.* **1996**, *159*, 375.

110. A. Corma, A. Martinez, V. Martinez-Soria, J. B. Monton, *J. Catal.* **1995**, *153*, 25.

111. J.-H.. Kim, M. Tanabe, M. Niwa, *Microporous Mater.* **1997**, *10*, 85.

112. S. B. Pu, J. B. Kim, M. Seno, T. Inui, *Microporous Mater.* **1997**, *10*, 25.

113. A. Corma, M. T. Navarro, J. Perez-Pariente, *J. Chem. Soc., Chem. Commum.* **1994**, 147.

114. P. T. Tanev, M. Chibwe, T. J. Pinnavaia, *Nature* **1994**, *368*, 321.

115. T. Blasco, A. Corma, M. T. Navarro, J. Perez-Pariente, *J. Catal.* **1995**, *156*, 65.

116. M. Morey, A. Davidson, G. Stucky, *Microporous Mater.* **1996**, *6*, 99.

117. S. A. Bagshaw, F. D. Renzo, F. Fajula, *Chem. Commun.* **1996**, 2209.

118. K. A. Koyano, T. Tatsumi, *Microporous Mater.* **1997**, *10*, 259.

119. A. Tuel, S. Gontier, R. Teissier, *Chem. Commun.* **1996**, 651.

120. K. M. Reddy, I. Moudrkovski, A. Sayari, *J. Chem. Soc., Chem. Commun.* **1994**, 1059.

121. J. S. Reddy, A. Sayari, *Chem. Commun.* **1995**, 2231.

122. K. J. Chao, C. N. Wu, H. Chang, L. J. Lee, S. Hu, *J. Phys. Chem. B.* **1997**, *101*, 6341.

123. S. Gontier, A. Tuel, *Microporous Mater.* **1995**, *5*, 161.

124. Z. Y. Tuan, S. Q. Liu, T. H. Chen, J. Z. Wang, H. X. Li, *J. Chem. Soc., Chem. Commun.* **1995**, 973.

125. T. Abe, Y. Tachibana, T. Uematsu, M. Iwamoto, *J. Chem. Soc., Chem. Commun.* **1995**, 1617.

126. B. Echchahed, A. Moen, D. Nicholson, L. Bonneviot, *Chem. Mater.* **1997**, *9*, 1716.

127. A. Jentys, N. H. Pham, H. Vinek, M. English, J. A. Lercher, *Microporous Mater.* **1996**, *6*, 13.

128. U. Oberhagemann, I. Kinski, I. Dierdorf, B. Marler, H. Gies, *J. Noncryst. Solids* **1996**, *197*, 145.

129. A. Sayari, C. Danumah, I. L. Moudrakovski, *Chem. Mater.* **1995**, *7*, 813.

130. A. Sayari, I. L. Moudrakovski, C. Danumah, C. I. Ratcliffe, J. A. Ripmeester, K. F. Preston, *J. Phys. Chem.* **1995**, *99*, 16373.

131. D. T. On, P. N. Joshi, S. Kaliaguine, *J. Phys. Chem.* **1996**, *100*, 6743.

132. T. K. Das, K. Chaudhari, A. J. Chandwadkar, S. Sivasanker, *J. Chem. Soc., Chem. Commun.* **1995**, 2495.

133. U. Junges, W. Jacobs, I. Voigt-Martin, B. Krutzsch, F. Schüth, *J. Chem. Soc., Chem. Commun.* **1995**, 2283.

134. T. Maschmeyer, F. Rey, G. Sanker, J. M. Thomas, *Nature* **1995**, *378*, 159.

135. J. M. Thomas, *Chem. Eur. J.* **1997**, *3*, 1557.

136. M. Morey, A. Davidson, H. Eckert, G. Stucky, *Microporous Mater.* **1996**, *8*, 486.

137. U. Junges, F. Schüth, G. Schmid, Y. Uchida, R. Schlögl, B. Bunsenges, *Physikal. Chem*. **1997**, *101*, 1631.

138. P. Behrens, *Angew. Chem. Int. Ed*. **1996**, *35*, 515.

139. A. Jentys, W. Schiesser, H. Vinek, *Stud. Surf. Sci. Catal*. **2000**, *130B*, 1523.

140. G. Busca, L. Lietti, G. Ramis, F. Berti, *Appl. Catal. B*, **1998**, *18*, 1.

141. A. Fritz, V. Pitchon, *Appl. Catal. B*, **1997**, *13*, 1.

142. K. C. C. Kharas, D.-J. Liu, H. J. Robota, *Catal. Today* **1995**, *26*, 129.

143. M. Shelef, *Chem. Rev.* **1995**, *95*, 209.

144. H. Bosch, F. Janssen, *Catal. Today* **1988**, *2*, 369.

145. M. Hatanaka, et al. *Eur. Pat. Appl*. **2000**.

146. S. Higashimoto, et al. *Chem. Lett*. **2000**, *4*, 408.

147. W. Schiesser, et al. *Catal. Lett*. **1999**, *56*, 189.

148. G. Moretti, et al. *Appl. Catal. B* **1999**, *20*, 67.

149. T. J. Pinnavaia, W. Zhang, *Stud. Surf. Sci. Catal.* **1998**, *117*, 23.

150. C. K. Narula, et al. *Ceram. Trans*. **1997**, *73*, 15.

151. R. A. Sheldon, J. K. Kochi, *Metal-catalyzed Oxidations of Organic Compounds*, Academic Press, New York, **1981**.

152. M. Nakao, S. Nishiyama, S. Tsuruya, M. Masai, *Inorg. Chem*. **1992**, *31*, 4662.

153. G. R. Dube, V. S. Darshane, *J. Chem. Soc., Faraday Trans*. **1992**, *88*, 1299.

154. H. Hayashibara, S. Nishiyama, S. Tsuruya, M. Masai, *J. Catal*. **1995**, *153*, 254.

155. M. Arai, A. Nishiyama, S. Tsuruya, M. Masai, *J. Chem. Soc., Faraday Trans*. **1996**, *92*, 2631.

156. H.-F. Chang, M. A. Saleque, W.-S. Hsu, W.-H. Lin, *J. Mol. Catal. A: Chem.* **1996**, *109*, 249.

157. M. Genta, S. Nishiyama, S. Tsuruya, M. Masai, *J. Chem. Soc., Faraday Trans.* **1996**, *92*, 1267.

158. H.-F. Chang, C-F. Yang, *Ind. Eng. Chem. Res.* **1997**, *36*, 2080.

159. Y.-J. Tu, Y.-W. Chen, *Ind. Eng. Chem. Res*. **1998**, *37*, 2618.

160. W. Aquila, H. Fuchs, O. Worz, W. Ruppel, K. Halbritter, US patent 6013843, **2000**.

161. J. Wulff-Doring, J.-P. Melder, G. Schulz, G. Voit, G. Frank, W. Harder, US patent 6046359, **2000**.

Chapter 2. Synthesis and Characterization of Mesoporous Titanium Oxide

2.1. Introduction

Many applications of MCM-41 have been explored in a wide variety of catalytic processes[1-3] since Mobil researchers[4,5] first demonstrated the synthesis of mesoporous silicate and aluminosilicate materials (MCM-41) by a micelle-assisted crystallization of the inorganic phase. However, transition metal analogues still remain very rare, although there have been many attempts to extend the synthetic methodology to the preparation of mesoporous transition metal oxide structures.[6-18] The most important drawbacks for application of mesoporous transition metal oxides are their low thermal stability, low surface areas, tedious synthetic routes, poorly clarified formation mechanisms and surface compositions. The quality of the mesoporous materials strongly depends on the synthetic conditions, e.g. choice of metal precursors and surfactants that determines the strength of metal-surfactant interactions, methods to remove templates, calcination temperatures, etc.

Surfactant templating method has been successfully used in the synthesis of mesoporous niobium[12] and tantalum[13] oxides, and a strong interaction between the inorganic precursor and the surfactant, e.g. covalent bonding, is presumed as one of the essential requirements for high-quality mesoporous materials. Therefore we adopted templating method to prepare mesoporous titanium oxide. We have endeavored to choose proper metal precursors and surfactants, and to prepare a covalent compound that is believed to be an ideal precursor for high quality mesoporous titanium oxide.

Preventing pore structures from collapsing at high calcination temperatures is amongst the most important aspects in the area of mesoporous transition metal oxide materials. Ciesla *et al.* found that post-synthetic treatment with phosphoric acid stabilized mesoporous zirconium oxide framework.[7] These materials were thermally stable up to 500 °C and their

BET surface areas were as high as 500 m^2g^{-1}. The high thermal stability was supposed to be achieved by a crystallization delay due to the presence of phosphate groups. This method has also been confirmed in the preparation of titanium oxo-phosphate by Thieme *et al.*[9] In this chapter, different methods are carried out to prevent pore structures from collapsing.

2.2. Results and Discussion

2.2.1. Synthesis and Characterization of As-synthesized Mesoporous Titanium Oxide

Initial attempts to synthesize mesoporous titania following the synthetic route published by Ying et al.[12] failed. The ^{1}H- and ^{13}C-NMR of a mixture of titanium isopropoxide and 1-dodecylamine clarified that no covalent bonding existed between titanium and the template head group. Enlightened by the synthesis strategy of mesoporous niobium[11,12] and tantalum[13] oxides, we assume that the formation of a covalent complex $Ti(OC_3H_7)_3[HN(CH_2)_{11}CH_3]$ is a very important factor at the first synthesis stage of mesoporous titania. In the cases of niobium[11,12] and tantalum[13], the amine surfactant head group was covalently bonded to the metal center prior to hydrolysis and condensation. Both the mesoporous niobium oxide and tantalum oxide showed high thermal stability over 400 °C. In contrast, when the same amine surfactant was used in the synthesis of phosphorus-free mesoporous titania, where the template was hydrogen-bonded into the structure, the obtained mesoporous titania was only thermally stable to 300 °C.[15] The weak metal-template interaction is assumed responsible for the poor mesoscopic order and the low thermal stability.

Although mixing $Ti(O^iPr)_4$ with one equivalent of 1-dodecylamine at room temperature did not result in a significant reaction, as monitored by ^{1}H-NMR, distilling off the generated ^{i}PrOH from the reaction mixture led to the formation of analytically pure complex $Ti(OC_3H_7)_3[HN(CH_2)_{11}CH_3]$ (Equation 2.1). The compound was characterized by elemental

analysis and ^{1}H-NMR spectroscopy, and was used to prepare as-synthesized mesoporous titania.

$$\text{Ti(OPr}^i)_4 + \text{~~~~~NH}_2 \xrightarrow{-\ ^i\text{PrOH}} \text{(structure)} \quad (2.1)$$
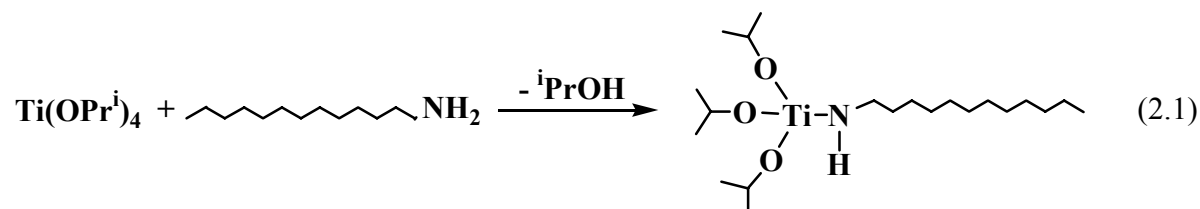
Initial attempts of hydrolysis in water following the procedure for synthesizing mesoporous niobium oxide[12] failed due to the rapid precipitation of oxide-alkoxide aggregate. The analyzed compositions of C, H and N in the resulting precipitate were much lower than the expected, and no distinguished reflections were observed in the XRD pattern. However, the as-synthesized material was successfully synthesized in our lab by hydrolysis in an [i]PrOH-H_2O co-solvent that functioned to restrain the hydrolysis rate.

The X-ray diffraction pattern of the as-synthesized mesoporous titania (Fig. 2.1a) gives a single broad reflection at d-spacing of 3.2 nm. This reflection can be indexed as (100) assuming a hexagonal unit cell. The low intensity reflections (110), (200) and (210) which appeared in the XRD pattern of the as-synthesized Ti-TMS1[10] are not evident in our examples. Although this phenomenon has been attributed to either disordered packing of individual tubes in mesostructures or very small crystalline size,[10,15] materials with only one distinct XRD reflection have also been found to contain a substantial amount of MCM-41 structure.[8] The XRD of an as-made sample prepared from Ti(OMe)$_4$ and a C$_{12}$-surfactant Dodecanol +5 EO also showed a single diffraction peak.[9] Therefore it is not reliable to determine the degree of order solely on the number of reflections.

The TGA curve of the as-synthesized material (Fig. 2.2a) reveals two decomposition steps between 210 and 600 ^{o}C after desorption of water, corresponding to the decomposition
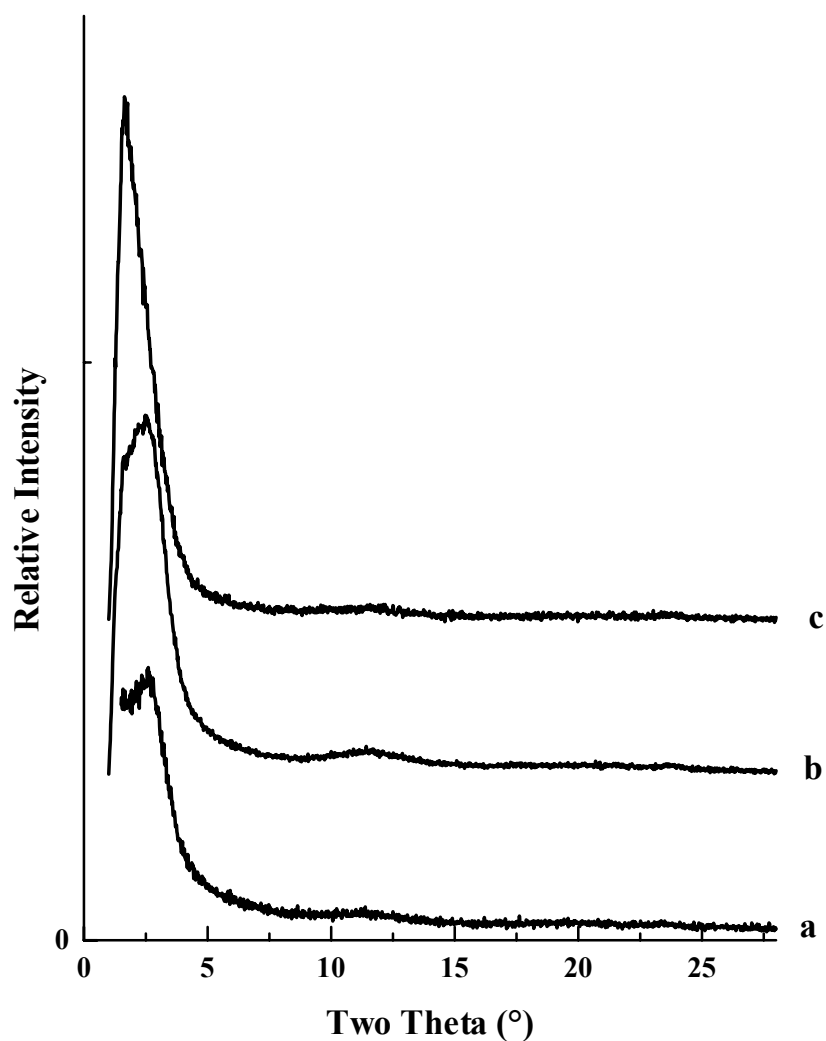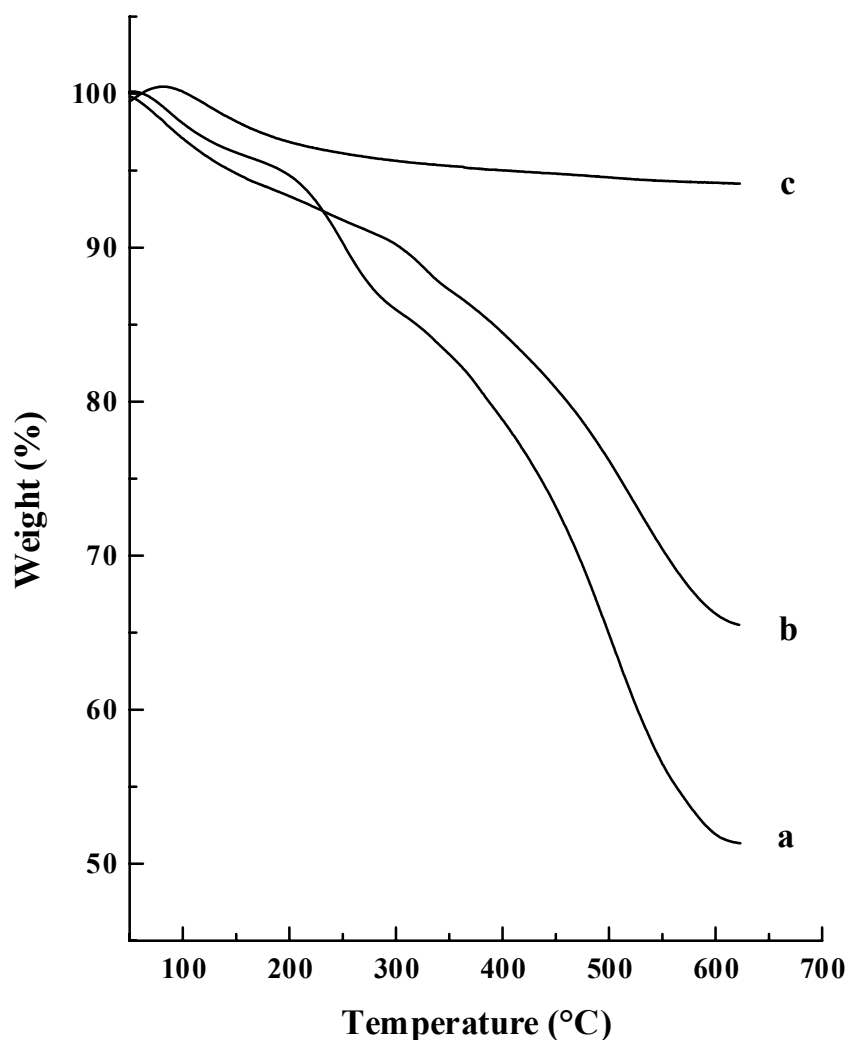
Figure 2.1 XRD diffraction patterns of (a) as-synthesized mesoporous titania, (b) mesoporous titanium oxo-phosphate before calcination, (c) mesoporous titanium oxo-phosphate after calcination.

of the organic template. The overall weight loss of 43.8% in this temperature range correlates with the total weight amount of C, H and N elements (44.41%) determined by elemental analysis. The strong IR vibrational bands in the region of 2800-3000 cm^{-1} originate from C-H stretches of the template.

2.2.2. Mesoporous Titanium Oxo-phosphate

Removing the surfactants completely but keeping pore structure from collapsing is a key step to obtain mesoporous titania with a high surface area, unique pore size and high thermal stability. As to the as-synthesized materials described in section 2.2.1, the complete removal of surfactants without destroying pore structures by utilizing acid extraction or calcination independently was not successful.


Figure 2.2 TGA plots of (a) as-synthesized mesoporous titania, (b) mesoporous titanium oxo-phosphate before calcination, (c) mesoporous titanium oxo-phosphate after calcination.

In principle, a proton source is required to achieve removal of amine surfactants. It has been reported that the long chain amine templates can be removed from Ta-TMS1 as-made material by alternative of three acid sources: triflic acid, nitric acid and ammonium tetraphenylborate.[13] Moreover, phosphorous-free titania was obtained by using *p*-toluene sulphonic acid extraction.[15] However, in our cases, treatment with 0.1 M triflic acid destroyed the pore structure. Treatment with 0.1 M nitric acid partially removed the surfactant and preserved the porous structure, as evidenced by a single XRD peak at d spacing of 5.5 nm. The remained template of ca. 8% was subsequently removed by calcination at 350 $^{\circ}$C for 8 h. The obtained material shows an XRD reflection at d = 5.8 nm and a BET surface area of 170 m^{2}g^{-1}. The low surface area is probably due to partial pore structure damage caused by strong acid — nitric acid — treatment.

2.2.2.1. Synthesis and Characterization of Mesoporous Titanium Oxo-phosphate Using 1-dodecylamine as Template

Considering the stabilization effect of phosphoric acid to the mesopore structures,[7,9] post-synthetic treatment with phosphoric acid has been adopted in the preparation of mesoporous titanium oxo-phosphate.

The as-synthesized material, using 1-dodecylamine as surfactant, was treated with phosphoric acid (pH = 0.5) for 3 h, and then collected and washed with water and ethanol, dried at 120 °C for 2 h. It has been revealed by TGA (Fig. 2.2b) and elemental analysis that 24% of the template remains in the material. C-H stretches of the template in the region of 2800 to 3000 cm^{-1} still exist in the IR spectrum. Another characteristic peak around 1030 cm^{-1} comes from P=O stretches of phosphate. The XRD shows a broad reflection centered at d = 3.6 nm, which is 0.4 nm higher and slightly more intense than that of the as-synthesized material (Fig. 2.1b).
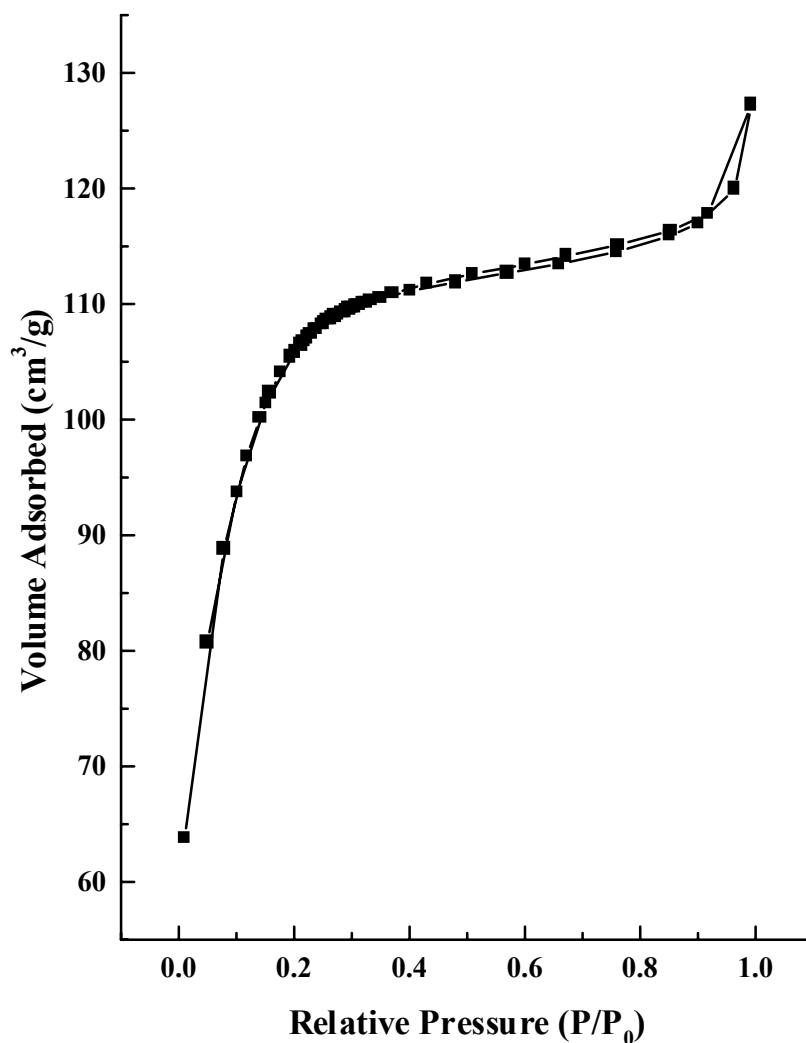
Figure 2.3 Nitrogen-adsorption-desorption isotherm of mesoporous titanium oxo-phosphate obtained by post-synthetic treatment with phosphoric acid.

After calcination at 400 °C, the retained surfactant was completely removed. This was confirmed by elemental analysis, IR spectrum and TGA analysis (Fig. 2.2c). Both the analyzed C and N percentages are below 0.5%, 1.11% of H comes from the absorbed water, and 14.1% of P indicates that the material is titanium oxo-phosphate. No C-H stretching bands are observed in the IR spectrum. With the exception of desorption of water, no weight loss can be identified in the TGA curve, indicating a surfactant-free material. As shown in Fig. 2.1, the XRD reflection is sharper and more intense than those of the as-synthesized material and of the phosphoric acid treated sample. This is probably attributed to the

enhancement of mesoscopic order in the material. The obtained mesoporous titanium oxo-phosphate exhibits a BET surface area of 368 m^2g^{-1} and an average pore diameter of 2.0 nm (Fig. 2.3). Fig. 2.3 does not show the standard type IV isotherm owing to the existence of a certain amount of micropores. The thermal stability of this material is up to 580 °C as determined by DSC (Fig. 2.6c).

Furthermore we attempted utilizing polyphosphoric acid instead of phosphoric acid owing to the consideration that the rigid long chain of polyphosphoric acid may increase order degree of mesoporous structures thereby enhancing thermal stability. Mesoporous oxo-phosphate material was again successfully obtained. However, the BET surface area decreased to 200 m^2g^{-1} and the average pore diameter increased to 2.2 nm in comparison to the phosphoric acid treated sample.

2.2.2.2. Synthesis and Characterization of Mesoporous Titanium Oxo-phosphate Using 1-dodecanol as Template

For a comparison, we employed 1-dodecanol as template instead of 1-dodecylamine. Using a similar synthesis method for $Ti(O^iPr)_3[NH(CH_2)_{11}CH_3]$, complex $Ti(O^iPr)_3[O(CH_2)_{11}CH_3]$ (Equation 2.2) was obtained from the reaction of titanium isopropoxide with one equivalent of 1-dodecanol. The complex was characterized by ^{1}H-NMR and elemental analysis. The hydrolysis of this complex was carried out in an aqueous hydrochloric acid solution at pH = 1.0. The obtained as-synthesized material was treated with phosphoric acid at pH = 0.5 for 3 h, and then filtered and washed with water and ethanol. The white solid was dried at 120 °C for 2 h and calcined at 450 °C for 4 h. A mesoporous titanium oxo-phosphate with BET-surface area of 320 m^2g^{-1}, which is ca. 50 m^2g^{-1} lower than the material using 1-dodecylamine as template, was obtained. This material is thermally stable up to 550 °C, being 30 °C lower than the material from 1-dodecylamine. The characteristic data

of this material are comparable with those of the mesoporous titanium oxo-phosphate obtained by Schüth and co-workers, in which polyethylenoxide was used as surfactant and the BET-surface area was reported as 350 m^2g^{-1} and the thermal stability being up to 550 ^oC.[9]

$$\text{Ti(OPr}^i)_4 \; + \; \text{/\/\/\/\OH} \; \xrightarrow{\text{- }^i\text{PrOH}} \; \text{>-O-Ti-O/\/\/\/\/} \qquad (2.2)$$
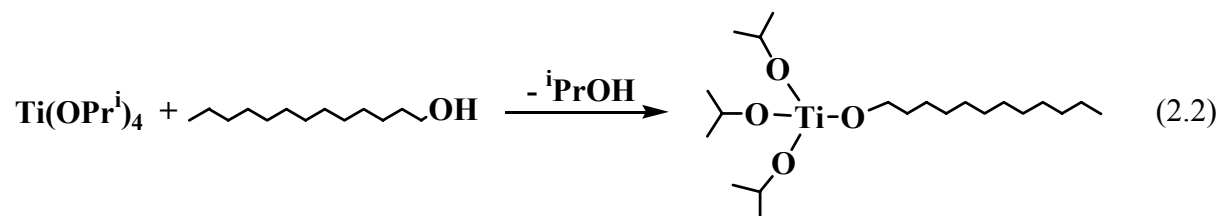
To the as-synthesized material using 1-dodecanol as template, post-synthetic treatment with polyphosphoric acid instead of phosphoric acid was also pursued. In this case, polyphosphoric acid treatment shows a distinct advantage over phosphoric acid in the quality of the mesoporous titamiun oxo-phosphate product. Calcination at 450 °C in a stream of air removed retained surfactant completely and yielded a mesoporous titanium oxo-phosphate with BET-surface area of 503 m^2g^{-1} and average pore size of 2.7 nm (Fig. 2.4). The elemental analysis data of 0.1% of C, 1.69% of H and 12.29% of P indicate a template free titanium oxo-phosphate material. No C-H stretching vibrations are observed in the IR spectrum, but rather a characteristic peak between 1020 and 1050 cm^{-1} attributed to the P=O stretches of polyphosphate. No weight loss can be identified above 200 °C in the TGA curve, confirming a surfactant free material. As illustrated in Fig. 2.5, the XRD reflection with d-spacing of 5.6 nm is sharper and more intense after calcination. A similar phenomenon has also been observed in the preparation process for mesoporous titanium oxo-phosphate from 1-dodecylamine templated material (Fig. 2.1), and is attributed to the enhancement of mesoscopic order in the material.

DSC analysis was applied to determine the thermal stability of the materials. In Fig. 2.6 the thermal stabilities of the mesoporous titanium oxo-phosphates which are stabilized by phosphoric acid and polyphosphoric acid, respectively, are compared with those of the pure

mesoporous titania (section 2.2.4) and "Na$_2$O" doped mesoporous titanium oxide (section 2.2.3). The stabilization effect of phosphate is apparent. The mesoporous titanium oxo-phosphate treated with polyphosphoric acid is thermally stable up to 626 °C. The sharp exothermic peak at 787 °C is related to the phase transformation to a phase mixture of anatase and different titanium phosphates.[9] Its thermal stability is appreciably higher than those of the pure mesoporous titania and "Na$_2$O" doped mesoporous titanium oxide, and even higher than
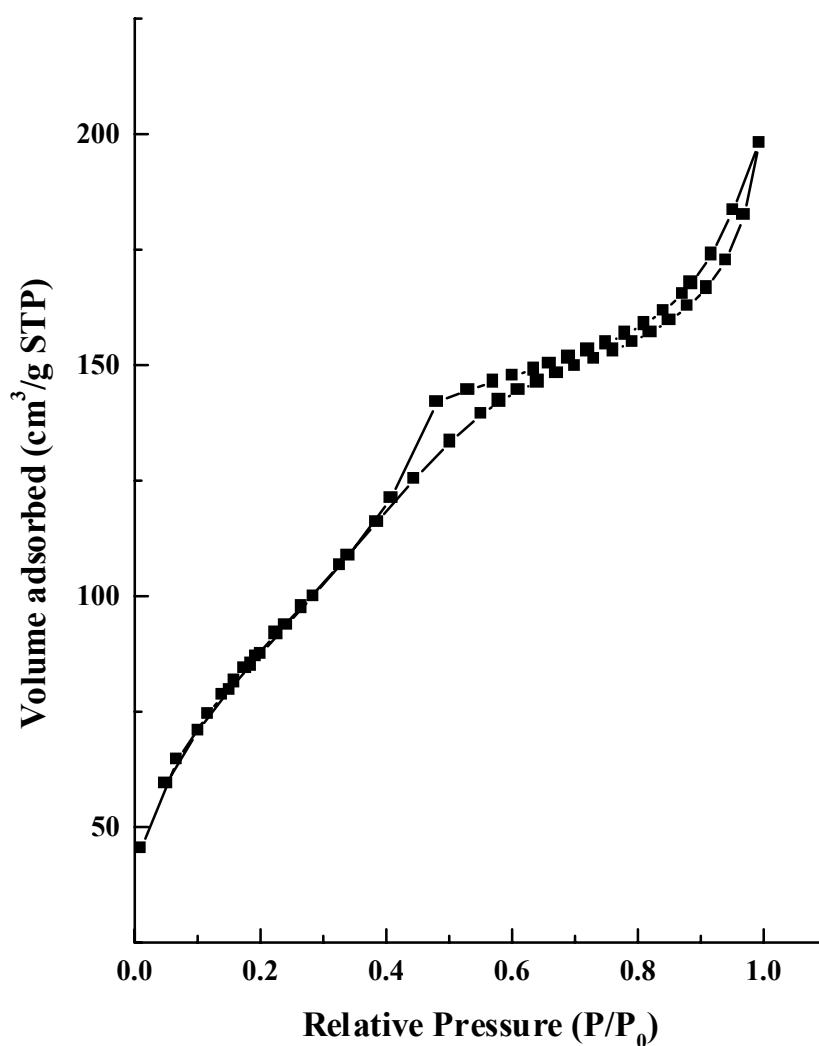
Figure 2.4 Nitrogen adsorption-desorption isotherms of mesoporous titanium oxo-phosphate obtained by post-synthetic treatment with polyphosphoric acid.
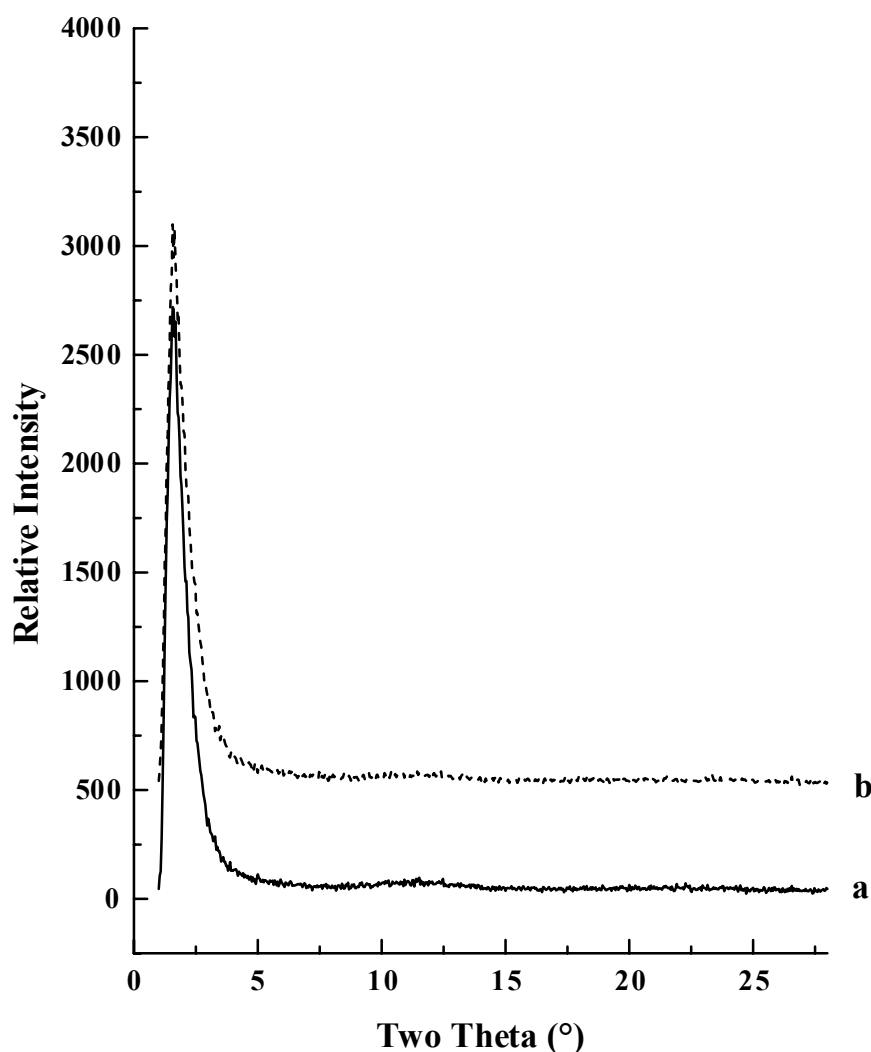
Figure 2.5 XRD diffraction patterns of mesoporous titanium oxo-phosphate obtained by post-synthetic treatment with polyphosphoric acid before calcination (a) and after calcination (b).

those of the phosphoric acid treated sample and the other mesoporous titanium oxo-phosphate reported in the literature.[9,10] Calcination of the mesoporous titanium oxo-phosphate (treated with polyphosphoric acid) at 650 °C destroys the pore structure, leading to the formation of anatase which is indicated by the characteristic anatase reflections in the XRD. The mesoporous titanium oxo-phosphates presented here are among the most thermally stable in the family of mesoporous titanium oxide materials. To our knowledge, it is the first time that polyphosphoric acid has been used to stabilize mesoporous structures. We believe that the

rigid long chain of polyphosphoric acid increases the order degree of the mesoporous structure, resulting in enhancement of the thermal stability.

From above discussion we conclude that both synthetic routes, amine-templating route and alcohol-templating route, can lead to titanium oxo-phosphates with high thermal stability. However, compared to the alcohol-templating route, amine route is more convenient since the hydrolysis is carried out in an ^{i}PrOH-H$_2$O co-solvent; whereas the hydrolysis of Ti(O^{i}Pr)$_3$[O(CH$_2$)$_{11}$CH$_3$] is carried out in an hydrochloric acid solution. Therefore, we select the amine-templating route for the further research.

## 2.2.3. Synthesis and Charaterization of "Na$_2$O" Doped Mesoporous Titanium Oxides

After post-synthetic treatment with phosphoric acid/polyphosphoric acid to the as-synthesized mesoporous titanium oxide formed from amine-templating method, the materials were treated with aqueous sodium hydroxide solution (10%). Exhaustively washing with water removed all phosphate and partial surfactants as evidenced by TGA analysis and IR spectroscopy. It was nevertheless found that sodium was introduced into the material even when exhaustively washing with water until a pH of 7 was reached. This was confirmed by elemental analysis. Calcination at 350 °C removed remaining surfactants completely, and a "sodium oxide" doped mesoporous titania was produced.

Fig. 2.7 shows a comparison of the powder X-ray diffraction patterns of the intermediate and final materials obtained in the preparation process of "Na$_2$O" doped mesoporous titania. All patterns exhibit a single diffraction peak. Higher order Bragg reflections of the hexagonal structure are not resolved. Pinnavaia *et al.* have demonstrated that similar "single-reflection" MCM-41-type materials still have short-range hexagonal symmetry.[19,20] Contrary to the literature reports of the (100) peak broadening upon surfactant removal,[21] in this case, NaOH treatment tends to preserve crystallinity of the material. This is clearly evidenced by the

enhanced scattering intensity and sharpness of the (100) peak.[19,20] Although the d-spacing of the phosphoric acid treated sample (d = 3.56 nm) is only slightly higher than that of the as-synthesized material (d = 3.45 nm), NaOH treated and calcined mesoporous material shows much higher d-spacing (5.66 nm) presumably due to a better condensation of the wall.
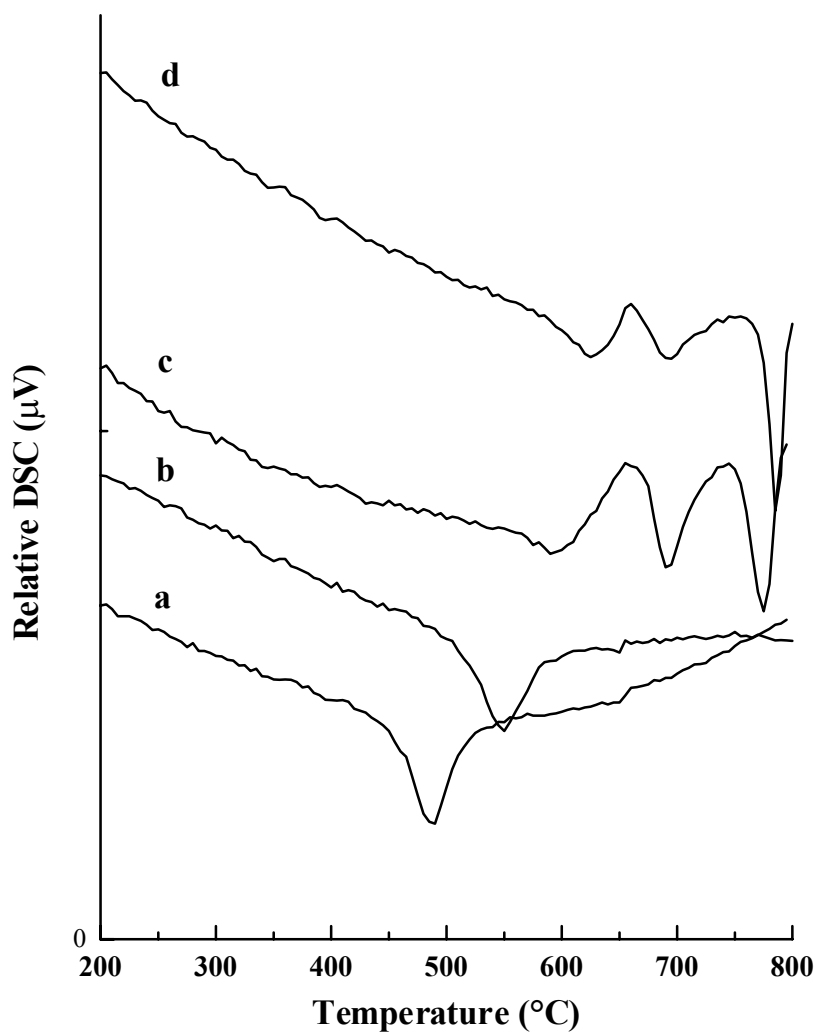


Figure 2.6 DSC plots of (a) pure mesoporous titania, (b) "Na$_2$O" doped mesoporous titania, (c) phosphoric acid treated mesoporous titanium oxo-phosphate, (d) polyphosphoric acid treated mesoporous titanium oxo-phosphate.
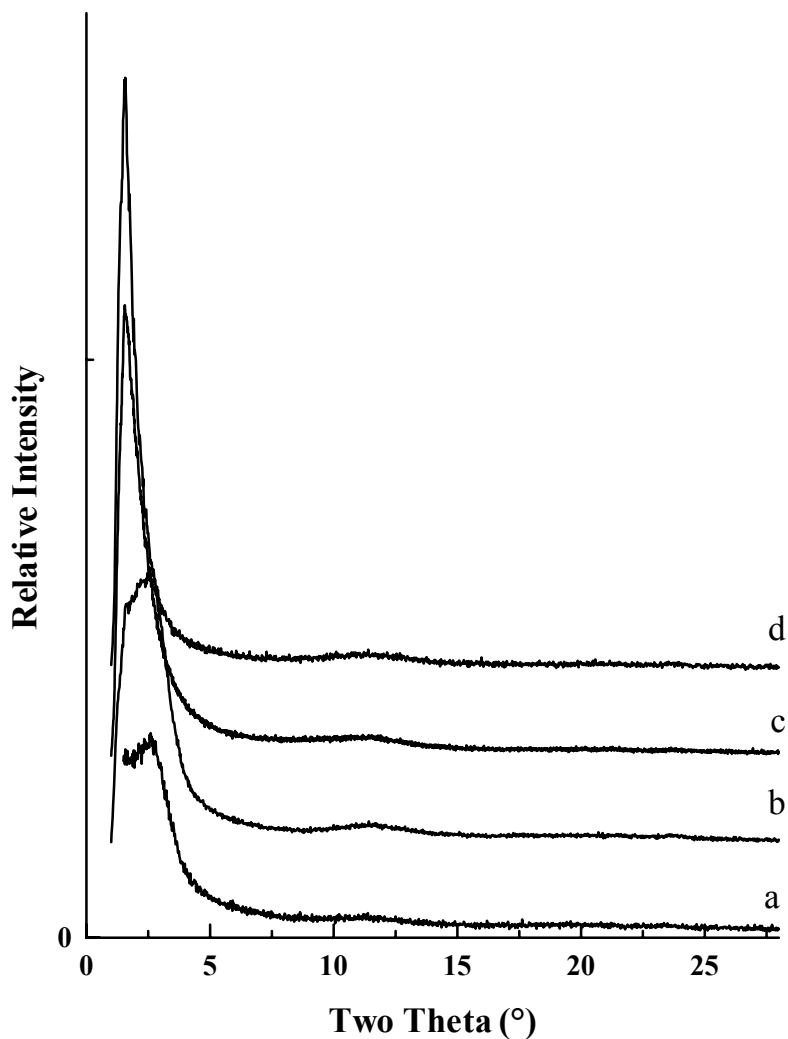
Figure 2.7 X-ray diffraction patterns of (a) as-synthesized mesoporous titania containing 1-dodecylamine, (b) phosphoric acid treated sample, (c) NaOH treated sample and (d) calcined mesoporous titania doped with "Na_2O".

The N_2-adsorption-desorption isotherm of the "Na_2O" doped mesoporous titania is shown in Fig. 2.8, which can be classified as type IV. This type of hysteresis loop is in principal due to cylindrical pores open at both ends. The sharp decline in the desorption curve indicates mesoporisity of the material. The BET surface area is about 390 m^2g^{-1}. The pore size distribution is narrow and the average pore diameter is 3.0 nm.
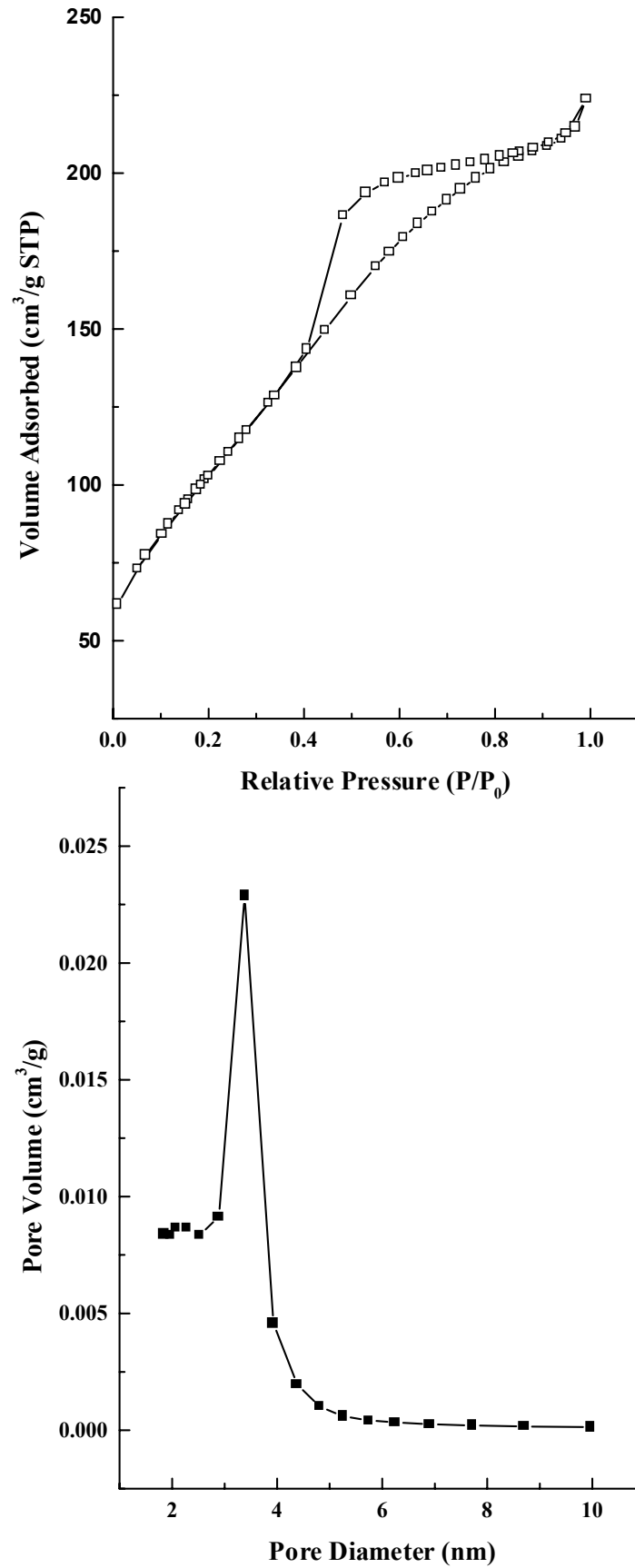
Figure 2.8 N_2-adsorption-desorption isotherm and the pore size distribution of the calcined mesoporous titania doped with "Na_2O".

TGA curves of the materials are presented in Fig. 2.9. The weight loss below 200 °C is due to desorption of water, and that between 200 and 600 °C corresponds to combustion of the template. It was found that the post-synthetic treatment with phosphoric acid removed ca. 29% of surfactants (Fig. 2.9b), which correlates well with the found value of 27% from elemental analysis. It can also be seen that sodium hydroxide treatment removed not only phosphate but also some surfactant (Fig. 2.9c). Calcination at 350 °C removed the remaining surfactant completely. In the TGA curve of the final product there are no traces of weight loss
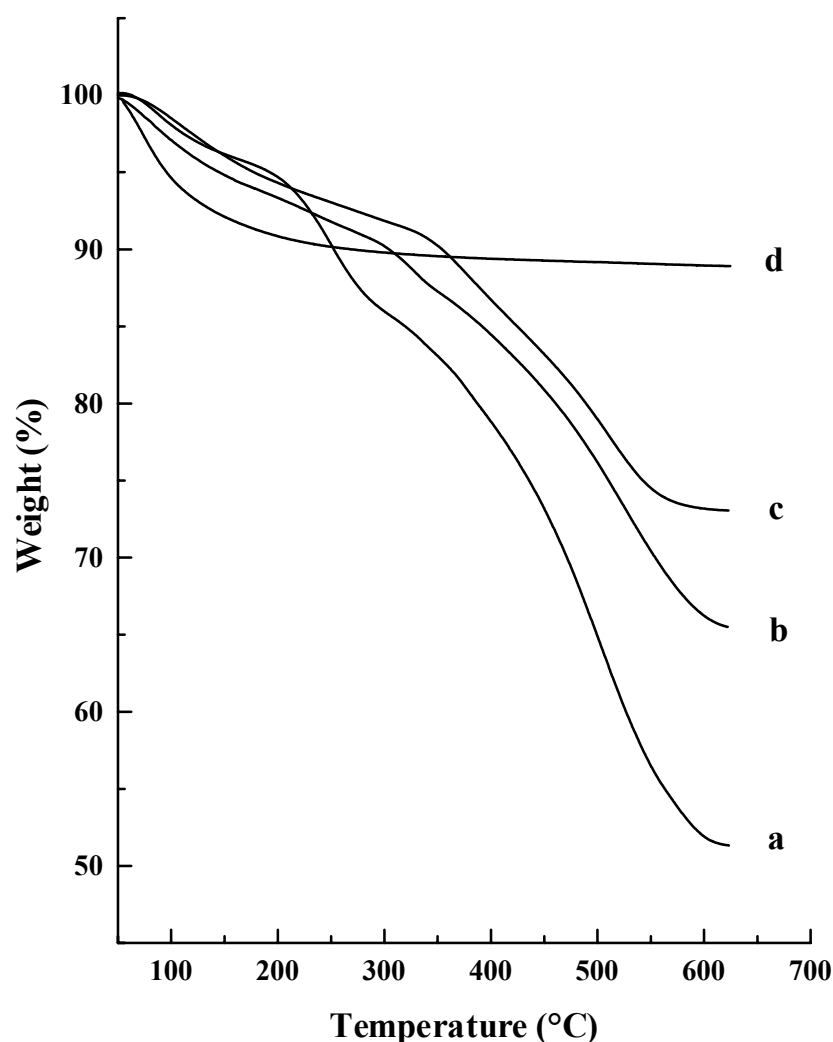
Figure 2.9 TGA plots of (a) as-synthesized mesoporous titania, (b) sample post-treated with phosphoric acid, (c) sample post-treated with sodium hydroxide, (d) "Na_2O" doped mesoporous titanium oxide after calcination.

above 200 °C observed (Fig. 2.9d). Elemental analysis confirmed that the product was a titanium oxide containing Na_2O.

The "Na_2O" doped mesoporous titania has a distinct advantage over the pure mesoporous titania (section 2.2.4) in terms of thermal stability, which is seen from DSC analysis presented in Fig. 2.6. An exothermic peak at 490 °C (Fig. 2.6a) originates from the collapsing of the pure mesoporous titania structure. The corresponding structural collapse exothermic peaks of "Na_2O" doped mesoporous titania materials appear at higher temperature (Fig. 2.6b). Additionally, the thermal stability increases with increasing sodium content, at 530 °C for 4.9%, 550 °C for 5.5% and 575 °C for 7.1% of Na (Fig. 2.10). We propose that titanate formed on the surface of the mesoporous structure contributes to the enhanced thermal stability. This is based on the observation of characteristic XRD reflections of a titanate $Na_2Ti_6O_{13}$ (Fig. 2.11). Table 2.1 presents a detailed comparison of the pure mesoporous titania (section 2.2.4) and the various amount "Na_2O" doped mesoporous titania. The existence of titanates increases the thickness of pore walls, and decreases pore diameters, pore volumes and BET surface areas.

Table 2.1 Characterization data of "Na_2O" doped mesoporous titania.[a]

Na	DSC	S_{BET}	V	D	$d_{(100)}$	wall
wt.%	°C	m^2g^{-1}	cm^3g^{-1}	nm	nm	nm
7.1	575	301	0.276	3.23	5.66	3.30
5.5	550	390	0.301	3.01	5.66	3.52
4.9	530	334	0.301	3.22	5.66	3.31
0.0	490	461	0.459	3.46	5.73	3.16

[a] D = average pore diameter, V = pore volume.
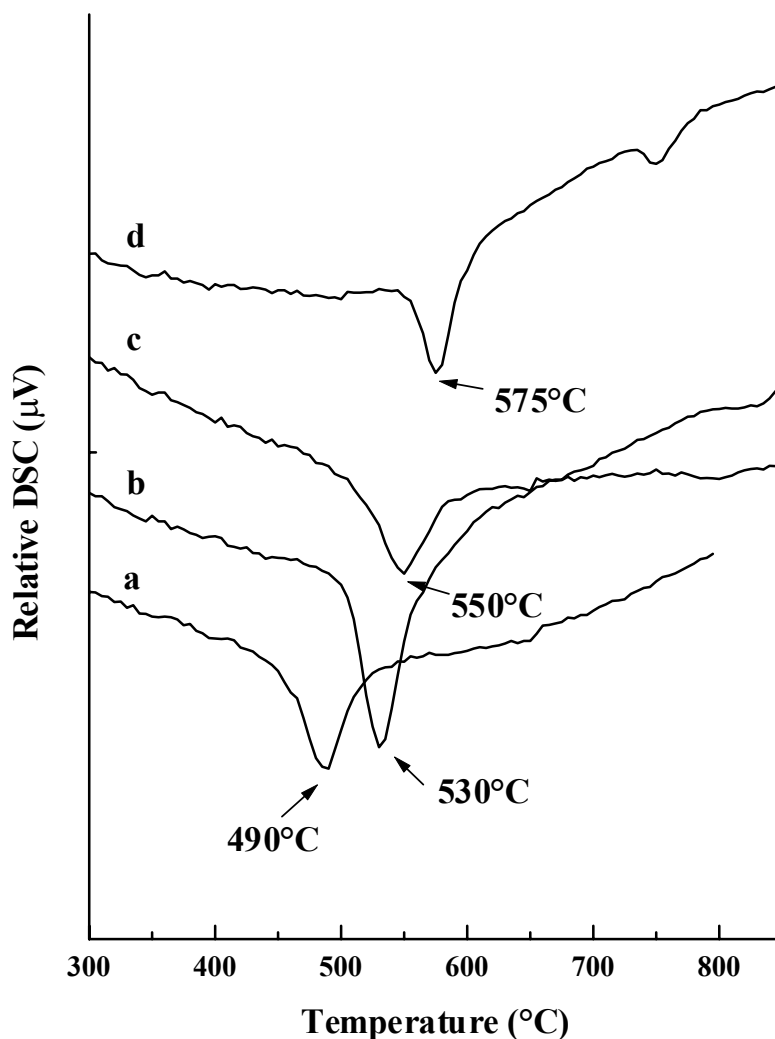
Figure 2.10 DSC curves of the pure mesoporous titania (a) and calcined mesoporous titania doped with "Na$_2$O" containing 4.3% (b), 5.5% (c) and 7.1% (d) of sodium.

A comparison (Table 2.2) of the pore properties between "Na$_2$O" doped mesoporous titania treated with phosphoric acid and that with polyphosphoric acid reveals that the polyphosphoric acid treated sample has a larger pore size (3.60 nm compared to 3.22 nm), thinner pore wall (2.93 nm compared to 3.31 nm), and lower thermal stability (520 °C compared to 530 °C). The lower thermal stability is very likely due to the thinner pore wall.
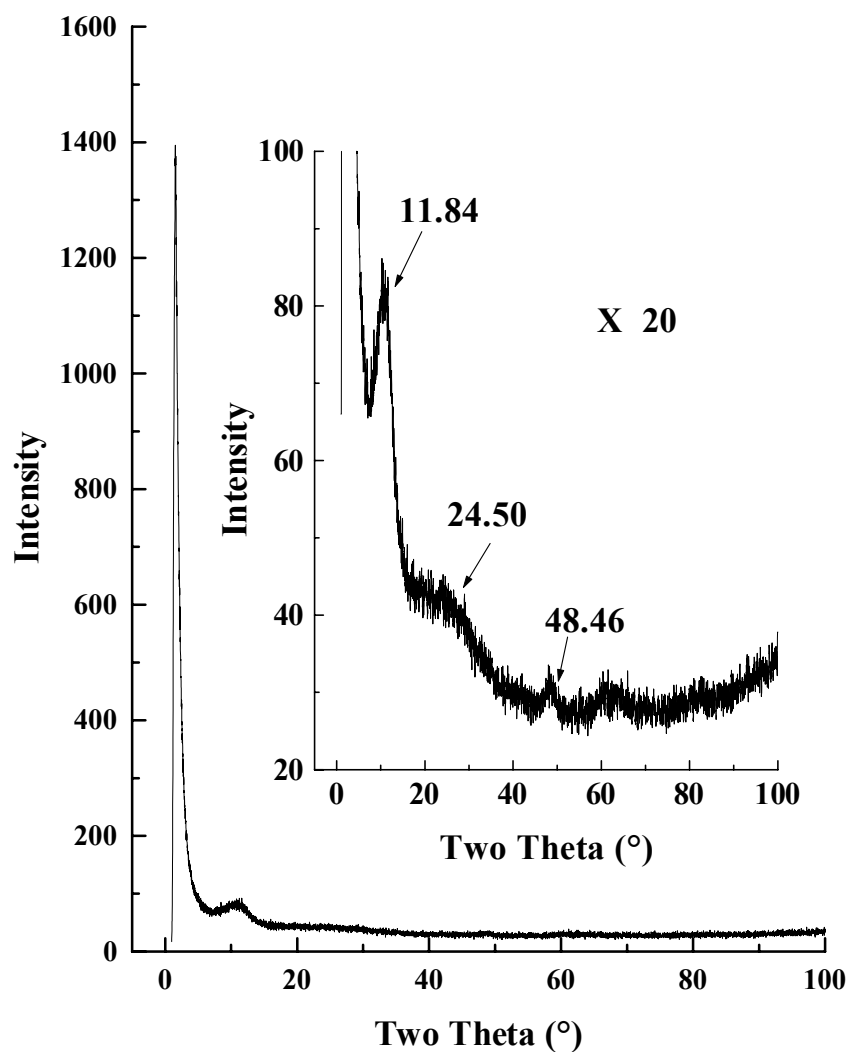
Figure 2.11 XRD pattern of "Na$_2$O" doped mesoporous titania (inserted pattern indicates the existence of titanates Na$_2$Ti$_6$O$_{13}$).

Table 2.2 Effect of Polyphosphoric acid and phosphoric acid treatment to pore structure.

Post-synthetic treatment agent	Na wt.%	S$_{BET}$ m^{2}g^{-1}	V cm^{3}g^{-1}	D nm	d$_{(100)}$ nm	wall nm	DSC °C
Polyphosphoric acid	4.8	312	0.316	3.60	5.66	2.93	520
Phosphoric acid	4.9	334	0.301	3.22	5.66	3.31	530
Polyphosphoric acid	0	578	0.462	3.59	5.59	2.86	430
Phosphoric acid	0	587	0.509	3.37	5.66	3.16	490

2.2.4. Synthesis and Characterization of Pure Mesoporous Titanium Oxides

Our initial aim was to synthesize pure mesoporous titanium oxide with high thermal stability. Since the research pursued in our laboratory has demonstrated that mesoporous structure of titanium oxide can be stabilized by phosphate (section 2.2.2) and "Na$_2$O" (section 2.2.3), thermally stable pure mesoporous titania was expected to be synthesized on the basis of titanium oxo-phosphate and "Na$_2$O" doped mesoporous titanium oxide.

As the post-synthetic treatment with NaOH can remove not only phosphate group but also partial surfactant, as described in section 2.2.3, an attempt to remove amine surfactant from the as-synthesized material was carried out by direct NaOH post-synthetic treatment. A convenient synthetic route to pure mesoporous titania was thereby developed: (1) the reaction of Ti(O^{i}Pr)$_4$ and 1-dodecylamine to produce as-made material; (2) post-synthetic treatment with aqueous NaOH solution; (3) treatment with aqueous HCl; and (4) calcination.

The pale-yellow coloured "Na$_2$O" doped mesoporous titania was obtained by NaOH treatment of the as-made material. Elemental analysis found C 1.59%, H 1.81%, N 0.1% and Na 5.2%, suggesting that almost all of the surfactant were removed. No C-H stretching is observed in the IR spectrum. The isotherm plot and pore size distribution of this "Na$_2$O" doped mesoporous titania are shown in Fig. 2.12a and Fig. 2.13a, respectively. The BET surface area is 354 m^{2}g^{-1}, pore volume is 0.194 cm^3/g and the average pore diameter is 2.5 nm obtained from BJH desorption branch. The pore size distribution is broad due to the existence of "Na$_2$O" on the surface of pores.

The obtained "Na$_2$O" doped mesoporous titania was treated with aqueous HCl solution (1%) in order to remove "Na$_2$O". After extensively washing with water until a pH of 7 was reached and no more Cl$^-$ detected, pure mesoporous titania was obtained. The material was calcined at 350 °C, and was characterized by elemental analysis, IR, TG, DSC, XRD and BET. In the TGA curve no weight loss appears above 200 °C, indicating a template free

material. No C-H stretching is observed in the IR spectrum. The elemental analysis found C 0.06%, H 1.03%, N 0.00, Cl 0.01%, Na 0.1% and Ti 51.42%. XRD shows a sharp reflection at d-spacing of 5.66 nm, indicating mesoporosity of the material. A comparison of pore properties between pure mesoporous titania (before calcination) and "Na$_2$O" doped mesoporous titania revealed that, after "Na$_2$O" was removed from the surface of the pores, the BET surface area increased from 354 to 418 m^{2}g^{-1}, pore volume increased from 0.194 to 0.300 cm^{3}g^{-1}, average pore diameter increased from 2.5 to 2.8 nm, and pore size distribution became narrower. Fig. 2.12b and 2.12c show the standard type IV isotherm plots of the materials before and after calcination at 350 °C. After calcination, the BET surface area decreased to 342 m^{2}g^{-1}, pore volume decreased to 0.241 cm^{3}g^{-1} and average pore size increased to 2.9 nm due to the condensation of the pore wall during the calcination process.

In Scheme 2.1 another synthetic approach to pure mesoporous titania is presented: (1) the reaction of Ti(O^{i}Pr)$_4$ and 1-dodecylamine produces as-made material; (2) the post-synthetic treatment with phosphoric acid/polyphosphoric acid partially removes the surfactant and stabilizes the mesoporous framework; (3) "ion-exchange" in an aqueous NaOH solution removes the phosphate species and introduces sodium to the material; (4) treatment with aqueous HCl solution; (5) washing with water removes Na$^+$, Cl$^-$ and partial surfactant; (6) calcination at 350 °C completely removes the retained surfactant and produces a pure mesoporous titania.

A similar process was carried out to prepare a new polymorph of titanium oxide, TiO$_2$(B), by Tornaux and coworkers.[22] The material was prepared from the precursor phase K$_2$Ti$_4$O$_9$ which was first synthesized by normal solid state reaction of KNO$_3$ (source of K$_2$O) and TiO$_2$ at 1000 °C for two days. This was then hydrolysed with nitric acid at room temperature to yield a solid product of stoichiometry H$_2$Ti$_4$O$_9$·H$_2$O. The final stage was to heat the material at 500 °C where it lost water to give the TiO$_2$(B) polymorph. The crystal structure of Ti$_2$O(B) is closely related to that of K$_2$Ti$_4$O$_9$: hydrolysis and dehydration led to
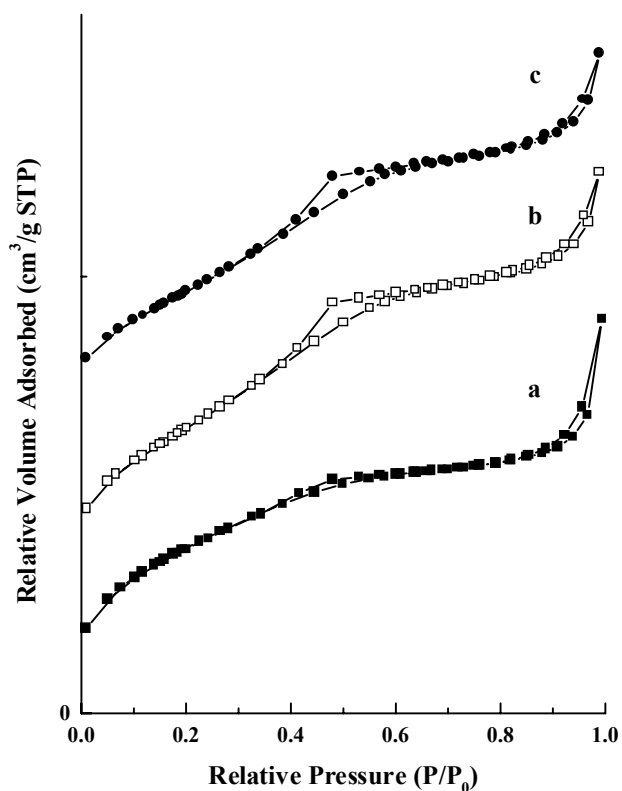
Figure 2.12 N_2-adsorption-desorption isotherms of (a) "Na_2O" doped mesoporous titania, (b) "Na_2O"-free mesoporous titania, (c) calcined pure mesoporous titania.
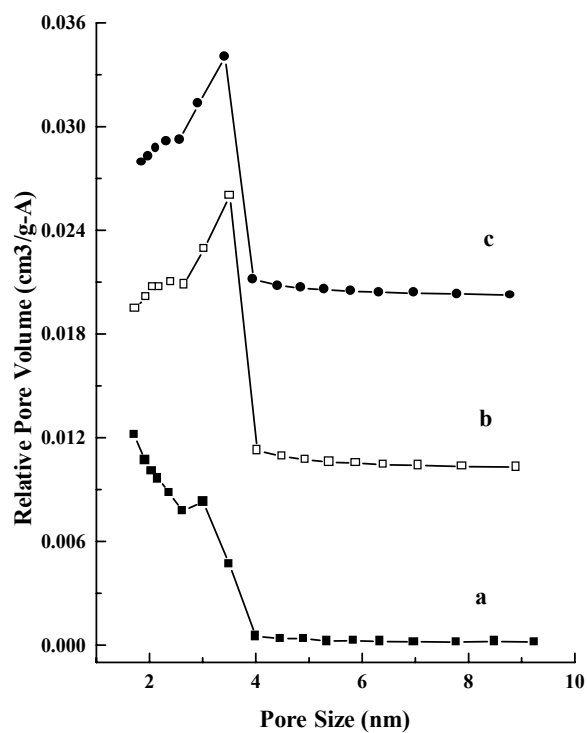

Figure 2.13 Pore size distributions of (a) "Na_2O" doped mesoporous titania, (b) "Na_2O"-free mesoporous titania, (c) calcined pure mesoporous titania.

$$Ti(O^iPr)_4 + H_2N(CH_2)_{11}CH_3 \xrightarrow{\quad - HO^iP_r \quad} Ti(OiPr)_3[NH(CH_2)_{11}CH_3]$$

↓ **hydrolysis**

as-synthesized mesoporous titania

↓ **phosphoric or polyphosphoric acid**

mesoporous titanium oxo phosphate ←—— **calcination** —— **phosphoric or polyphosphoric acid treated sample**

↓ **NaOH**

"Na$_2$O" doped mesoporous titania ←—— **calcination** —— **NaOH-treated sample**

↓ **HCl**

↓ **calcination**

pure mesoporous titania
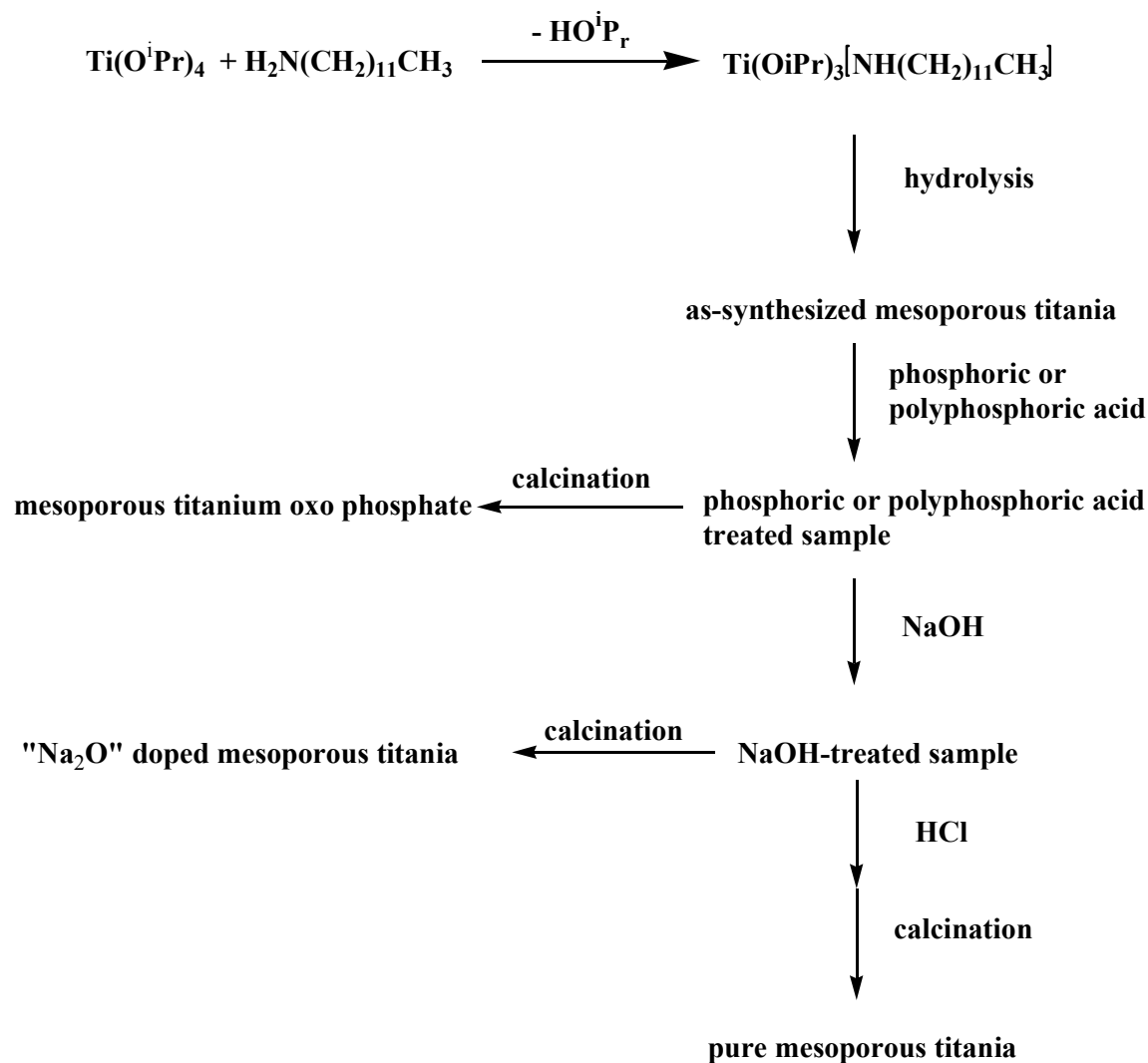
Scheme 2.1 Synthesis approach to mesoporous titanium oxides.

the effective removal of K$_2$O from K$_2$Ti$_4$O$_9$, leaving the remainder of the structure intact. The structure of TiO$_2$(B) is built of TiO$_6$ octahedra, but these are linked up in a different way to the structures of the other TiO$_2$ polymorphs, rutile, anatase and brookite.

Scheme 2.2 depicts a proposed process of "sodium ion exchange" on the surface of the pore wall. The stabilization effect of phosphate group has been discussed above. Displacement of phosphate by hydroxide does not damage the mesoporous structure. Moreover, the generated oxygen bridge is presumed beneficial to prevent the pore structure from collapsing.
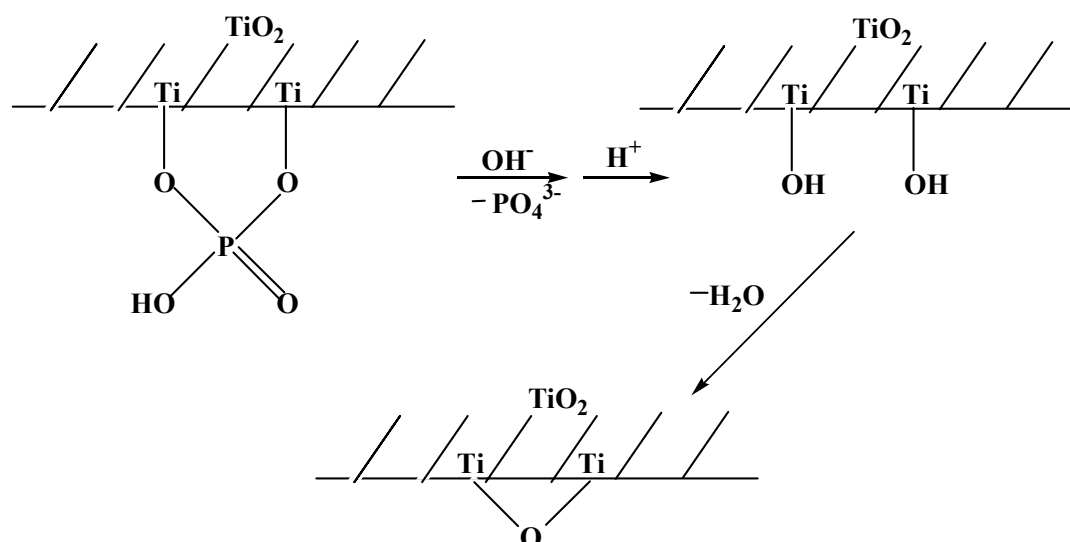
Scheme 2.2 "Sodium ion exchange" process in which the phosphate is removed by aqueous NaOH solution.

The purity of the material was confirmed by elemental analysis, revealing C 0.15%, H 0.66%, N 0.00%, Cl <0.1%, Na 0.1% and P 0.02%. No C-H stretches are observed in the IR spectrum. TGA shows no weight loss above 200 °C (Fig. 2.14d).

The obtained pure mesoporous titania shows a single reflection at d = 5.7 nm in the XRD pattern (Fig. 2.15d), which is the most intense and the sharpest amongst the XRD patterns presented in Fig. 2.15. N_2-adsorption-desorption measurements yield a typical type IV isotherm from which a BET surface area of 461 m^2g^{-1}, pore volume of 0.459 cm^3g^{-1} and a narrow distributed pore size of 3.4 nm are calculated (Fig. 2.16). The sharp decline in the desorption curve reveals the mesoporosity of the material, while the hysteresis between these two curves indicates a diffusion bottleneck, probably due to pore damage during the surfactant removal processes.

The thermal stability of the pure mesoporous titania has been examined by DSC (Fig. 2.6). An exothermal peak at 490 °C (Fig. 2.6a) suggests the pore structure collapses over this temperature.
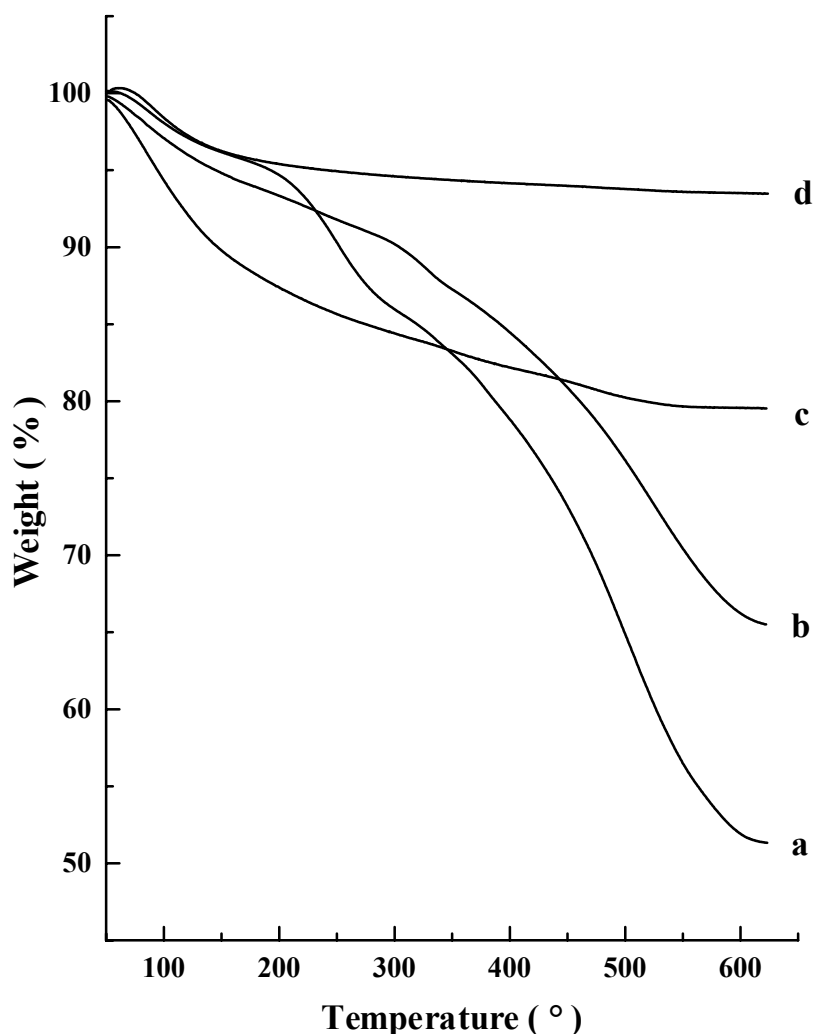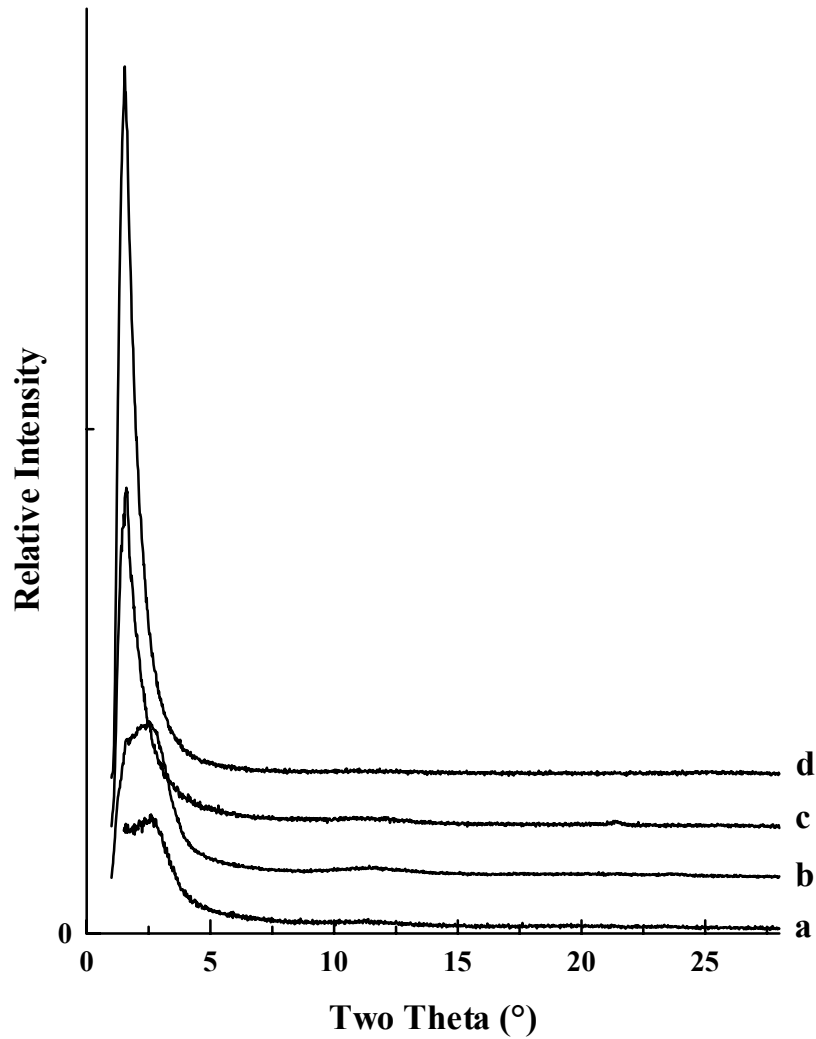
Figure 2.14 TGA plots of (a) as-synthesized mesoporous titania containing 1-dodecylamine, (b) phosphoric acid treated sample, (c) phosphate-free mesoporous titanium oxide, (d) calcined pure mesoporous titanium oxide.

When using polyphosphoric acid instead of phosphoric acid, the pure mesoporous titania obtained before calcination has a higher BET surface area but lower thermal stability of 430 °C. This is probably due to the larger pore (increased from 3.37 to 3.59 nm) and the thinner pore wall (decreased from 3.16 to 2.86 nm) (Table 2.2).

Comparing the characteristic properties of the pure mesoporous titania obtained by the two different routes described above, we found that the materials exhibit the same thermal stability, but the material obtained by the route shown in Scheme 2.1 has a much higher BET

Figure 2.15 X-ray diffraction patterns of (a) as-synthesized mesoporous titania containing 1-dodecylamine, (b) phosphoric acid treated sample, (c) phosphate-free mesoporous titanium oxide, (d) calcined pure mesoporous titanium oxide.

surface area, larger pore volume and bigger pore diameter. The reason might be due to the stabilization effect of the phosphoric acid post-synthetic treatment to the mesoporous structure.
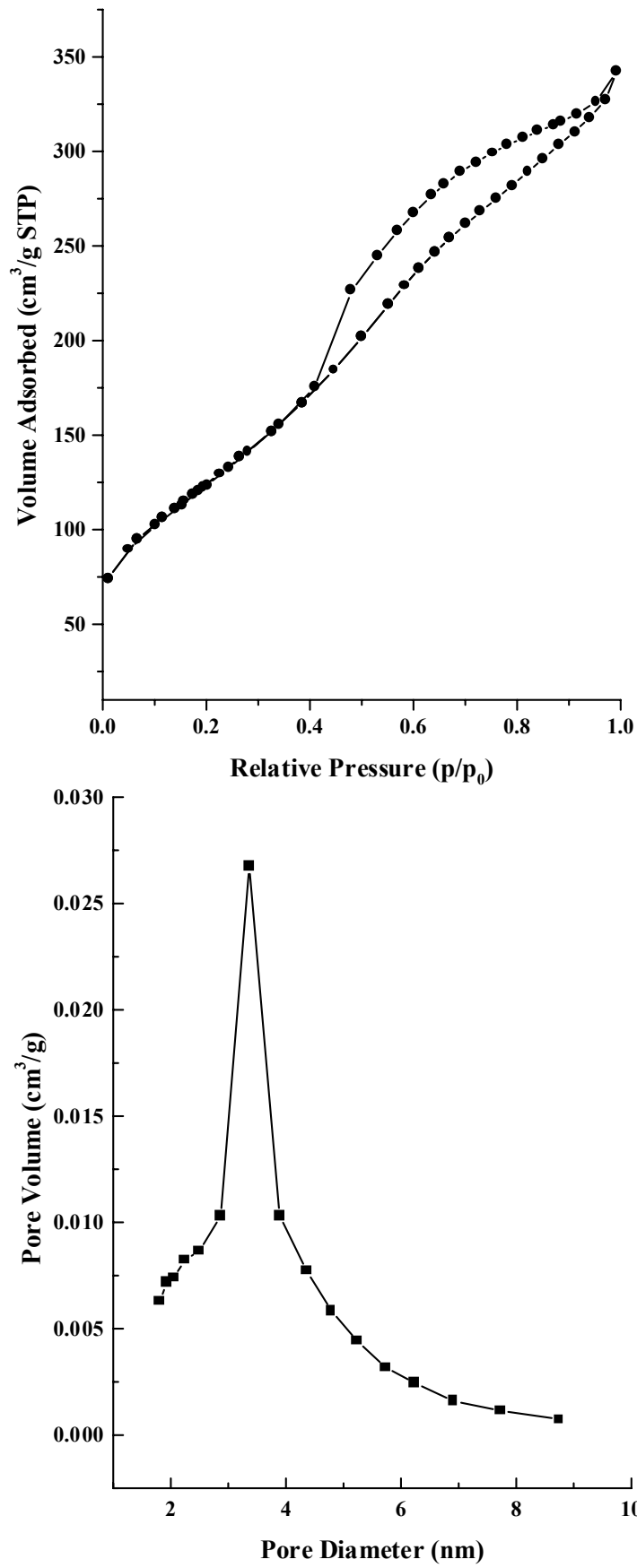
Figure 2.16 N₂-adsorption-desorption isotherm and pore size distribution of calcined pure mesoporous titanium oxide.

In conclusion, the mesoporous titanium oxide molecular sieves, namely titanium oxo-phosphate, "Na_2O" doped titania and pure titania, were synthesized by a ligand-assisted templating method. The strong covalent bonding between the metal center and the template head group is assumed responsible for the high quality of the mesoporous materials. The stabilization effect of the post-synthetic treatment with polyphosphoric acid has been demonstrated for the first time, to the best of our knowledge. The mesoporous titanium oxo-phosphate showed BET surface area high up to 503 m^2g^{-1} and thermal stability up to 626 °C. The "Na_2O" doped mesoporous titania showed BET surface area above 300 m^2g^{-1} and thermal stability above 530 °C. The pure mesoporous titania showed BET surface area of 461 m^2g^{-1} and thermal stability of 490 °C. In general, the mesoporous titanium oxides reported in this thesis exhibit remarkably higher thermal stability than the reported analogous in the literature. Their high surface area, unique pore size distribution and high thermal stabilitiy are certainly the most important features with respect to the majority of possible catalytic applications.

References

1. F. Schüth, *Ber. Bunsengers. Phys. Chem.* **1995**, *99*, 1306.

2. U. Giesla, F. Schüth, *Micro. and Meso. Mater.* **1999**, *27*, 131.

3. J. Ying, C. P. Mehnert, M. S. Wong, *Angew. Chem. Int. Ed.* **1999**, *38*, 56.

4. C. T. Kresge, M. E. Leonowicz, W. J. Roth, J. C. Vartuli, J. S. Beck, *Nature* **1992**, *359*, 710.

5. J. S. Beck, J. C. Vartuli, W. J. Roth, M. E. Leonowicz, C. T. Kresge, K. D. Schmitt, C. T.-W. Chu, D. H. Olson, E. W. Shepard, S. B. Mccullen, J. B. Higgins, J. L. Schlenker, *J. Am. Chem. Soc.* **1992**, *14*, 10834.

6. Q. Huo, D. I. Margolese, U. Cielsa, P. Feng, T. E. Gier, P. Sieger, R. Leon, P. M. Petroff, F. Schüth, G. Stucky, *Nature* **1994**, *368*, 317.

7. U. Ciesla, D. Demuth, R. Petroff, G. Stucky, K. Unger, F. Schüth, *J. Chem. Soc. Chem. Commun*. **1994**, 1387.

8. U. Ciesla, S. Schacht, G. D. Stucky, K. Unger, F. Schüth, *Angew, Chem. Int. Ed. Engl*. **1996**, *35*, 541.

9. M. Thieme, F. Schüth, *Micro. and Meso. Mater*. **1999**, *27*, 193.

10. D. M. Antonelli, J. Y. Ying, *Angew. Chem. Int. Ed. Engl*. **1995**, *34*, 2014.

11. D. M. Antonelli, J. Y. Ying, *Angew. Chem. Int. Ed. Engl*. **1996**, *35*, 426.

12. D. M. Antonelli, A. Nakahira, J. Y. Ying, *Inorg. Chem*. **1996**, *35*, 3126.

13. D. M. Antonelli, J. Y. Ying, *Chem. Mater*. **1996**, *8*, 874.

14. M. S. Wong, D. M. Antonelli, J. Y. Ying, *Nanostruc. Mater.* **1997**, *9*, 165.

15. D. M. Antonelli, *Micro. and Meso. Mater*. **1999**, *30*, 315.

16. J. S. Reddy, A. Sayari, *Catal. Lett*. **1996**, *38*, 219.

17. P. Liu, J. Liu, A. J. Sayari, *Chem. Commun*. **1997**, 577.

18. Z. R. Tian, J. Y. Wang, N. G. Duan, V. V. Krishnan, S. L. Suib, *Science* **1997**, *276*, 926.

19. A.orma, M. T. Navarro, J. Pérez-Pariente, *J. Chem. Soc., Chem. Commun*. **1994**, 147.

20. P. T. Tanev, M. Chibwe, T.J. Pinnavaia, *Nature* **1994**, *368*, 321.

21. R. L. Putnam, N. Nakagawa, K. M. McGrath, N. Yao, I. A. Aksay, S. M. Gruner, A. Navrotsky, *Chem. Mater*. **1997**, *9*, 2690.

22. A. R. West, *Solid State Chemistry and Its Applications*, John Wiley & Sons, **1992**, pp 31.

Chapter 3. Synthesis and Characterization of Mesoporous Zirconium Oxide

3.1. Introduction

Since the first examples of stable transition metal oxide mesoporous molecular sieves appeared in 1996,[1,2] there have been many attempts to synthesize mesoporous transition metal oxides. Zirconium oxide is of particular interest in the application of acid catalysis.[3] Zirconium oxide contains both weakly acidic and basic surface sites, providing for high activity in reactions requiring acid-base bifunctional catalysts.[4,5] Porous zirconia with BET surface areas of 100-200 m^2g^{-1} can be prepared by chemical methods and supercritical drying of zirconia gels.[6] However, an inherent drawback of these materials is the facile sinterability and concomitant loss of surface area at temperatures higher than 400 °C. The major thermodynamic driving force is the crystalline transformation of these zirconia materials into dense, low-surface-area monoclinic and metastable tetragonal phases.[7] By introducing dopants, such as phosphates[8] and sulfates,[9] the low thermal stability of pure zirconia can be improved.

Some synthetic approaches to mesoporous zirconium oxides have been based upon the concepts of electronic,[10,11] hydrogen-bonding,[12,13] and covalent-bond interactions,[1,2,14] but they have resulted in a lamellar phase in most cases. Removal of the surfactant without collapse of the zirconium oxide framework is very difficult; the few exceptions include microporous zirconium oxophosphate,[15,16] zirconium oxide[15] and mesoporous phosphated zirconia.[17]

We have successfully achieved the syntheses of thermally stable titanium oxide, titanium oxo-phosphate and "Na$_2$O" doped titanium oxide in mesoporous forms, as reported

in Chapter 2. Therefore, we decided to extend the ligand-assisted templating methodology, as presented in Scheme 2.1, to the synthesis of mesoporous zirconium oxides.

3.2. Results and Discussion

3.2.1. Synthesis and Characterization of As-synthesized Mesoporous Zirconia

Mesoporous titanias were successfully synthesized by a ligand-assisted templating method in which titanium isopropoxide was used as metal center and 1-dodecylamine as surfactant. The strong covalent bonding between titanium and the amine template resulted in highly thermal stable mesoporous materials. Thus, we adopted similar methods to synthesize mesoporous zirconium oxides. Zirconium ethoxide was used as the metal center and 1-dodecylamine as surfactant. Although mixing the two precursors did not bring about any significant reactions, as monitored by ^{1}H NMR, distilling off the by-product EtOH at 50 °C under reduced pressure led to the formation of complex $Zr(OCH_2CH_3)_3[HN(CH_2)_{11}CH_3]$ (Equation 3.1) as an analytically pure product. The strong covalent bonding between zirconium and the amine template is proposed to be an important factor to produce stable mesoporous materials as in the cases of mesoporous titanium oxides described in Chapter 2.

$$\textbf{Zr(OEt)}_4 + \sim\!\!\sim\!\!\sim\!\!\sim\!\!\text{NH}_2 \xrightarrow{\text{- EtOH}} \quad (3.1)$$
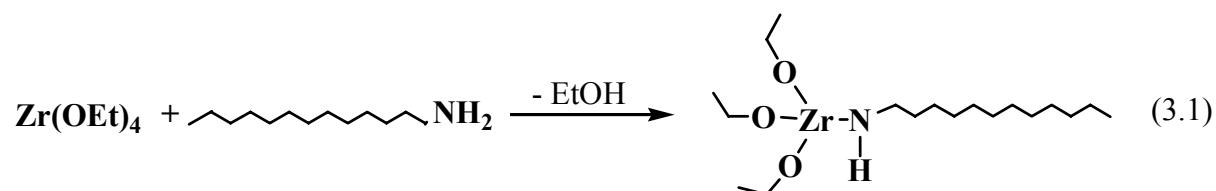
The hydrolysis of complex $Zr(OCH_2CH_3)_3[HN(CH_2)_{11}CH_3]$ was carried out in an EtOH-H$_2$O co-solvent, in a manner analogous to the hydrolysis of $Ti(OC_3H_7)_3[HN(CH_2)_{11}CH_3]$ and $Ti(OC_3H_7)_3[O(CH_2)_{11}CH_3]$ with an ^{i}PrOH-H$_2$O co-solvent.

The co-solvent functioned to restrain the hydrolysis rate. After aging at room temperature for 1 day and 70 °C for 5 days, the as-synthesized mesoporous zirconia was produced, which was characterized by TGA, XRD and N_2-adsoption-desorption method.

The TGA plot of the as-synthesized mesoporous zirconia is shown in Fig. 3.1a. A 15% weight loss below 120 °C is corresponding to physisorbed water, and a 15-18% weight loss between 120 and 600 °C is from both the decomposition of the organic surfactant and the removal of structural water. This indicates that ca. 70% of surfactants have been washed away while forming the as-synthesized mesoporous material. This behavior is in contrast to the as-synthesized mesoporous titania where only ca 30% of surfactants have been washed away while forming the as-synthesized material.

The X-ray diffraction pattern of the as-synthesized mesoporous zirconia (Fig. 3.2a) shows only one reflection at d-spacing of 5.4 nm. This reflection can be indexed as (100) assuming a hexagonal unit cell. The low intensity reflections of (110), (200) and (210), which showed up in the XRD patterns of the as-synthesized surfactant composites, e.g. $ZrO_x(SO_4)_{2-x}$,[18] are not observed in our examples. However, the feature of a single (100) peak in the XRD pattern does not exclude the materials having mesoporous structures. Materials with only one distinct XRD reflection have been found to contain a substantial amount of MCM-41 structure.[18] The XRD of an as-made sample prepared from $Ti(OMe)_4$ and a C_{12}-surfactant Dodecanol +5 EO also showed a single diffraction peak.[19] This phenomenon has been attributed to either disordered packing of individual tubes in mesostructures or a very small crystalline size.[20,21] In Chapter 2 we reported mesoporous titania and derivatives, where the single XRD reflection indicates the existence of mesoporous structure which is not highly ordered. Nevertheless, N_2-adsorption-desorption measurements (see below) show that the as-synthesized mesoporous zirconia has mesoporous structure.
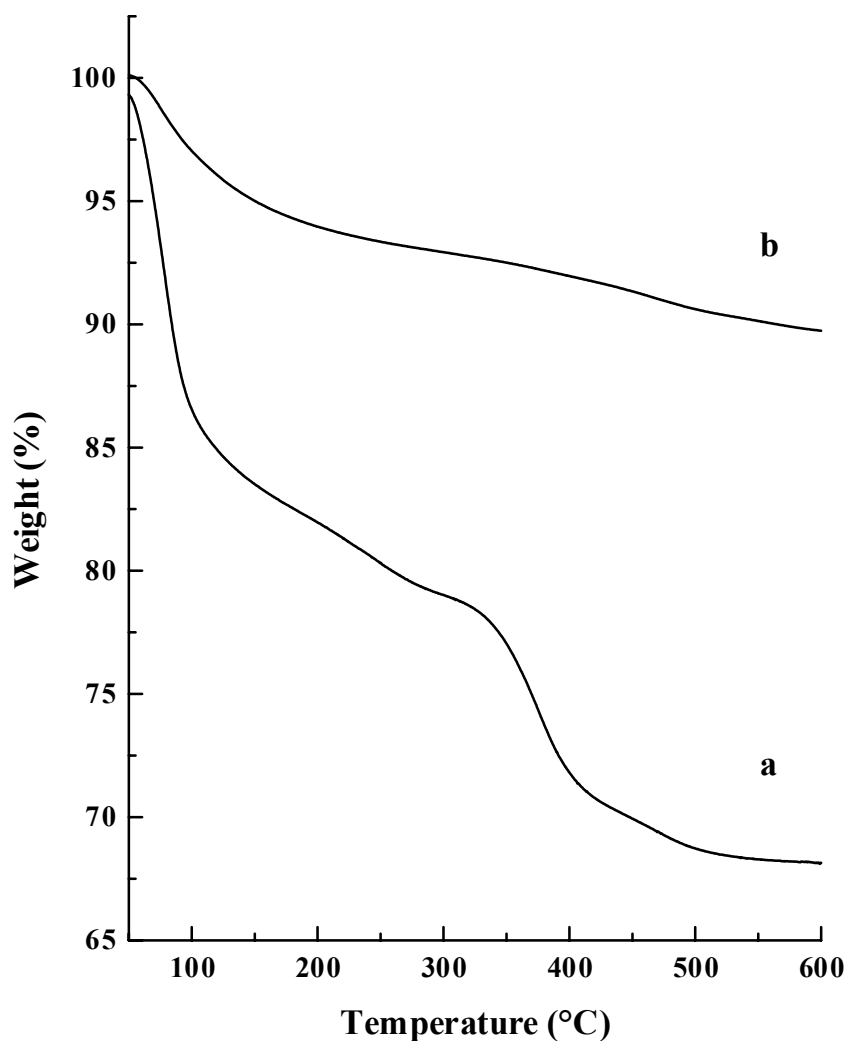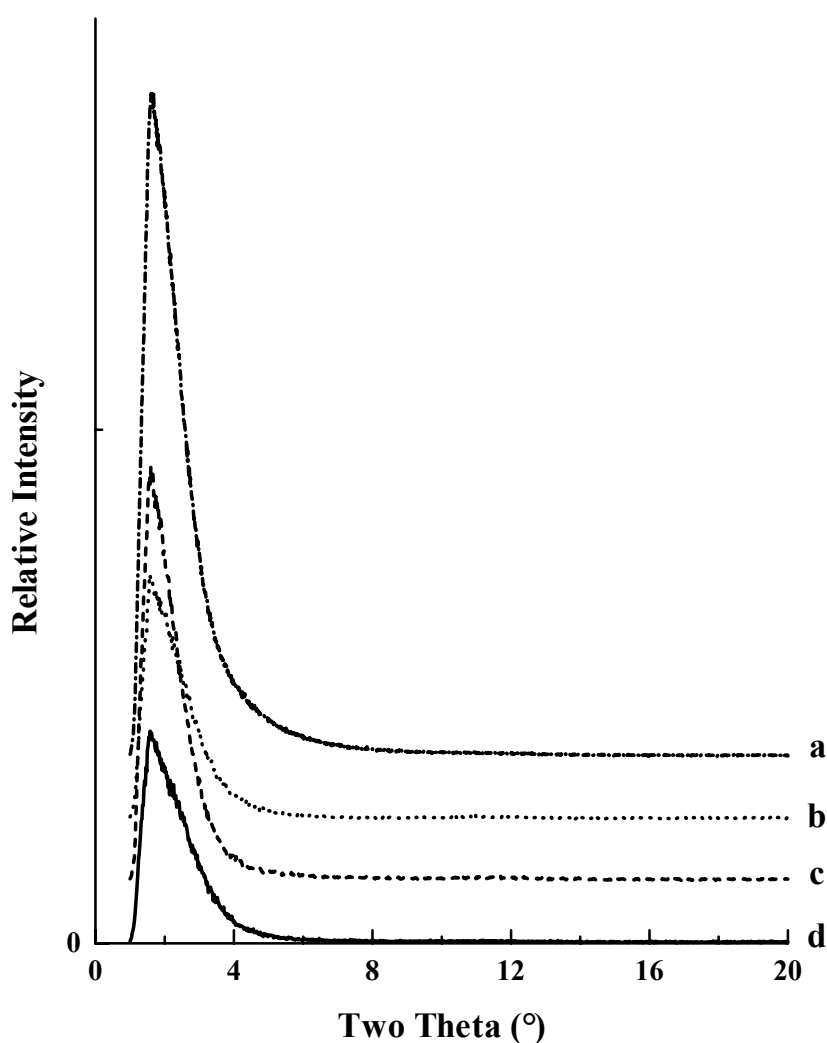
Figure 3.1 TGA plots of (a) the as-synthesized mesopoous zirconia synthesized at 50 °C and aged at 75 °C for 5 days, (b) the pure mesoporous zirconia obtained after treated with H_3PO_4, NaOH, HCl and calcined at 350 °C.

A comparison of the XRD between the as-synthesized zirconia and the as-synthesized titania (Fig 2.1a) reveals that, the reflection intensity of the former is much higher than that of the latter. The main reason is probably due to the presence of less surfactant in the as-made zirconia than in the as-made titania (see above). Recent studies have demonstrated that the removal of the occluded organic template from mesostructures enhances the Bragg scattering cross-section,[18] so as to cause the XRD reflection becoming sharper and more

intense. This phenomenon has also been observed when comparing the XRD between the template-free mesoporous titanium oxides and the as-made materials in Chapter 2, and between the template-free mesoporous alumina and the as-made material in Chapter 4.

The N_2-adsorption-desorption isotherm and the pore size distribution of the as-synthesized mesoporous zirconia is presented in Fig. 3.3a. The isotherm plot belongs to type

Figure 3.2 XRD patterns of (a) the as-synthesized mesoporous zirconia, (b) the mesoporous zirconium oxo-phosphate, (c) the pure mesoporous zirconia obtained by direct calcination at 400 °C, and (d) the pure mesoporous zirconia upon treatment with H_3PO_4, NaOH, HCl and calcination at 350 °C.
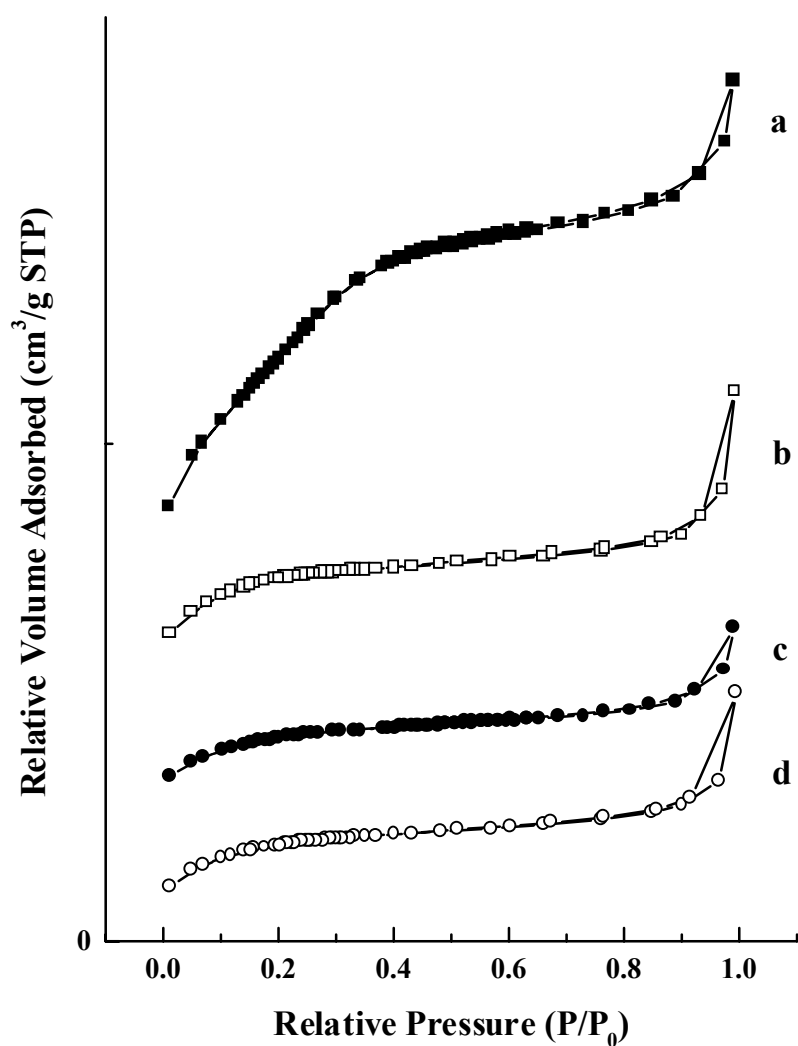
Figure 3.3 N$_2$-adsorption-desorption isotherms and pore size distributions of (a) the as-synthesized mesoporous zirconia, (b) the mesoporous zirconium oxo-phosphate, (c) the pure mesoporous zirconia obtained by direct calcination at 400 °C, and (d) the pure mesoporous zirconia upon treatment with H$_3$PO$_4$, NaOH, HCl and calcination at 350 °C.

IV, but hysteresis loop is absent. Although mesoporous materials have been studied for one decade, there is still no satisfactory explanation for those cases where the hysteresis loops absent.[19] The BET surface area of the as-synthesized material is 711 m^{2}g^{-1}. The average pore diameter of ca. 2.4 nm is obtained from the pore size distribution based on the BJH desorption branch. The wall thickness is calculated to be ca 3.8 nm. The feature of small

pores with thick walls has also been reported by Schüth *et.al.* in the examples of porous zirconium oxo-phosphates.[15]

3.2.2. Synthesis and Characterization of Porous Zirconium Oxo-Phosphate

In order to prevent pore structures from collapsing at high calcination temperatures, the as-synthesized material was treated with aqueous phosphoric acid solution. The stabilization effect of phosphoric acid post-synthetic treatment has been demonstrated by Ciesla *et al.* in mesoporous zirconium oxide, and Thieme *et al.* in mesoporous titanium oxo-phosphate.[15,19-21] In Chapter 2 we also found that treatment with phosphoric acid or polyphosphoric acid stabilized mesoporous titanium oxide framework. Therefore, post-synthetic treatment with phosphoric acid is used here in order to prepare thermally stable mesoporous zirconium oxide derivatives.

The as-synthesized surfactant composite was treated with phosphoric acid (pH = 0.5) for 3 h, washed with water and ethanol, and dried at 120 °C for 2 h. After calcination at 400 °C, the retained surfactant was completely removed as confirmed by elemental analysis and IR spectroscopy. Both the analysed C and N percentages are below 0.1%, and 0.89% of H found comes from the absorbed water. No C-H stretching bands are observed in the region of 2800 to 3000 cm^{-1} in the IR spectrum, confirming that the material is organic surfactant-free. The characteristic peak around 1030 cm^{-1} comes from P=O stretches of phosphate, indicating that the material is a zirconium oxo-phosphate.

Fig. 3.2b shows the XRD of the calcined porous zirconium oxo-phosphate. Compared to the data of the as-synthesized material, the intensity decreases and the d-spacing shifts from 5.4 to 5.6 nm. The reason is due to the pore structure partially collapsing and the pore wall condensing upon calcination. This phenomenon has been observed by Ciesla *et al.*[19] in

the preparation of porous zirconium oxo-phosphate: due to incomplete condensation of the walls, the ordered pore structure collapses upon thermal treatment of the samples in air at 773 K, leading to the loss of intensity or disappearance of the low angle XRD reflections. The loss of intensity and the shifting towards lower 2θ angles of the (100) reflection after calcination of a mesoporous zirconium anionic surfactant composite, has also been reported by Pacheco *et al.*[22]

The N_2-adsorption-desorption isotherm of the porous zirconium oxo-phosphate is presented in Fig. 3.3b. No hysteresis loop is observed and the step of the isotherm is around a relative pressure of 0.2. The step above 0.8 of P/P_0 in isotherm plot indicates the existence of inter particle pores. N_2-adsorption isotherms of this type are typical for pores with pore sizes between micro- and meso-pores.[18] The BET surface area is 336 m^2g^{-1}. The average pore diameter of ca. 2.2 nm is obtained from the pore size distribution based on the BJH desorption branch.

3.2.3. Synthesis and Characterization of Pure Porous Zirconium Oxide

A high thermal stability of the mesoporous zirconia is reasonably expected since the as-synthesized mesoporous zirconium oxide has thick pore walls as described in section 3.2.1. An attempt to remove surfactant, therefore, was carried out by calcination of the as-synthesized material at 400 °C. The elemental analysis confirmed that a pure zirconia was obtained upon calcination.

Fig. 3.2c shows the XRD pattern of the calcined pure porous zirconia. In comparison to the pattern of the as-synthesized material, the intensity decreases and d-spacing slightly shifts from 5.4 to 5.5 nm. The same phenomenon has been observed in the mesoporous zirconium oxo-phosphate (section 3.2.2). We assume that this is due to incomplete condensation of the

walls. The condensation led to the formation of tetragonal zirconia in the walls, as confirmed by its typical XRD reflection (Fig. 3.4a).
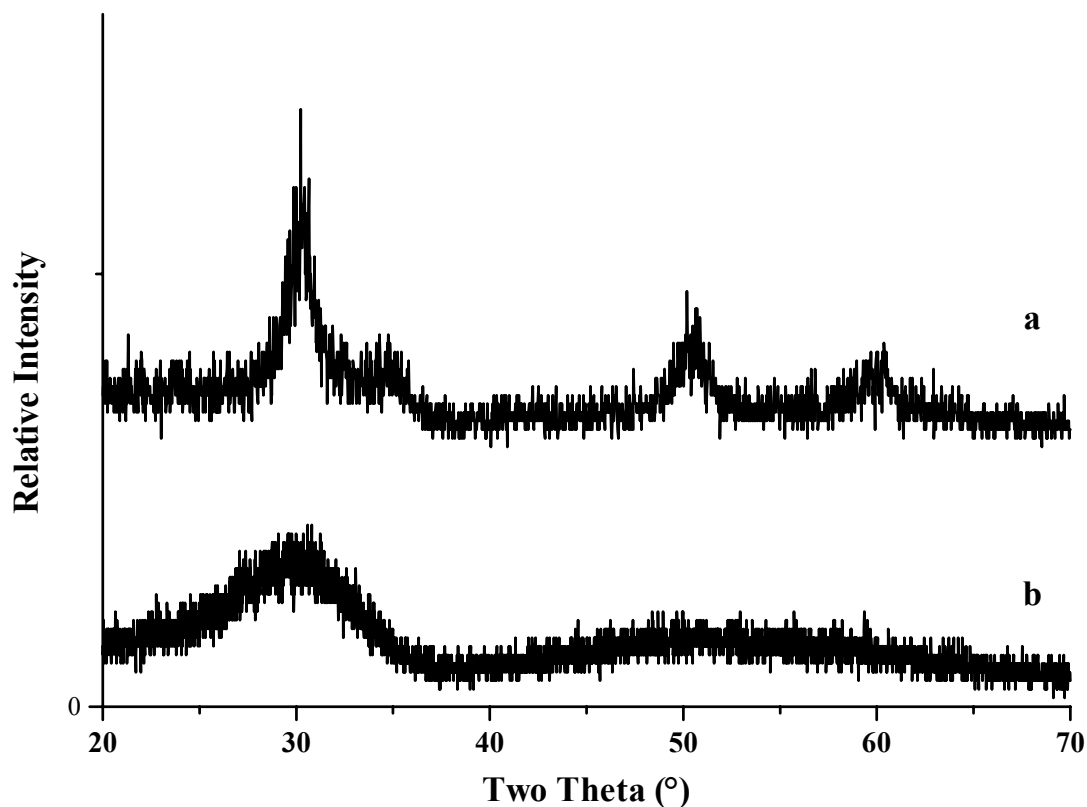
The N_2-adsorption-desorption isotherm and the pore size distribution of the pure porous zirconia are presented in Fig. 3.3c. No hysteresis loop is found and the step of the isotherm is around a relative pressure of 0.2. N_2 isotherms of this type are typical for pores with pore sizes between micro- and meso-pores.[18] The BET surface area is 228 m^2g^{-1}. The average pore diameter of ca. 2.2 nm is obtained from the pore size distribution based on the BJH desorption branch.

We have also attempted to obtain pure mesoporous zirconia by the strategy summarized in Scheme 2.1. The sample was subsequently treated with aqueous NaOH solution after the phosphoric acid post-synthetic treatment. No characteristic P=O stretches around 1030 cm^{-1} was identified in the IR spectrum, indicating that the phosphate group was removed from the material. Upon calcination at 400 °C, the material shows a BET surface area of only 136 m^2g^{-1}. The disappearance of the low angle XRD reflection suggested a collapse of the pore structure. Elemental analysis found only 1.4% of Na in the sample. The synthetic approach to the "Na_2O" doped mesoporous titania reported in Chapter 2 is obviously not applicable in the preparation of zirconium analogue.

However, if the sample is treated with diluted aqueous HCl before calcination and subsequently calcined at 350 °C, a pure porous zirconia is obtained. Elemental analysis data of C 0.82, H 1.16 and N 0.00% confirm the purity of the calcined sample. In the TGA plot (Fig. 3.1b) only ca. 5% of weight loss is found above 200 °C, corresponding to the removal of structural water.

The XRD pattern of the pure porous zirconia (Fig. 3.2d) shows a similar feature when compared to that of the as-synthesized material. The loss of intensity and shifting from 5.4 to 5.6 nm of the (100) d-spacing indicate an incomplete condensation of the walls.[19,22] Two

broad reflections were observed in the region of $2\theta = 20\text{-}70°$ (Fig. 3.4b). According to the literature,[22] these broad reflections with relatively high intensity indicate the existence of quasi-amorphous walls.

Figure 3.4 XRD patterns of the pure porous zirconia obtained by direct calcination at 400 °C (a) and by utilizing the approach to pure mesoporous titania as summarized in Scheme 2.1 (b).

The N_2-adsorption-desorption isotherm of the obtained pure porous zirconia is presented in Fig. 3.3d. The shape of isotherm is very similar to that of pure porous zirconia obtained by direct calcination (Fig. 3.3c). Lack of hysteresis loop and the step of the isotherm located at a low relative pressure of 0.2 are indicative of pores with pore sizes between micro- and mesopores.[18] The BET surface area is 242 m^2g^{-1}, slightly higher than that of the

sample prepared by direct calcination. The BJH average pore diameter of ca. 2.2 nm is also comparable to that of the directly calcined sample.

In summary, the ligand-assisted templating methodology, which is utilized in the synthesis of mesoporous titanium oxides (Chapter 2), is also applied to the synthesis of porous zirconium oxo-phosphate and pure zirconium oxide, although the pore sizes are between micro- and meso-pores. However, zirconium analogue of "Na$_2$O" doped mesoporous titania is not successfully obtained.

References

1. D. M. Antonelli, J. Y. Ying, *Angew. Chem. Int. Ed. Engl*. **1996**, *35*, 426.

2. D. M. Antonelli, A. Nakahira, J. Y. Ying, *Inorg. Chem*. **1996**, *35*, 3126.

3. T. Yamaguchi, *Catal. Today* **1994**, *20*, 199.

4. Y. Nakano, T. Lizuka, H. Hattori, K. Tanabe*, J. Catal*. **1979**, *57*, 1.

5. K. Tanabe, T. Yamaguchi, *Catal. Today* **1994**, *20*, 185.

6. D. A. Ward, I. E. Ko, *Chem. Mater*. **1993**, *5*, 956.

7. C. E. Subbarao, *Science and Technology of Zirconia*, American Ceramic Society: Columbus, OH, **1981**; p1.

8. R. Boyse, I. E. Ko, *Catal Lett*. **1996**, *38*, 225.

9. X. Song, A. Sayari, *Catal. Rev.-Sci. Eng*. **1996**, *38*, 329.

10. Q. Huo, D. I. Margolese, U. Ciesla, D. G. Demuth, P. Feng, T. E. Gier, P. Sieger, A. Firouzi, B. F. Chmelka, F. Schüth, G. D. Stuck, *Chem. Mater*. **1994**, *6*, 1176.

11. Q. Huo, D. I. Margolese, U. Ciesla, P. Feng, T. E. Gier, P. Sieger, R. Leon, P. M. Petroff, F. Schüth , G. D. Stucky, *Nature* **1994**, *368*, 317.

12. P. T. Tanev, T. J. Pinnavaia, *Science* **1995**, *267*, 865.

13. S. A. Bagshaw, E. Prouzert, T. J. Pinnavaia, *Science* **1995**, *269*, 1242.

14. D. M. Antonelli, J. Y. Ying, *Chem. Mater*. **1996**, *8*, 874.

15. U. Ciesla, S. Schacht, G. D. Stucky, K. K. Unger, F. Schüth, *Angew. Chem. Int. Ed. Engl.* **1996**, *35*, 541.

16. P. Liu, J. S. Reddy, A. Adnot, A. Sayari, *Mater. Res. Soc. Symp. Proc*. **1996**, *431*, 101.

17. M. S. Wong, D. M. Antonelli, J. Y. Ying, *Nanostr. Mater*. **1997**, *9*, 165.

18. D. M. Antonelli, *Micro. Meso. Mater*. **1999**, *30*, 315.

19. U. Ciesla, F. Schüth, *Micro. Meso. Mater*. **1999**, *27*, 131.

20. M. Thieme, F. Schüth, *Micro. Meso. Mater*. **1999**, *27*, 193.

21. U. Ciesla, D. Demuth, R. Petroff, G. Stucky, K. Unger, F. Schüth, *J. Chem. Soc., Chem. Commun*. **1994**, 1387.

22. G. Pacheco, E. Zhao, A. Garcia, A. Sklyarov, J. J. Fripiat, *J. Mater. Chem.* **1998**, *8*, 219.

Chapter 4. Synthesis and Characterization of Bimodal Mesoporous Alumina

4.1. Introduction

Although activated aluminas are attractive catalysts for many chemical processes, their wide spread application is limited. They possess only textural porosity and lack the selective framework/confined pore structure characteristic of a molecular sieve. Therefore, the synthesis of mesoporous aluminas would be of industrial interest.

Since the original synthesis of MCM-41 mesoporous molecular sieves have been achieved by electrostatic interactions between a positively charged surfactant and a negatively charged inorganic precursor to assemble the mesostructure,[1,2] there have been some attempts to prepare mesoporous aluminas by electrostatic assembly pathways,[3-5] but all afforded products collapsed upon surfactant removal. The first example of mesoporous alumina molecular sieves was obtained by the neutral surfactant (copolymer based on polyethylene oxide and polypropylene oxide) templating method.[6] Since then, mesoporous aluminas have also been successfully synthesized by the use of anionic surfactants[7] and cationic surfactants.[8]

In this chapter we present self-assembling processes leading to the formation of unusual bimodal mesoporous aluminas. Neutral surfactant templating method was employed, in which aluminum isopropoxide was used as a metal center and neutral alkylamines as surfactants. The synthetic factors, *e.g.* reaction, aging and calcination temperatures, surfactant length, etc, which influence the structures of mesoporous aluminas, have been studied in detail.

4.2. Results and Discussion

4.2.1. Synthesis and Characterization

As the preparation of mesoporous titanium oxides was successfully achieved by a neutral surfactant templating method, we endeavored to adapt this methodology to the synthesis of mesoporous alumina.

Aluminium isopropoxide is known to exist as a tetramer that is readily cleaved by donor molecules to form mononuclear adducts.[11] The reaction between aluminum isopropoxide and 1-dodecylamine led to the formation of an adduct $(^iPrO)_3Al[NH_2(CH_2)_{11}CH_3]$ (Equation 4.1) that was monitored by ^{1}H-NMR. There are two different types of CH proton signals found at $\delta = 4.21$ and 4.52 ppm in the precursor, indicating the existence of tetrameric aluminium isopropoxide. The bridging isopropoxide groups exhibit their CH proton signal at $\delta = 4.52$ ppm. However, only one distinguishable type of CH protons was presented at $\delta = 4.22$ ppm after formation of the adduct $(^iPrO)_3Al[NH_2(CH_2)_{11}CH_3]$. The disappearance of CH proton signal at $\delta = 4.52$ ppm indicates the formation of a monomeric adduct.
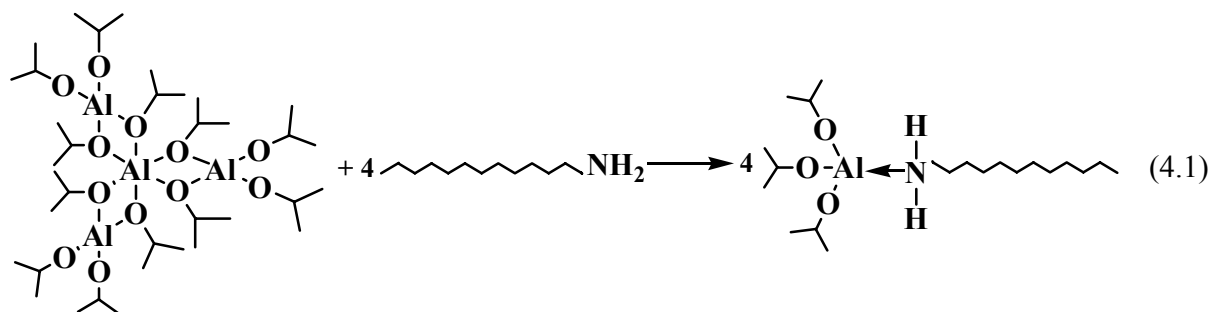
The expected coordination compound analogous to $(^iPrO)_3Ti[NH(CH_2)_{11}CH_3]$ was not obtained. Thus, a different methodology was developed to prepare mesoporous alumina. By

the following procedure, bimodal mesoporous alumina was obtained: (1) aluminium isoproxide was mixed with one equivalent of 1-dodecylamine at 80 °C to form an adduct $(^iPrO)_3Al[NH_2(CH_2)_{11}CH_3]$; (2) hydrolysis of the adduct in an isopropanol-water co-solvent at 30 °C led to the formation of an alumina gel; (3) aging at room temperature for 5 days; (4) as-synthesized mesoporous alumina was obtained after washing with water, ethanol and diethyl ether, and drying at 120 °C overnight; (5) pure bimodal mesoporous alumina was produced after calcination at 450 °C for 4 h in a stream of air.

As described in Chapter 2, the mesoporous materials can be synthsized not only by the electrostatic interactions between a charged surfactant and a charged inorganic precursor,[2,4] but also by the hydrogen bonding and covalent bonding interactions between neutral inorganic precursors and neutral surfactants.[9] In fact, the neutral surfactant templating method was effectively used by Pinnavaia and his co-workers for the synthesis of mesoporous alumina.[10]

Relative to electrostatic templating pathways, route of using neutral amine templates and neutral inorganic precursors offers the practical advantage of facile template removal by non-corrosive solvent extraction. In alumina case, only 7% surfactant retained after solvent extraction. The elemental analysis data of the as-synthesized material, C 5.44%, H 3.5% and N 0.31%, revealed that the material retained ca. 7% of surfactant. It correlates with the TGA, shown in Fig. 4.1. The as-synthesized material shows an 8-10% weight loss below 120 °C corresponding to physisorbed water and a 20-25% weight loss between 120 and 700 °C due to both decomposition of the surfactant and removal of structural water. Elemental analysis indicates that the organic residue totally decomposes after calcination at 450 °C for 4 h. The TGA of the calcined material only shows a 10-12% weight loss between 50 and 600 °C corresponding to the removal of physisorbed and structural water.
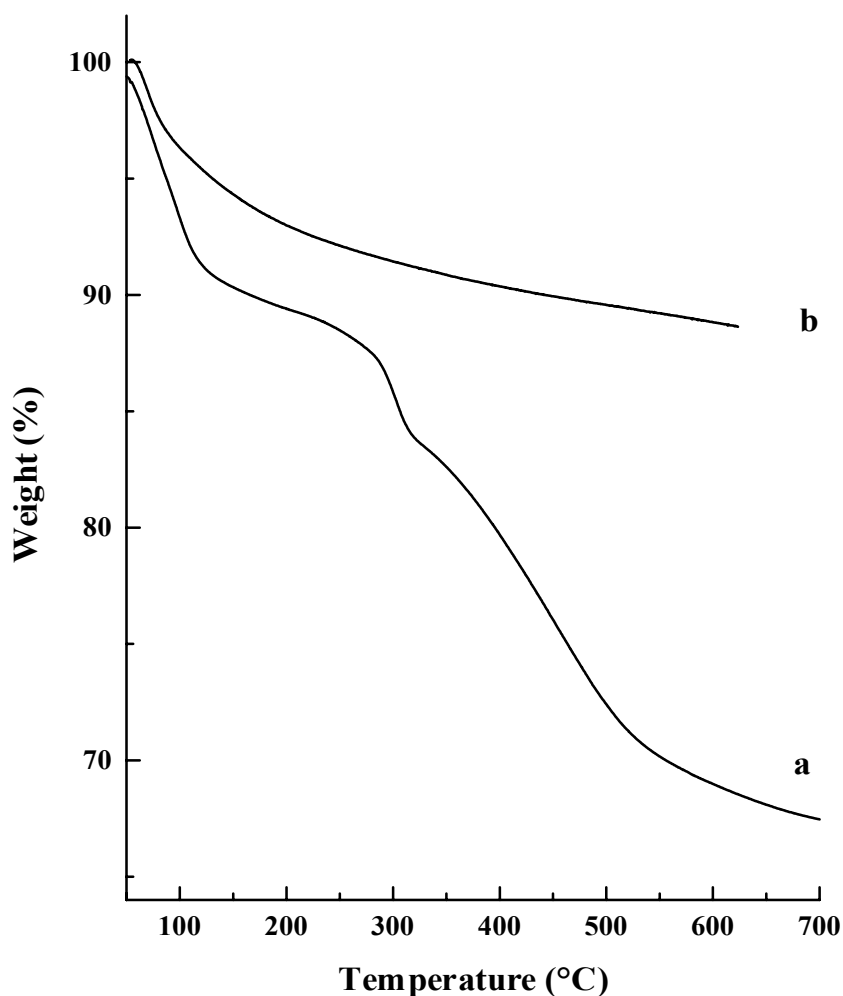
Figure 4.1 TGA plots: (a) the as-synthesized mesoporous alumina synthesized at 80 °C and aged at room temperature; (b) the bimodal mesoporous alumina calcined at 450 °C.

It is acknowledged that XRD single line at high d-spacing is typically observed from mesoporous materials featuring randomly ordered pores.[12] This line is much broader than that exhibited by hexagonal, cubic and lamellar phases where repeating units are homogeneous in size. Recent modeling studies have shown that the removal of the occluded organic template from hexagonal mesostructures enhances the Bragg scattering cross-section,[6] thereby the XRD peak becomes sharper and more intense. As described in Chapter 2 for mesoporous titanium oxides, the intensities of the XRD lines are substantially higher for the template-free forms than for the as-made materials. On the contrary, as shown in Fig. 4.2, both the as-synthesized
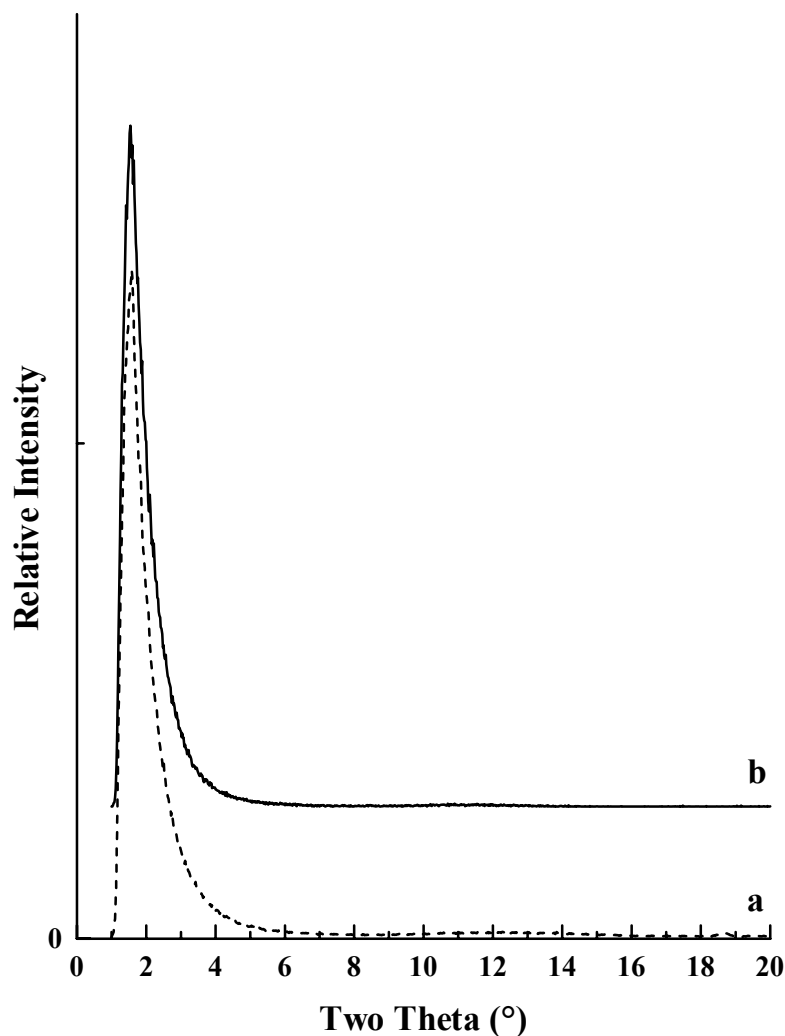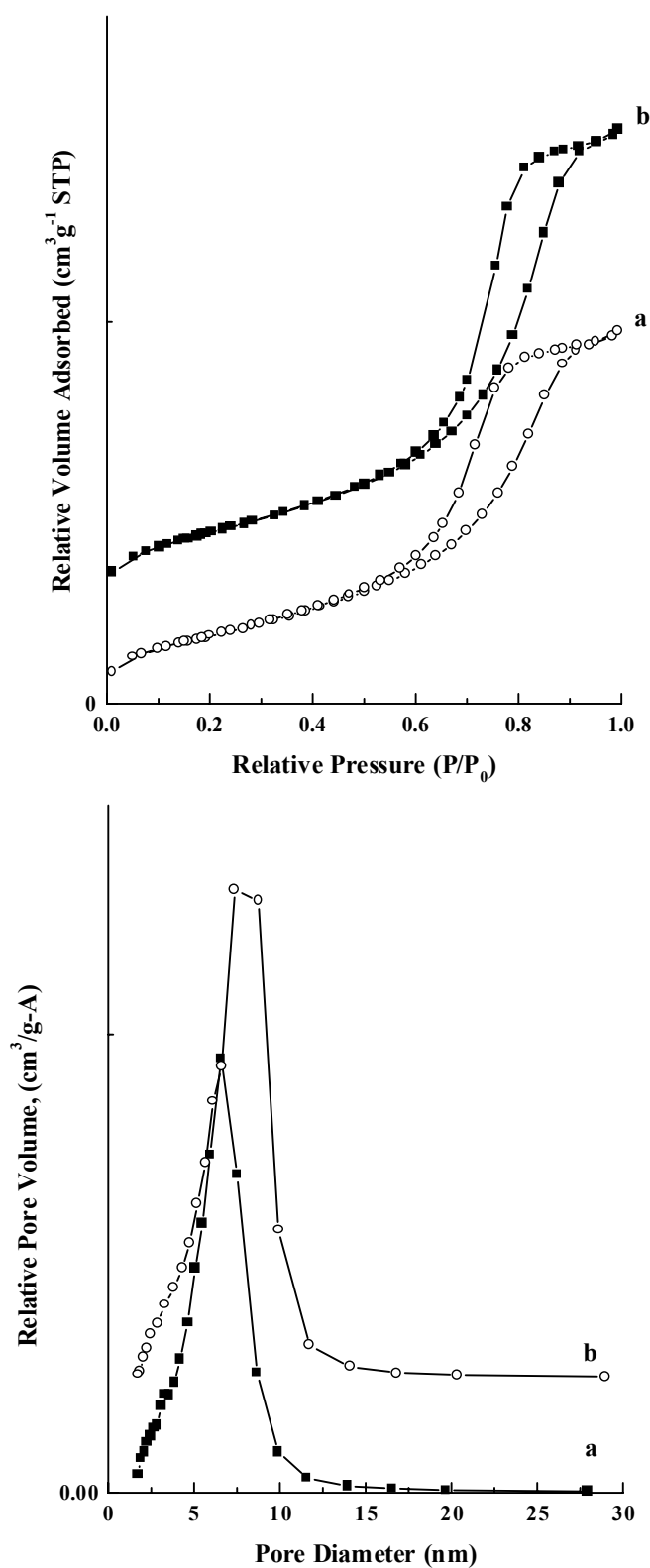
Figure 4.2 X-Ray powder diffraction (XRD) patterns: (a) the as-synthesized mesoporous alumina synthesized at 80 °C and aged at room temperature; (b) the bimodal mesoporous alumina calcined at 450 °C.

and calcined mesoporous aluminas show a single broad high-intensity reflection at high d-spacing. The XRD pattern of the as-made material does not show significant differences from the calcined material with regard to intensity and broadness, as the solvent extraction has washed out most of the surfactant so that the as-made material only contains ca. 7% of surfactant. Analogous single peak patterns corresponding to large d spacings have been observed for disordered MCM-41,[3,13] HMS,[9] MSU-X silicas,[10] and mesoporous titanium oxides (Chapter 2). However, the reflections of mesoporous alumina presented here are

broader, signifying an even greater degree of structural disorder. Similar features have been observed in MSU-X aluminas reported by Pinnavaia.[6] Although the reflection of the calcined material is as broad as that of the as-synthesized material, it is found that the calcination increases the d-spacing from 5.6 to 5.7 nm due to the better condensation of the wall. The same result was also found by Davis *et al.*,[7] in which a shift to higher d spacings is observed upon calcination.

The N_2-adsorption-desorption isotherms and the pore size distributions of both the as-synthesized and the calcined (450 °C) mesoporous aluminas are presented in Fig.4.3. The typical hysteresis loop of the isotherms indicates the existence of mesopores in the materials. The BET surface area is 449 m^2g^{-1}. It is interesting to observe a bimodal distribution from the pore size distribution based on the desorption branch: small pores with average pore diameter of ca. 3.0 nm and large ones between 6.0 and 20.0 nm. The bimodal behavior is very sensitive to the reaction and calcination temperatures (see below). A very well defined bimodal distribution is illustrated in Fig. 4.4e, where the reaction between the starting materials was carried out at 55 °C and the sample was calcined at 750 °C. The small pores correspond to the d-spacing in the range of 5.5 to 6.0 nm in the XRD. The difference between the lattice parameter ($a = 2d_{(100)}/3^{1/2}$), obtained from XRD, and the pore size, found from nitrogen adsorption analysis, indicates that the thickness of the walls around these pores is ca. 3.0 nm. This wall thickness is larger than that of MCM-41.[2,4] This is not unexpected on considering the weaker repulsive interactions between neutral metal precursors at the surfactant-solution interface than between charged precursors. Therefore, the neutral pathway tends to afford structures with thicker framework walls, improved stability, and smaller elementary particle sizes for adding textural mesoporosity.[10] The large pores give no extra reflections in the XRD, and are presumed to be textural mesoporous structures crosslinked by alumina particles. We
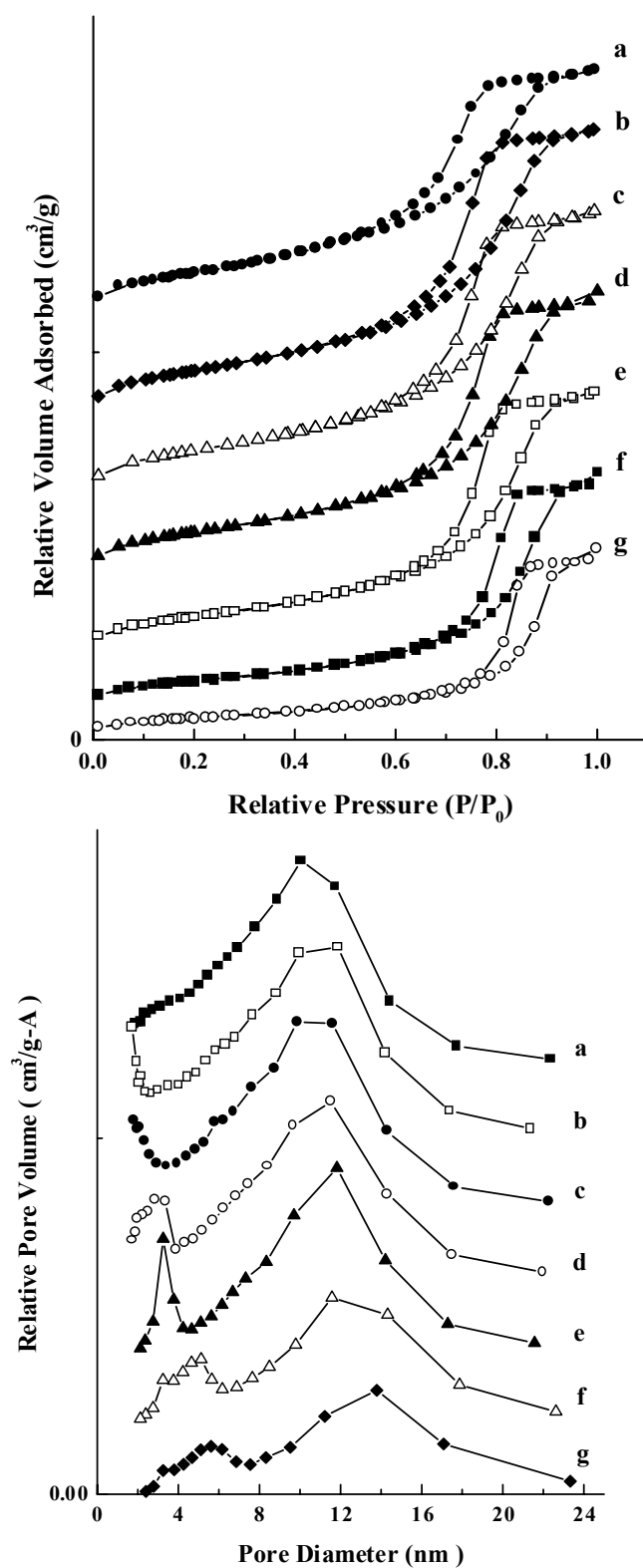
Figure 4.3 N_2-adsorption-desorption isotherms and pore size distributions: (a) the as-synthesized mesoporous alumina synthesized at 80 °C and aged at room temperature; (b) the bimodal mesoporous alumina calcined at 450 °C.

do not believe that the porosity of the large pores is controlled by the template. The characters of these pores are quite similar to those of early reported aluminas which were X-ray amorphous materials and their porosity was purely textural, characterized by wide pore size distributions.[8] Similar bimodal distribution behavior has also been observed in cases of mesoporous silica[15] and aluminosilicate[16]. Pang *et al.*[15] synthesized bimodal mesoporous silica, which contains small pores with an average pore diameter of ca. 3.0 nm and large pores within the range 8.0-20 nm. The small pores correspond to the XRD reflection with a d-spacing of 5.0 nm, and the large pores are formed by packing of small silica particles.

The nature of mesophases, obtained using the neutral surfactant templating route as described here, is influenced by variations in synthetic conditions, e.g. length of surfactant, reaction, aging and calcination temperatures, etc.

The effect of the variation of calcination temperatures is summarized in Fig. 4.4 and Table 4.1. The average pore size of small pores is found to increase with the increasing calcination temperatures up to 750 °C. It would appear that, higher calcination temperatures achieve a better condensation of the pore wall. However, much higher temperatures result in the pore structure collapsing. It was observed that calcination at temperatures between 750 and 950 °C led to structures with small pores partially collapsing. The pore volume decreases from 0.080 to 0.024 cm^3g^{-1}. On the other hand, some pores are generated with pore size distributions centered at ca. 5.0 nm (850 °C) to ca. 6.0 nm (950 °C). The average pore size of large pores increases from 9.6 nm (350 °C) to 11.5 nm (950 °C), due to textural mesoporosity change among the crosslinked particles. Nevertheless, the average pore volume decreases from 0.66 to 0.40 cm^3g^{-1}, due to the fact that the pore structure partially collapses at high temperatures. The BET surface area decreases with increasing calcination temperature, from 398 m^2g^{-1} at 350 °C to 131 m^2g^{-1} at 950 °C. In Fig. 4.5 compares the XRD patterns of the mesoporous alumina obtained at various calcination temperatures. The fact that the d-spacing

Figure 4.4 N$_2$-adsorption-desorption isotherms and pore size distributions of the bimodal mesoporous aluminas calcined at 350 (a), 450 (b), 550 (c), 650 (d), 750 (e), 850 (f) and 950 °C (g). The samples were prepared by using 1-dodecylamine as template at 55 °C and aged at room temperature.
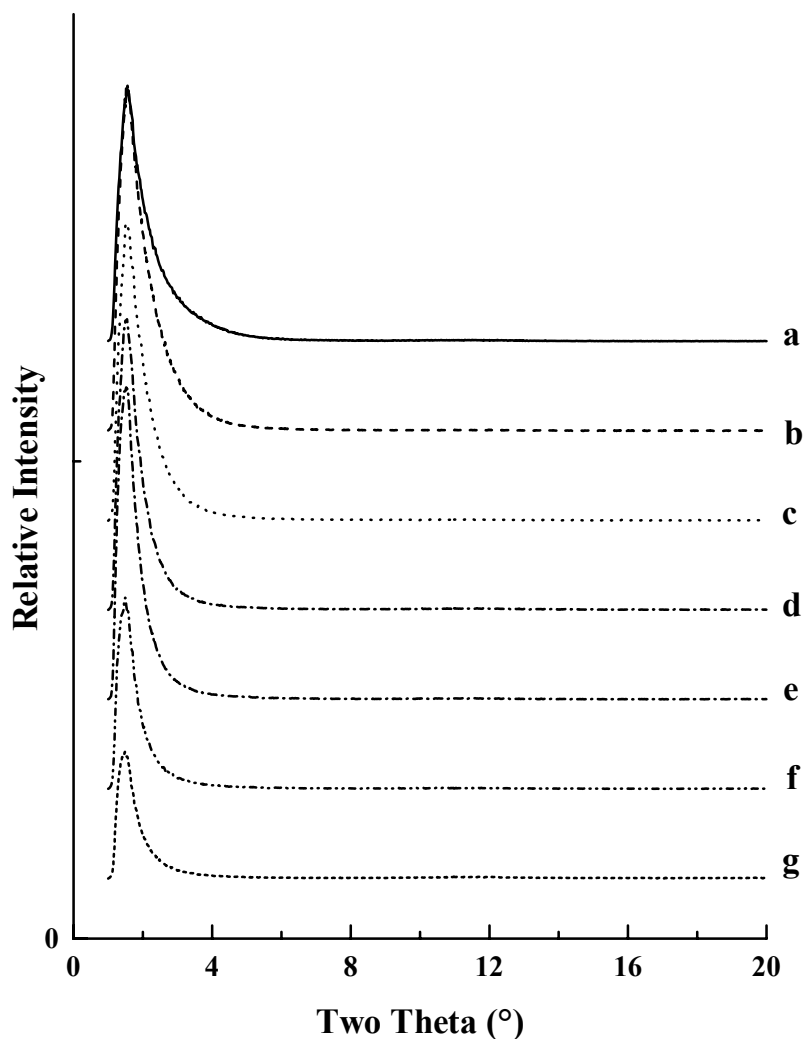
Figure 4.5 X-Ray power diffraction (XRD) patterns of the bimodal mesoporous aluminas calcined at 350 (a), 450 (b), 550 (c), 650 (d), 750 (e), 850 (f) and 950 °C (g). The samples were prepared by using 1-dodecylamine as template at 55 °C and aged at room temperature.

increases from 5.6 to 6.0 nm while the calcination temperature rises from 350 to 950 °C indicates that a high calcination temperature tends to produce better condensation of the pore walls and thus benefits a large pore size. The intensities of the XRD reflections decrease with increasing calcination temperatures. However, the well defined XRD peak still remains after heating the sample at 950 °C (curve g), indicating the existence of the mesostructures and revealing the high thermal stability of the mesoporous alumina. The high thermal stability has
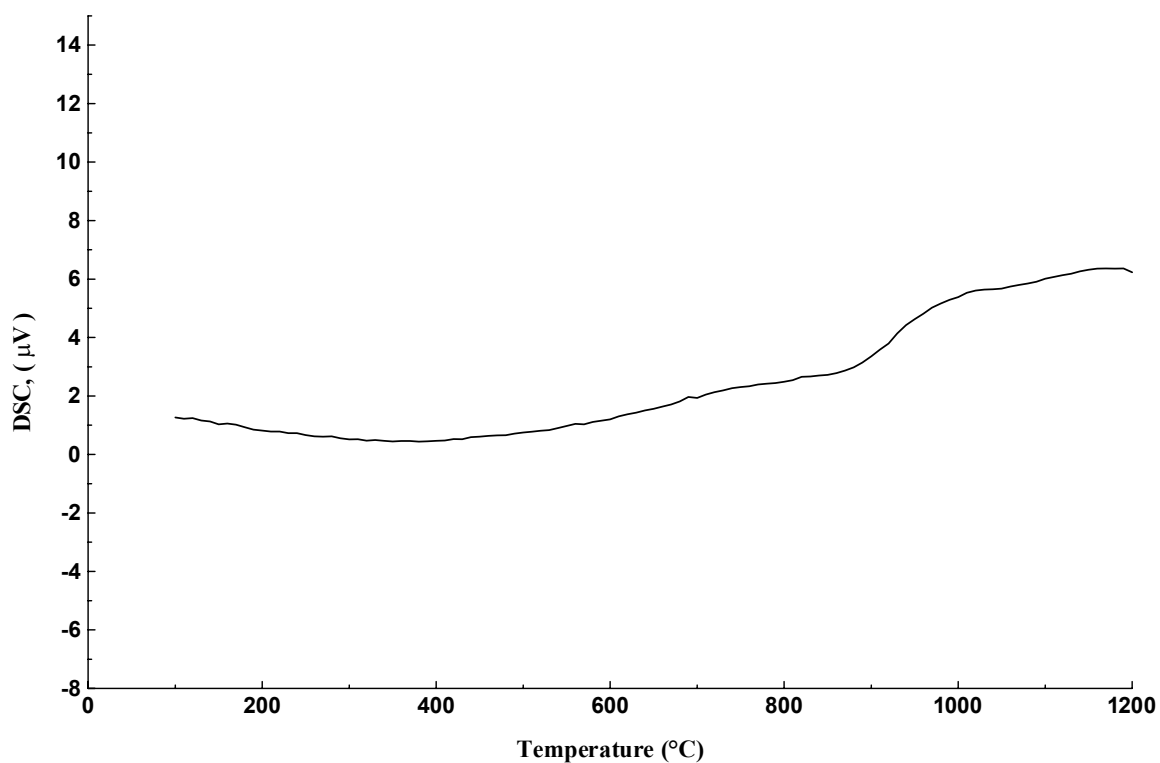
Figure 4.6 DSC plot of the bimodal mesoporous alumina. The sample was prepared by using 1-dodecylamine as template at 55 °C, aged at room temperature and calcined at 450 °C.

also been confirmed by DSC, presented in Fig. 4.6. The endothermic curve between 900 and 1000 °C (heating rate is 10 °C min⁻¹) implies a phase transfer process.

The reaction temperature also affects the mesoporsity of the bimodal mesoporous alumina, as illustrated in Fig. 4.7 and Table 4.1. In the temperature range of 30 to 110 °C, both the small and the large pore diameters increase with the increasing of reaction temperature. The small pore diameter enlarges from 3.0 to 3.6 nm and the pore volume reduces from 0.16 to 0.081 cm^{3}g^{-1}. In principle, the small pores are generated from hydrolysis of template directed micelles, and the formation of micelles is favored at lower temperatures.[17] Higher temperature results in micelles swelling up, therefore the average pore size increases after hydrolysis. But the thermal stability of these pores decreases compared with that of pores with small pore diameters, therefore the pore structure partially collapses

during the process of hydrolysis, and the pore volume decreases. For the large pores, the pore diameter increases from 8.2 to 9.8 nm and the pore volume increases from 0.35 to 1.13 cm^3g^{-1} on increasing the temperature from 30 to 110 °C. Since the higher reaction temperature can increase the random degree of textural porosity, both the average pore diameter and the pore volume increase while increasing reaction temperature.

Table 4.1 Effect of the reaction and calcination temperatures on the pore structures of mesoporous aluminas.[a]

| $T_{reaction}$	$T_{calcination}$	S_{BET}	D_{small}[b]	D_{large}[c]	V_{small}[b]	V_{large}[c]	d_{XRD}
°C	°C	m^2g^{-1}	nm	nm	cm^3g^{-1}	cm^3g^{-1}	nm
55	350	398	3.1	9.6	0.080	0.66	5.6
55	450	396	2.9	9.9	0.087	0.64	5.7
55	550	366	3.0	9.9	0.076	0.63	5.7
55	650	288	2.9	10.2	0.079	0.59	5.7
55	750	202	3.4	10.5	0.052	0.54	5.8
55	850	167	3.7	11.1	0.042	0.47	5.9
55	950	131	3.8	11.5	0.024	0.40	6.0
110	450	450	3.6	9.8	0.081	1.13	5.7
80	450	449	3.6	7.6	0.10	0.86	5.7
55	450	384	3.4	7.6	0.14	0.61	5.7
30	450	421	3.0	8.2	0.16	0.35	5.6

[a] D = average pore diameter, V = pore volume.

[b] Average pore diameter in the range of 1.7 to 5.0 nm.

[c] Average pore diameter in the range of 5.0 to 20.0.

Davis and his co-workers have reported the preparation of mesoporous aluminas by the use of anionic surfactants.[7] The materials have narrow pore size distributions at ca. 2.0 nm that can not be tailored by varying the surfactant length. On the contrary, Pinnavaia and co-workers have reported that both the d-spacing and the pore diameter increase as the surfactant size increasing when using neutral polyethylene oxides as directing agents for the synthesis of mesoporous aluminas.[6] We have investigated the surfactant length effect on the mesoporosity of mesoporous aluminas utilizing 1-dodecylamine and 1-aminoheptane as templates. A comparison of their isotherm plots and pore size distributions is given in Fig. 4.8. It is found that, when using 1-aminoheptane instead of 1-dodecylamine, the XRD d-spacing decreases from 5.73 to 5.59 nm. The average diameter of the small pores (ranging from 1.7 to 5.0 nm) decreases from 3.6 to 3.5 nm. The BET surface area decreases from 449 to 423 m^2g^{-1}. An influencing factor is that the structure of small pores, which are generated from template directed micelles, is affected by the variation of template size. However, the changing of surfactant length does not affect the size of large pores. This is not surprising, because the large pores are assumed to be textural mesoporous structures crosslinked by alumina particles and are not affected by the template.

Fig. 4.9 illustrates the isotherm plots and the pore size distributions of mesoporous aluminas which are synthesized at different aging temperatures. When increasing the aging temperature from 25 to 80 °C, both the d-spacing and the average diameter of small pores decrease from 5.7 to 5.5 nm and 3.6 to 3.3 nm, respectively. This is probably because the higher aging temperature increases crystallinity and condensation in the walls, which has been previously proposed by Antonelli *et al*. in the preparation of Nb-TMS.[17] They found that, when the aging temperature increased from 100 to 180 °C, the d-spacing of Nb-TMS decreased from 4.0 to 3.4 nm. On the other hand, the large pore size increases from 7.6 to 8.5 nm and the BET surface area decreases from 449 to 293 m^2g^{-1} on increasing the aging
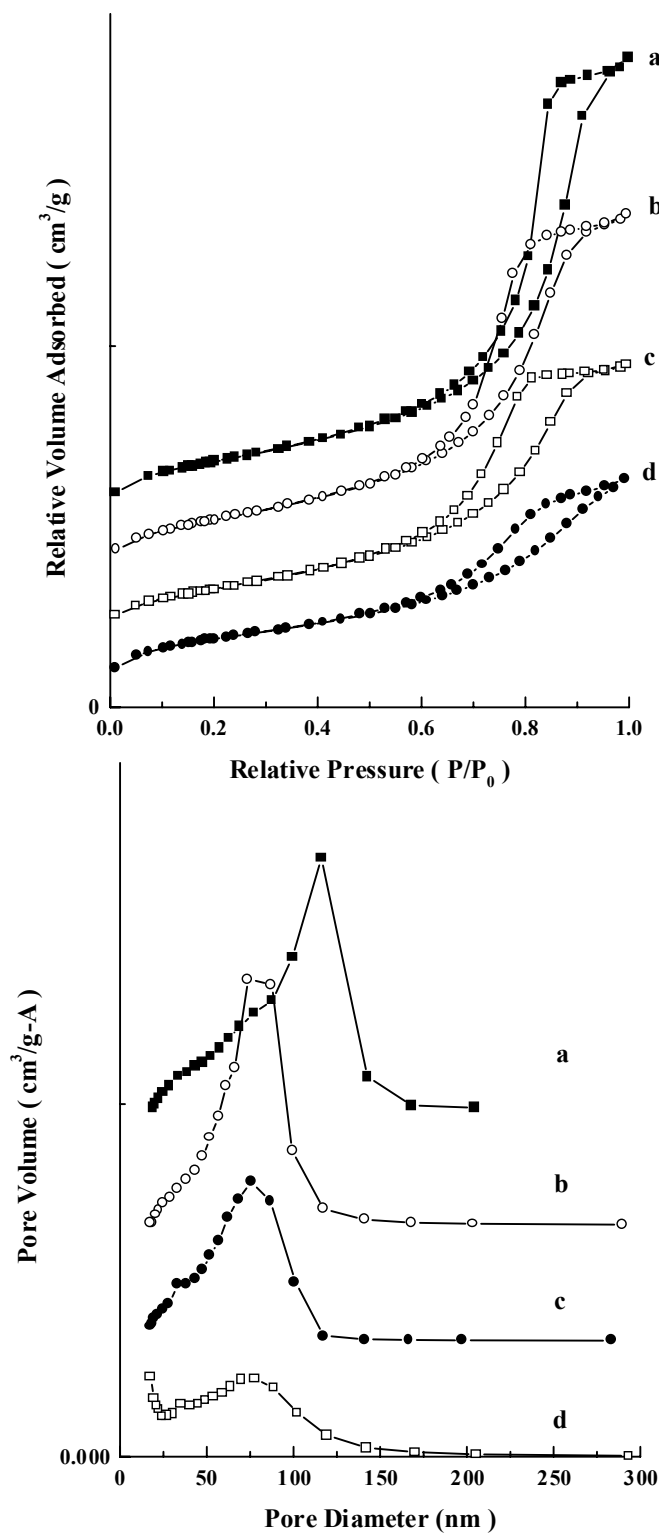
Figure 4.7 N$_2$-adsorption-desorption isotherms and pore size distributions of the calcined bimodal mesoporous aluminas prepared at different reaction temperatures: 110 (a), 80 (b), 55 (c) and 30 °C (d). The samples were synthesized using 1-dodecylamine as template, aged at room temperature and calcined at 450 °C.
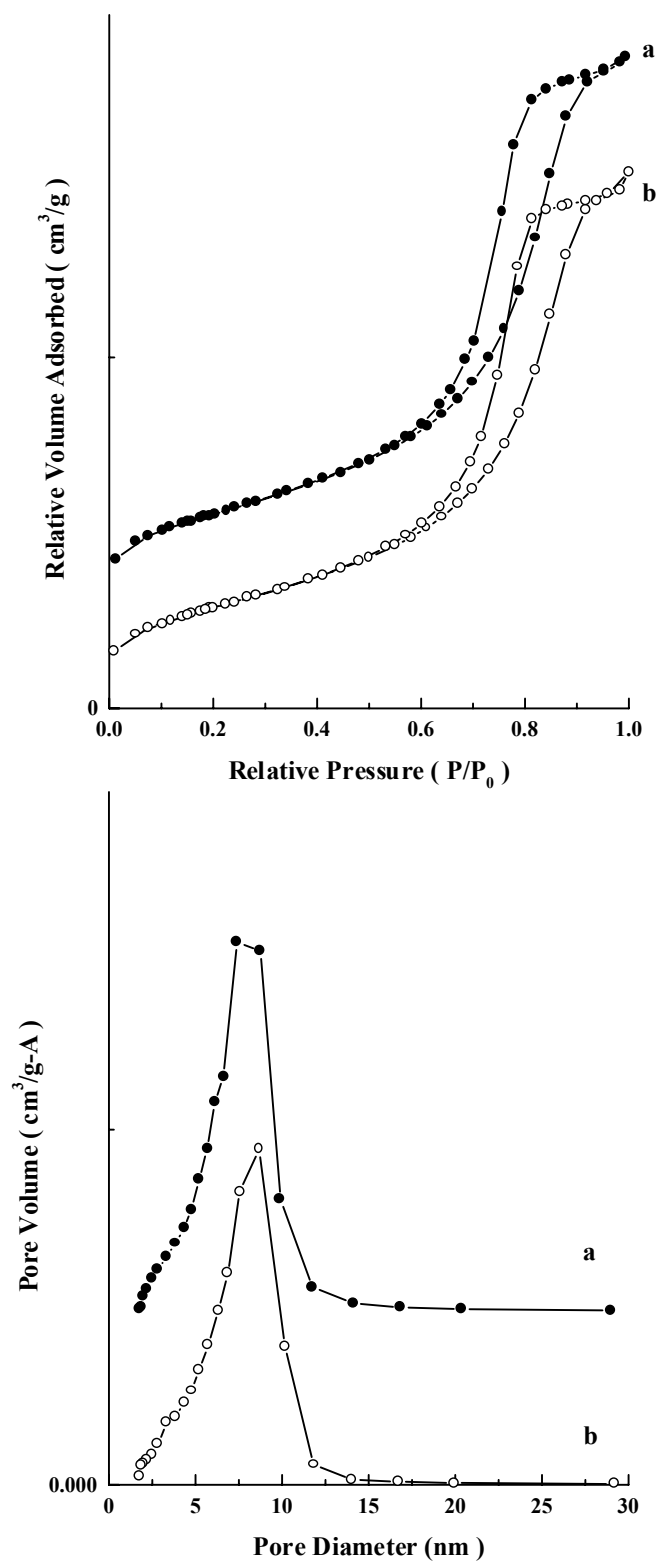
Figure 4.8 N_2-adsorption-desorption isotherms and pore size distributions of the calcined

bimodal mesoporous aluminas synthesized using (a) 1-dodecylamine and (b) 1-aminoheptane

as templates. The samples were prepared at 55 °C reaction temperature and calcined at 450

°C.
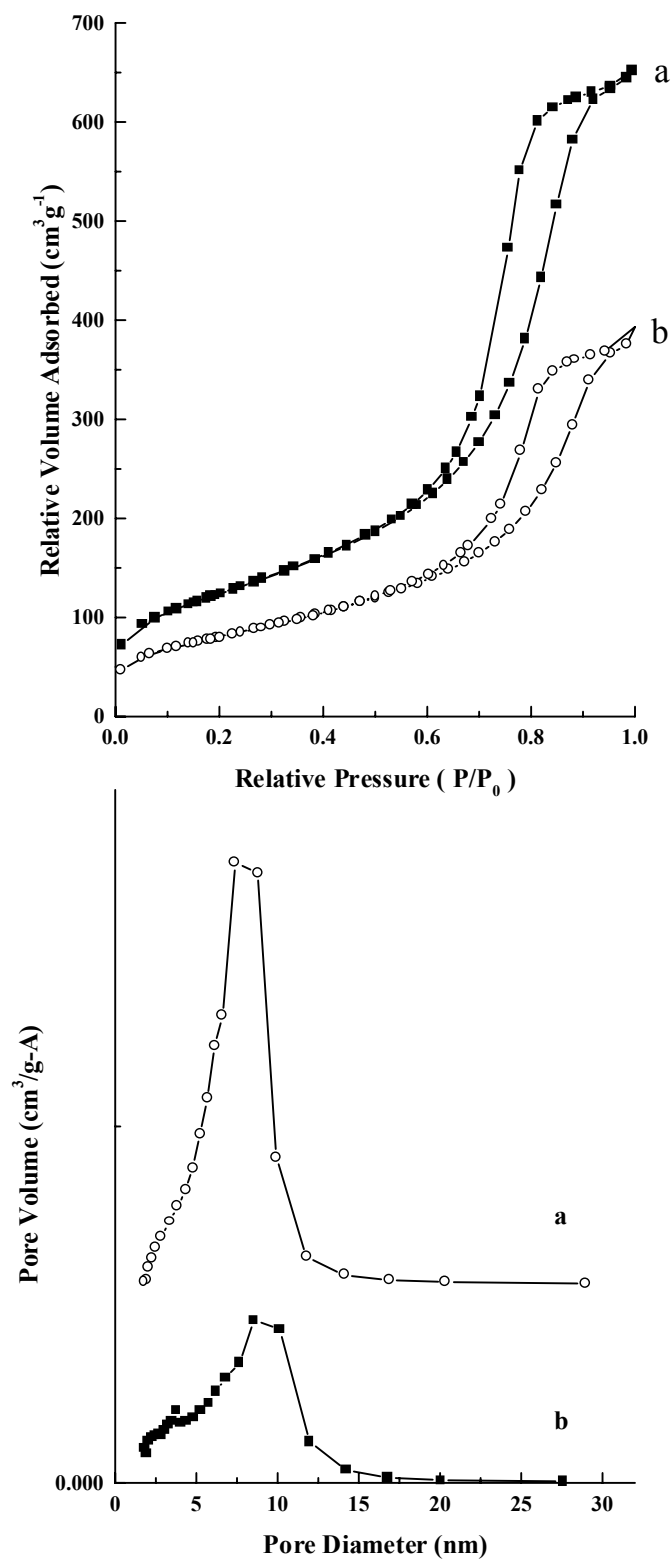
Figure 4.9 A comparison of N_2-adsorption-desorption isotherms and pore size distributions of the calcined bimodal mesoporous aluminas between aging temperatures of 25 °C (a) and 80 °C (b). The samples were prepared using 1-dodecylamine as template at 55 °C and calcined at 450 °C.

temperature from 25 to 80 °C. The reason is that the random degree of textural structure increases and the textural pores partially collapse during the hydrothermal treatment at high temperatures.[9,18]

In conclusion, mesoporous alumina can be prepared by a neutral surfactant templating method. These materials are thermally stable up to 950 °C. An unusual bimodal mesoporous structure is observed. The porous structure is influenced by template size, and reaction, aging and calcination temperatures, etc. The variation of template size only affects the structure of small pores, but not the size of large pores. High reaction temperature helps to increase BET surface area and pore size. Low aging temperature benefits to pore structure and thermal stability. Higher calcination temperature enhances the condensation of the pore walls, however, much higher temperature (over 750 °C) leads to pore structure partially or completely collapse. Calcination at 750 °C produces the mesoporous alumina with the most distinguished bimodal structure. The prepared bimodal mesoporous alumina exhibits high catalytic activity for $DeNO_x$ reaction, which is presented in Chapter 5.

References

1. J. S. Beck, US-A 5057296, **1991**.

2. C. T. Kresge, M. E. Leonowicz, W. J. Roth, J. C. Vartuli, J. S. Beck, *Nature* **1992**, *359*, 710.

3. Q. Huo, D. I. Margolese, U. Cielsa, D. G. Demuth, P. Feng, T. E. Gier, P. Sieger, A. Firouzi, B. F. Chemlka, F. Schüth, G. Stucky, *Chem. Mater.* **1994**, *6*, 1176.

4. Q. Huo, D. I. Margolese, U. Cielsa, P. Feng, T. E. Gier, P. Sieger, R. Leon, P. M. Petroff, F. Schüth, G. Stucky, *Nature* **1994**, *368*, 317.

5. U. Cielsa, D. Demuth, R. Leon, P. M. Petroff, G. Stucky, K. Unger, F. Schüth, *J. Chem. Soc., Chem. Commun.* **1994**, 1387.

6. S. A. Bagshow, T. J. Pinnavaia, *Angew. Chem. Int. Ed. Engl*. **1996**, *35*, 1102.

7. F. Vaudry, S. Khodabandeh, M. E. Davis, *Chem. Mater*. **1996**, *8*, 1451.

8. S. Cabrera, J. El Haskouri, J. Alamo, A. Beltrán, D. Beltrán, S. Mendioroz, M. D. Marcos, P. Amorós, *Adv. Mater*. **1999**, *11*, 379.

9. P. T. Tanev, T. J. Pinnavaia, *Science* **1995**, *267*, 865.

10. S. A. Bagshow, E. Prouzet, T. J. Pinnavaia, *Science* **1995**, *269*, 1242.

11. S. G. Wilkinson, *Comprehansive Coordination Chemistry* (Pergamon Press) Vol.3, **1987.**

12. M. E. Davis, C. Chen, S. L. Burkett, R. F. Lobo, *Mater. Res. Soc. Symp. Proc*. **1994**, *346*, 831.

13. C.-Y. Chen, H.-Y. Li, M. E. Davis, *Microporous Mater*. **1993**, *2*, 17.

14. X. Wang, T. Dou, Y. Xiao, *Chem. Commun*. **1998**, 1035.

15. W. Lin, J. Chen, Y. Sun, W. Pang, *Chem. Commun*. **1995**, 2367.

16. Z. Yuan, J. Wang, H. Li, *Chinese Chem. Lett*. **1997**, *10*, 927.

17. D. M. Antonelli, A. Nakahira, J. Y. Ying, *Inorg. Chem*. **1996**, *35*, 3126.

18. Z. Luan, H. He, W. Zhou, C. Cheng, J. Klinowski. *J. Chem. Soc., Faraday Trans.* **1995**, *91*, 2955.

Chapter 5. Catalytic Application of Mesoporous Metal Oxides in Decomposition of NO$_x$

5.1. Introduction

Stringent emission control requirements have stimulated the development of various NO$_x$ control technologies over the last few decades. For stationary NO$_x$ sources such as power plants, and for mobile sources such as gasoline fueled engines working under stoichiometric air/fuel ratios, technical solutions are available.[1,2] Recently, diesel and lean-burn gasoline fueled engines have attracted considerable attention due to their high fuel efficiency and lower emission of carbon dioxide. These types of engines present new challenges for NO$_x$ emission control, as they generally operate under net oxidizing conditions under which typical three-way catalysts show little activity towards NO$_x$ reduction.[1,2] On the other hand, as NH$_3$ is not suitable for application as a reducing agent in motor vehicles, increased effort has been put into the development of suitable catalysts capable of reducing NO$_x$ in the presence of O$_2$ with hydrocarbons as reducing agents.[2-4] This process is the so-called hydrocarbon selective catalytic reduction (HC-SCR) of nitrogen oxides.

In general three types of catalysts are active for the HC-SCR of NO$_x$: zeolites, metal oxides and noble metals. The catalysts, which are based on metal ion exchanged zeolites, show very high activity.[5] However these materials have shown limited hydrothermal stability. Supported noble metal catalysts, which are active at low temperatures, produce substantial amounts of N$_2$O. A wide variety of metal oxides (bulk or supported) exhibit a moderate activity. A major advantage of these catalysts is that a large selection of reducing agents can be used. The drawbacks lie in the high operation temperature, the low activity at high space velocity, and the deactivation of the catalysts by sulphur dioxide and thermal aging due to loss of specific area. In order to make application feasible, high space velocity performance,

selectivity behaviour and durability of the lean NO_x catalysts in the presence of steam and sulphur oxides need to be improved.

In the past decade, the sol-gel process offered a possibility to prepare high-purity materials with a mesoporous pore distribution and a high surface area. Such materials have ideal properties for applications as catalyst supports. A number of attempts at catalytic reduction of NO_x have been carried out over mesoporous molecular sieves.[6-13] However, sol-gel-processed materials have not yet found applications in automotive catalysts due to the cost considerations and the loss of beneficial properties of the materials at elevated temperatures. These materials can only be used in applications where temperatures are not extremely high or the cost is offset by a reduced use of platinum group metals. Therefore, preparing $DeNO_x$ catalysts that are thermally stable, highly active and cheap in cost is still demanding.

In this chapter, we report an initial investigation on the applications of mesoporous alumina- and titania-based catalysts in $DeNO_x$ reactions.

5.2. Results and Discussion

5.2.1. Synthesis and Characterization of Catalysts

The synthesis of the mesoporous alumina was reported in Chapter 4. Fig. 5.1a illustrates the isotherm plot and the pore size distribution of the material. The pore size distribution shows a bimodal character: small pores with an average pore diameter of ca. 3.0 nm and large pores within the range of 6.0 to 20.0 nm. The BET surface area is calculated as 414 m^2g^{-1}, the pore volume is 0.951 cm^3g^{-1} and the average pore diameter is 6.9 nm. The mesoporous alumina powder was compressed into disks in a steel die of 10 mm diameter by applying a pressure of 500 N/mm^2, and the disks were crushed and sieved into pellets with diameters between 0.2 to 0.3 mm. The N_2-adsorption-desorption isotherm plot and the pore

size distribution of the compressed sample are shown in Fig. 5.1b. The shift of hysteresis loop to lower relative pressure relative to Fig. 5.1a indicates the decrease of the pore size. It is interesting to find that, upon mechanical treatment, the BET surface area, the pore volume and the average pore diameter decreased to 412 m^{2}g^{-1}, 0.654 cm^{3}g^{-1} and 5.1 nm, respectively. We assume that the major reason is due to the rearrangement of the textural structure under the high mechanical pressure and the partially blocking of pores. A similar effect of mechanical treatment on the mesoporous structures of silica has been reported by Hartmann *et al.*[14] They found that, the adsorption capacity of MCM-41 and MCM-48 was affected considerably by mechanical compression between 20 and 400 N/mm^2, while the material was destroyed to a large extend between 480 and 600 N/mm^2. The loss of surface area and pore volume at low compression pressure was due to the blocking of some pores by other particles. The three-dimensional arrangement of the pore system and high wall thickness of the MCM-48 system resulted in higher stability than that of MCM-41, which has one-dimensional channel system.

The CuO/*meso*-Al$_2$O$_3$ catalyst was prepared by using a precipitation method. The mesoporous alumina was suspended in an aqueous CuCl$_2$ solution. Dropwise addition of NH$_3$·H$_2$O (25%) led to Cu(OH)$_2$ precipitation on the Al$_2$O$_3$ surface. The solid was collected, washed with water until no Cl$^-$ was detected, dried at 120 °C, and calcined at 400 °C for 2 h. The CuO/*meso*-Al$_2$O$_3$ containing 8.8% of copper was obtained, as confirmed by elemental analysis. The catalyst powder was compressed into disks, and then crushed and sieved into pellets with diameters between 0.2 to 0.3 mm, as described above. In the X-ray diffraction pattern (Fig. 5.2b) a broad reflection around 2θ = 37.0° corresponds to CuO and Al$_2$O$_3$.[15,16] As shown in Fig. 5.3, the type IV isotherm similar to the parent mesoporous alumina was obtained for the CuO/*meso*-Al$_2$O$_3$, providing strong evidence that the mesoporous structure of the alumina support was retained throughout the grafting process. The pore size distribution still shows a bimodal structure after grafting CuO. Comparing to the data of the compressed pure mesoporous alumina (Fig. 5.1b), the BET surface area of the compressed CuO/*meso*-
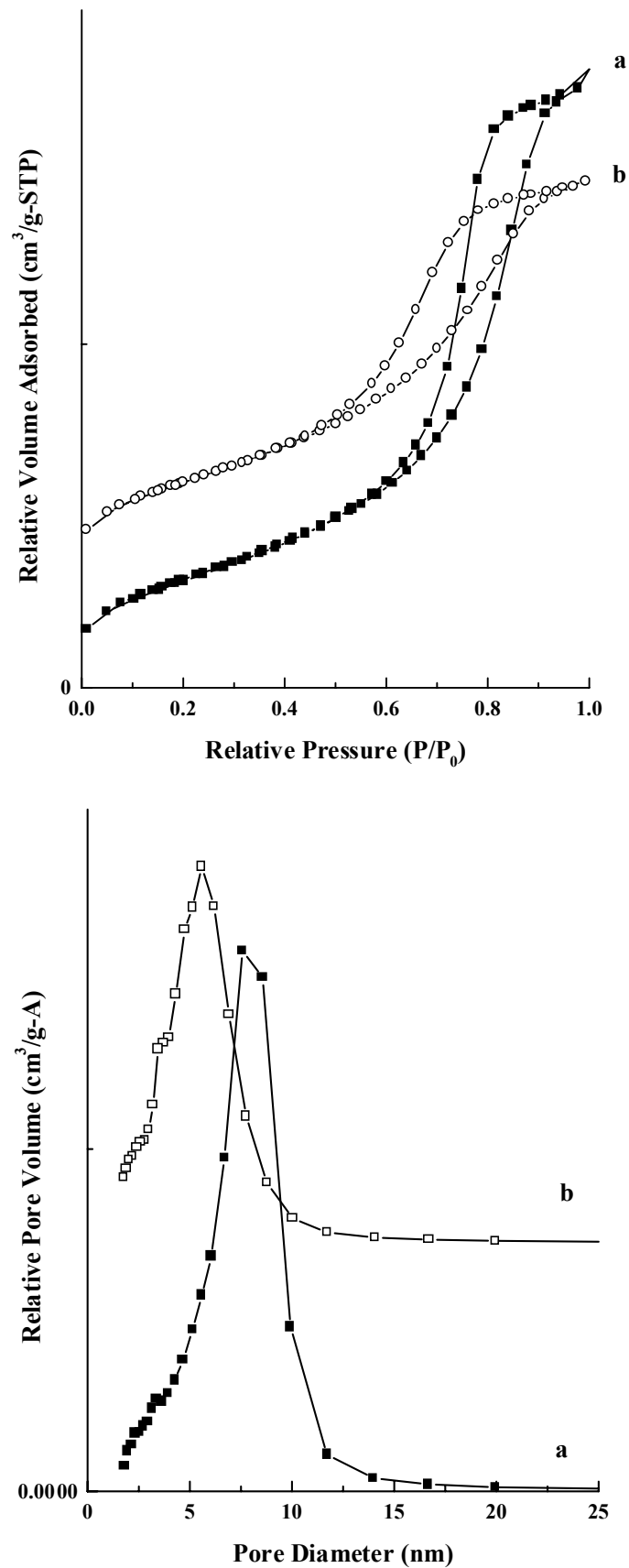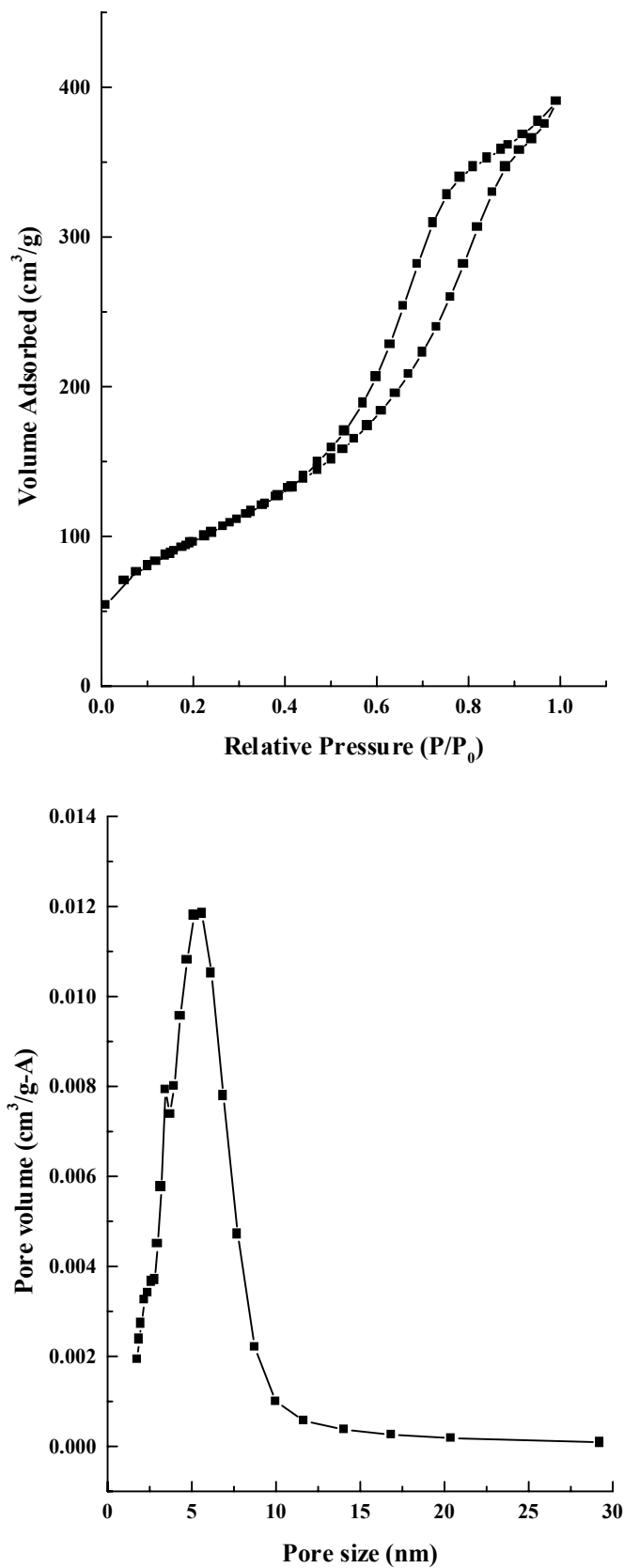
Figure 5.1 Isotherm plots and pore size distributions of (a) mesoporous alumina powder, and

(b) mesoporous alumina pellets compressed under a pressure of 500 N/mm^2.

Al$_2$O$_3$ decreased from 413 to 355 m^{2}g^{-1}, the pore volume reduced from 0.645 to 0.585 cm^{3}g^{-1}, and the average pore diameter increased slightly from 5.1 to 5.2 nm.
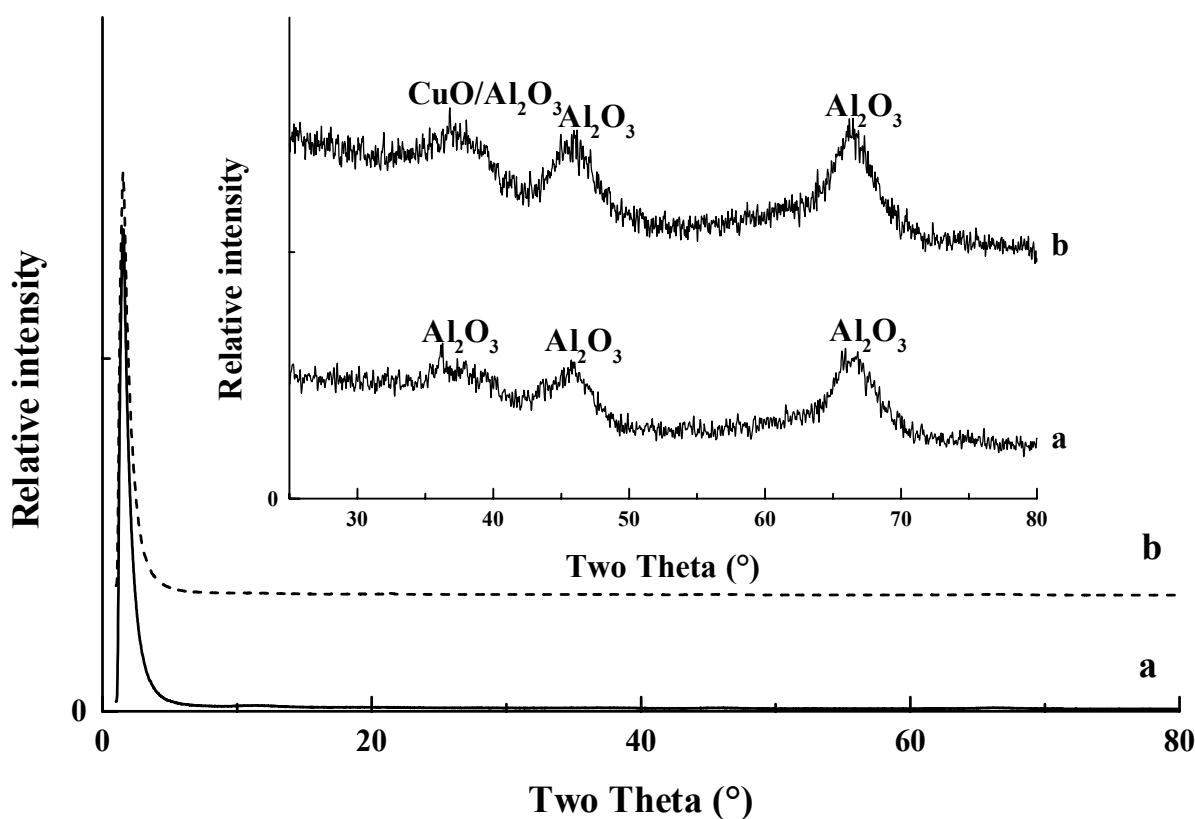

Figure 5.2 XRD patterns of (a) the pure mesoporous alumina and (b) the CuO/*meso*-Al$_2$O$_3$ catalyst.

The ZnO/*meso*-Al$_2$O$_3$ catalyst containing 7.7% of zinc, as confirmed by elemental analysis, was prepared by the same method described above for CuO/*meso*-Al$_2$O$_3$, using ZnCl$_2$ instead of CuCl$_2$. The catalyst powder was also compressed, crushed and sieved into pellets with diameters between 0.2 to 0.3 mm before use in the DeNO$_x$ reaction. Fig. 5.4 compares the isotherm plots and the pore size distributions of ZnO/*meso*-Al$_2$O$_3$ before and after the mechanical treatment. Both of them still retain the type IV isotherm plots. The pore size distributions show that the high-pressure mechanical treatment reduces pore size but does not change the bimodal character. Similar to mesoporous Al$_2$O$_3$ and CuO/*meso*-Al$_2$O$_3$, upon

Figure 5.3 Isotherm plot and pore size distribution of the CuO/*meso*-Al$_2$O$_3$ catalyst pellets compressed under a pressure of 500 N/mm^2.
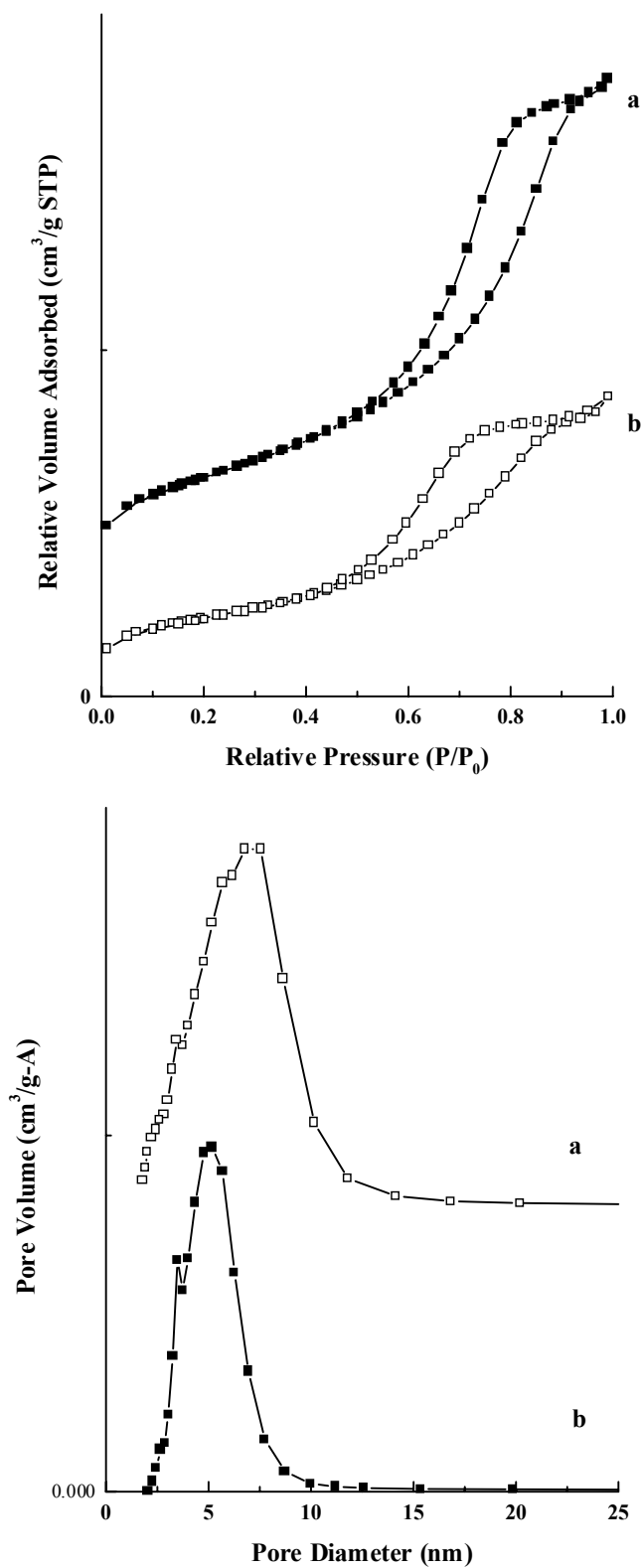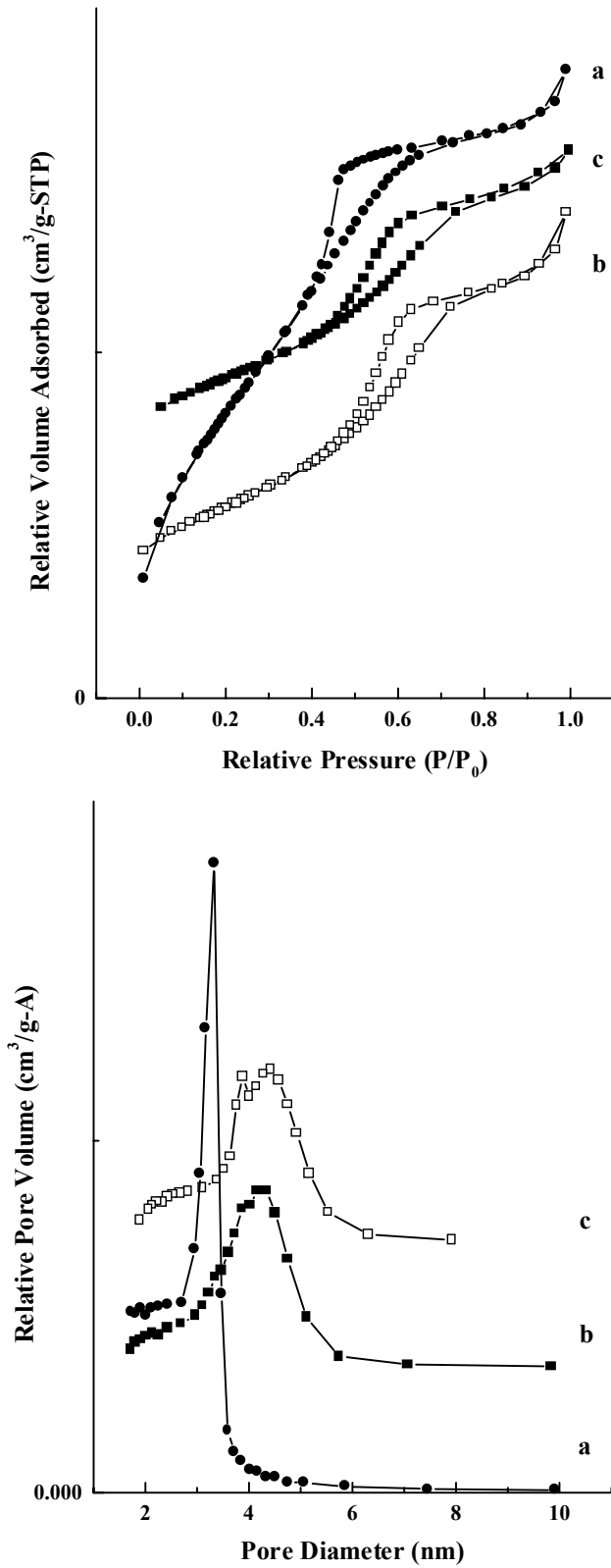
Figure 5.4 Isotherm plots and pore size distributions of (a) the ZnO/*meso*-Al$_2$O$_3$ catalyst powder, and (b) the ZnO/*meso*-Al$_2$O$_3$ catalyst pellets compressed under a pressure of 500 N/mm^2.

mechanical treatment the BET surface area, the pore volume and the average pore diameter of ZnO/*meso*-Al$_2$O$_3$ decreases from 395 to 263 m^{2}g^{-1}, from 0.739 to 0.425 cm^{3}g^{-1} and from 6.0 to 5.1 nm, respectively. In comparison to the pure mesoporous alumina (see above and Fig. 5.1), grafting ZnO on the *meso*-Al$_2$O$_3$ surface resulted in the decrease of both the BET surface area and the pore volume, but the average pore diameter did not change significantly.
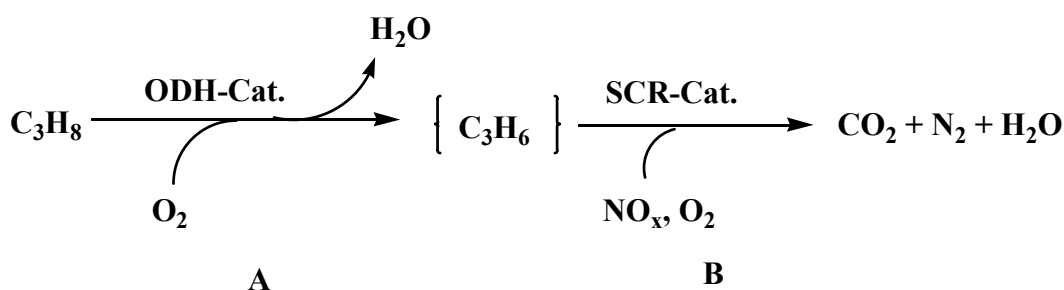
The synthesis of the pure mesoporous titania was reported in Chapter 2. Fig. 5.5a illustrates the type IV isotherm plot, and the sharp and narrow pore size distribution of the mesoporous titania before calcination. The BET surface area is calculated as 654 m^{2}g^{-1}, the pore volume is 0.438 cm^{3}g^{-1} and the average pore diameter is 2.8 nm. Upon calcination at 400 °C, the pore size distribution became broader due to the condensation of the pore wall and the pore structure partially collapsing. Thus the average pore size increased to 3.8 nm. Moreover, some large pores formed due to pore wall collapse. As a result, the BET surface area and the pore volume decreased to 230 m^{2}g^{-1} and 0.285 cm^{3}g^{-1}, respectively (Fig. 5.5b). The calcined mesoporous titania powder was compressed, crushed and sieved into pellets with diameters between 0.2 to 0.3 mm as described above for the other catalysts. The N$_2$-adsorption-desorption isotherm plot and the pore size distribution of the compressed sample are shown in Fig. 5.5c. In contrast to mesoporous Al$_2$O$_3$, CuO/*meso*-Al$_2$O$_3$ and ZnO/*meso*-Al$_2$O$_3$, the mechanical treatment enhanced the BET surface area of the titania to 300 m^{2}g^{-1}. The pore volume and the average pore diameter were also found to increase to 0.298 cm^{3}g^{-1} and 3.9 nm, respectively. This suggests that the high-pressure mechanical treatment does not significantly influence the mesoporous structure of titania. The high-pressure stability of mesoporous titania is attributed to its framework structure. The relative thick pore walls help to increase the high-pressure stability. In contrast, the textural structured mesoporous alumina shows a relatively low mechanical stability due to the existence of textural mesoporosity among the crosslinked particles.

Figure 5.5 Isotherm plots and pore size distributions of mesoporous titania powder before calcination (a) and after calcination (b), and mesoporous titania pellets compressed under a pressure of 500 N/mm^2 (c).

5.2.2. Catalytic Decomposition of NO$_x$

Propene has usually been used as an active reducing agent for catalytic DeNO$_x$ reactions.[17] Recently, propane has attracted considerable attention as a replacement of propene for HC-SCR DeNO$_x$ reactions, taking into account the cheap cost of propane and that the active reducing agent propene can be generated through the process of oxidative dehydrogenation of propane as shown in Scheme 5.1.[18]

$$C_3H_8 \xrightarrow[\;O_2\;]{\text{ODH-Cat.}} \{\, C_3H_6 \,\} \xrightarrow[\;NO_x, O_2\;]{\text{SCR-Cat.}} CO_2 + N_2 + H_2O$$

$$\text{(H}_2\text{O)}$$

A   B

Scheme 5.1 Proposed reaction mechanism of HC-SCR DeNO$_x$ process: (a) C_3H_6 is generated from oxidative dehydrogenation of C_3H_8; (b) C_3H_6-SCR DeNO$_x$ process.

Catalytic measurements were performed on a fully computer-controlled microreactor system, which is described in detail in Chapter 8. Standard experiments were carried out at atmospheric pressure using 800 mg of catalyst. C_3H_8 was used as a reducing agent. The samples were pretreated at 450 °C for 25 min. with a flow of He before measurements.

Subsequently, the reactant gas mixture of O_2, C_3H_8, NO$_x$ and He, as specified in Chapter 8, was passed through the catalyst bed. Steady-state measurements of the temperature dependence of the catalytic activity were performed by raising the temperature from 250 to 650 °C in steps of 50 °C, with a typical duration of the isothermal steps of 30 min.

Fig. 5.6a and Fig. 5.6b depict the conversion of NO$_x$ to N_2 and the conversion of C_3H_8 to CO_2, respectively, as a function of temperature for various mesoporous alumina based C_3H_8-SCR DeNO$_x$ catalysts. It is found that, mesoporous alumina catalyst (BET surface area

ca. 400 m^{2}g^{-1}) is more active than commercial alumina catalyst (200 m^{2}g^{-1}), especially at high temperature of 550 °C. The specific feature of mesoporous alumina, high surface area and large pore diameter, can be a reason for the improved catalytic activity, since large pores benefit to the diffusion of reactants and products in and out the catalyst particles. Another possible reason is due to the incomplete oxidation of C$_3$H$_8$ in the case of mesoporous alumina. As shown in Fig. 5.6b, the conversion of C$_3$H$_8$ over mesoporous alumina is lower than that over commercial alumina between 300 to 550 °C. Bog has found that the incomplete oxidation of C$_3$H$_8$ benefits to the conversion of NO$_x$.[19] As shown in Fig. 5.6a, when the temperature is higher than 550 °C, the conversion of NO$_x$ declines. The reason is that the conversion of C$_3$H$_8$ to CO$_2$ reaches ca. 100% at temperature over 550 °C, and no more reductant exists in the system.

Since surface acidity and redox ability of catalysts might be important for HC-SCR DeNO$_x$,[18] catalysts CuO/*meso*-Al$_2$O$_3$ and ZnO/*meso*-Al$_2$O$_3$ were prepared and their catalytic behaviours were examined. Fig. 5.7 shows that the conversion of NO$_x$ to N$_2$ over CuO/*meso*-Al$_2$O$_3$ catalyst is higher than over pure mesoporous Al$_2$O$_3$ at low temperatures in the range of 300 to 400 °C. The same tendency is observed for the conversion of C$_3$H$_8$ to CO$_2$. It is assumed that, at low temperatures, the grafted CuO increases the catalytic activity in oxidative dehydrogenation of propane (Scheme 5.1), so as to enhance the conversion of NO$_x$. The conversion of NO$_x$ decreases when temperature is higher than 450 °C, because the conversion of C$_3$H$_8$ to CO$_2$ reaches ca. 100% at 450°C. On the other hand, the ZnO/*meso*-Al$_2$O$_3$ catalyst is less active than the pure mesoporous alumina catalyst in the range of 300 to 600 °C. This suggests that the existence of ZnO in the catalyst system does not benefit to the DeNO$_x$ reaction.

It was reported that, a non-mesoporous titania catalyst (BET surface area ca. 45 m^{2}g^{-1}) showed relatively high catalytic activity for HC-SCR DeNO$_x$ reaction in the temperature range of 300-400 °C while using C$_3$H$_6$ as a reducing agent.[19] When C$_3$H$_8$ was used instead of
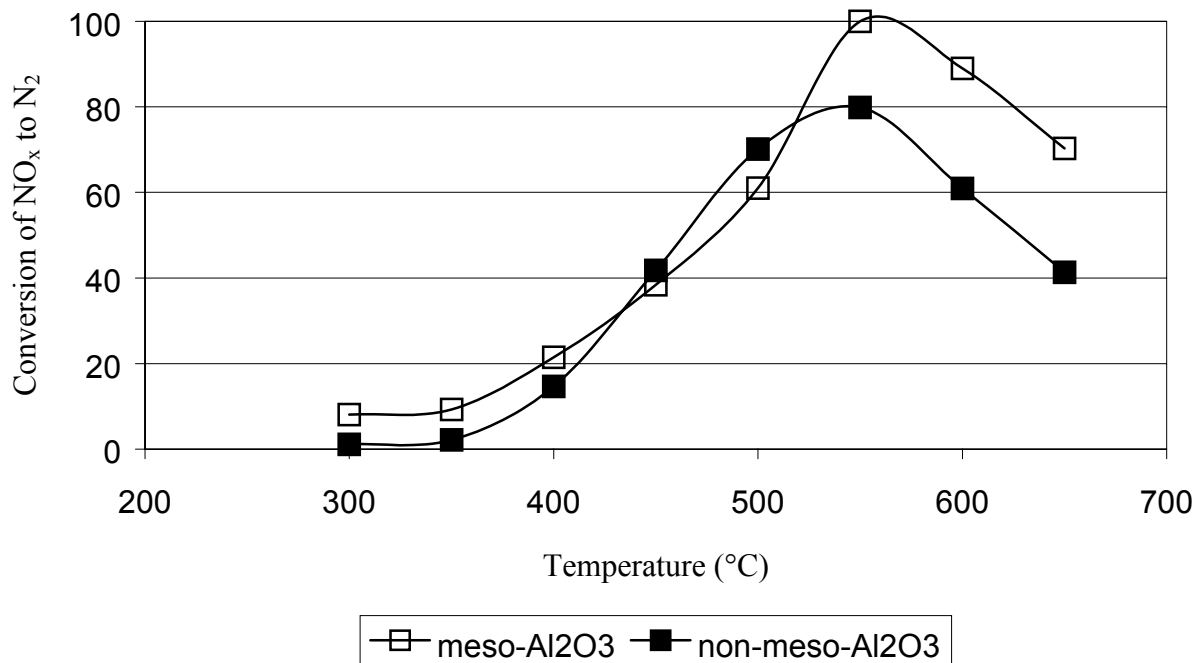
(a)
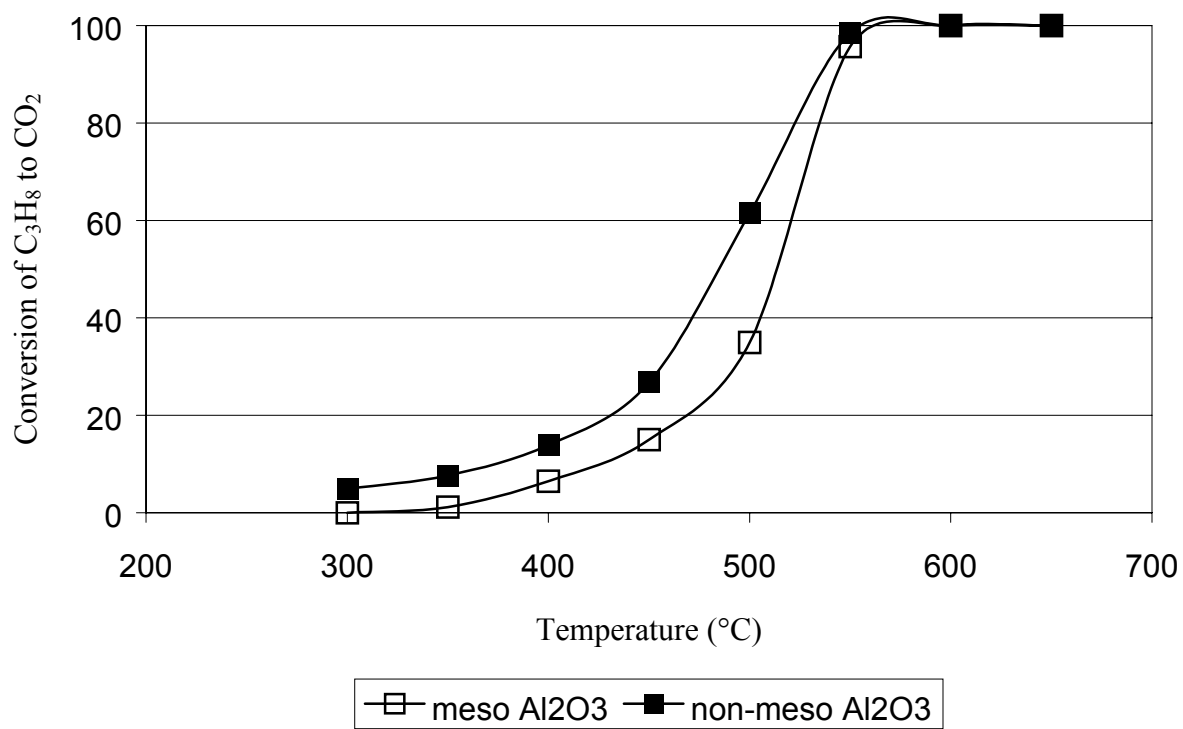
(b)

Figure 5.6 (a) Conversion of NO_x to N_2 and (b) conversion of C_3H_8 to CO_2 over mesoporous alumina and commercial alumina.

(a)
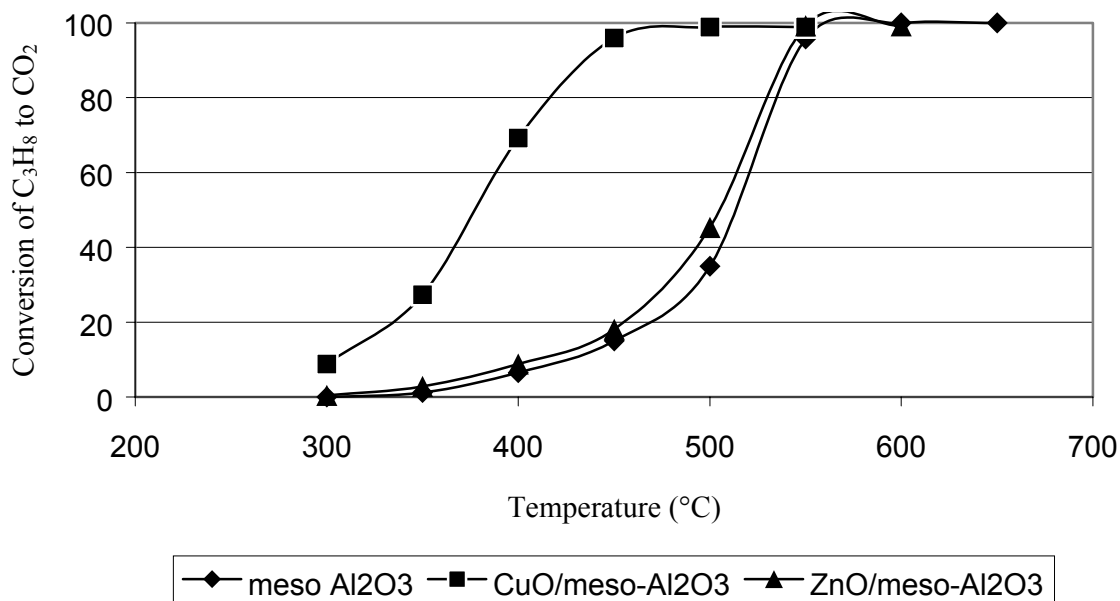
(b)

Figure 5.7 (a) Conversion of NO$_x$ to N$_2$ and (b) conversion of C$_3$H$_8$ to CO$_2$ over mesoporous
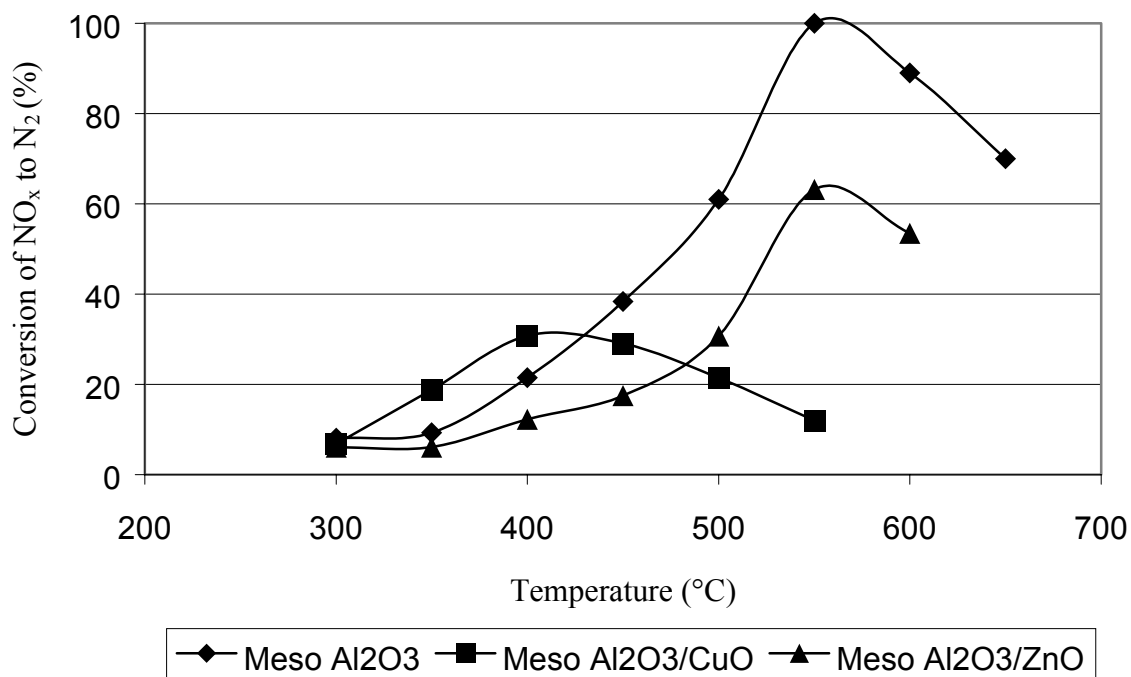
alumina, CuO/*meso*-Al$_2$O$_3$ and ZnO/*meso*-Al$_2$O$_3$ catalysts.

(a)

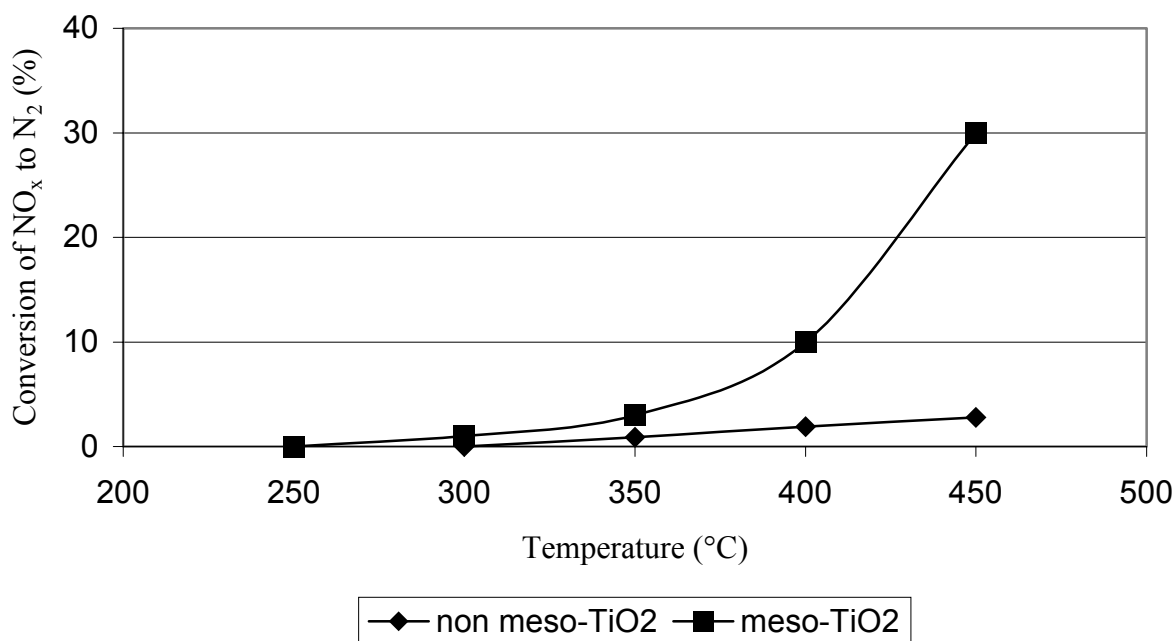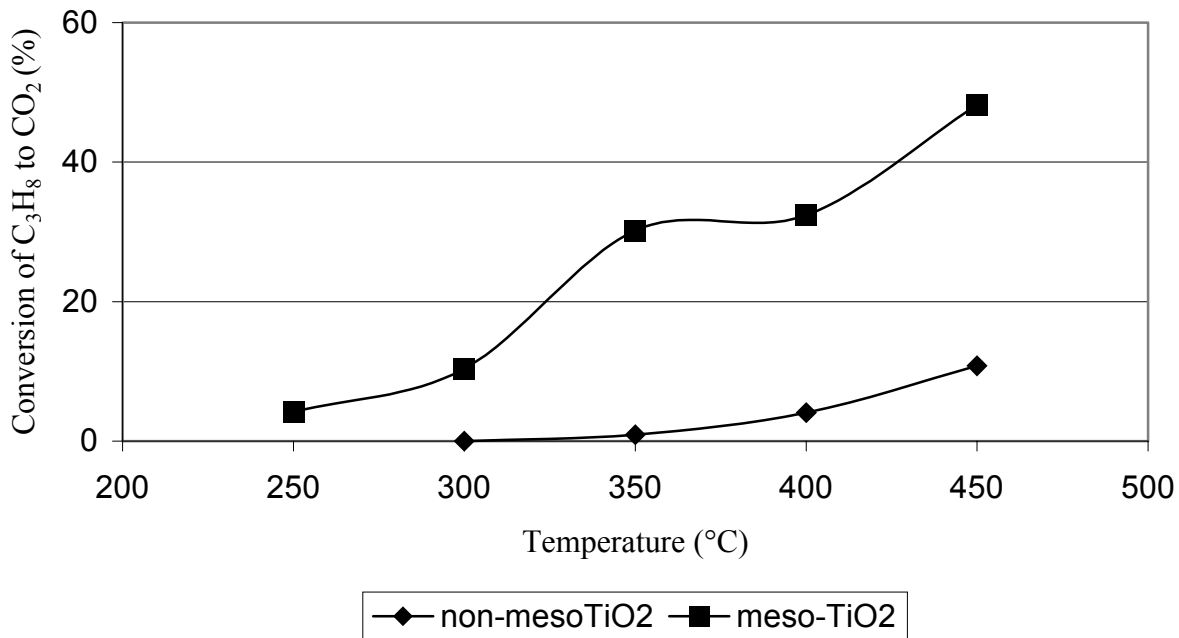
(b)

Figure 5.8 (a) Conversion of NO_x to N_2 and (b) conversion of C_3H_8 to CO_2 over mesoporous titania and non-mesoporous titania catalysts.

C_3H_6, the conversions of both NO_x to N_2 and C_3H_8 to CO_2 were reduced tremendously (Fig. 5.8). However, the mesoporous titania catalyst (BET surface area ca. 300 m^2g^{-1}) exhibits much improved conversion of NO_x and C_3H_8 for C_3H_8-SCR DeNO$_x$ reaction at low temperatures in the range of 300 to 400 °C, in comparison to the non-mesoporous titania catalyst. It was suggested that the superior activity of the large-pore zeolite Co/beta in C_3H_8-SCR could be ascribed to the ease of diffusion of reactants, products and inhibitors such as water and SO_2 in its channels.[20,21] By contrast, the low activity of Co/ferrierite was attributed to the hindered diffusion in its small pores.[21,22] Thus, in our case, we presume that the high BET surface area and the large pore size of the mesoporous titania catalyst are responsible for the high activity in C_3H_8-SCR DeNO$_x$.

In summary, mesoporous metal oxides (*e.g.* alumina and titania) indeed show promising advantages as a catalyst or a catalyst support in DeNO$_x$ reaction, due to their high BET surface areas and large pore sizes.

References

1. K. C. Taylor, *Catal. Rev.-Sci. Eng.* **1993**, *35*, 457.

2. M. Shelef, *Chem. Rev.* **1995**, *95*, 209.

3. M. Iwamoto, H. Yahiro, S. Shundo, Y. Yu-u, and N. Mizuno, *Shokubai*, **1990**, *32*, 430.

4. W. Held, A. König, T. Richter, L. Puppe, *SAE Tech. Pap. Ser.* **1990**, *810,* 13.

5. F. Radtke, R. A. Koeppel, E. G. Minardi, A. Baiker, *J. Catal.* **1997**, *167*, 127.

6. M. Hatanaka, et al. *Eur. Pat. Appl.* **2000**.

7. S. Higashimoto, et al. *Chem. Lett.* **2000**, *4*, 408.

8. W. Schiesser, et al. *Catal. Lett.* **1999**, *56*, 189.

9. G. Moretti, et al. *Appl. Catal. B* **1999**, *20*, 67.

10. T. J. Pinnavaia, W. Zhang, *Stud. Surf. Sci. Catal.* **1998**, *117*, 23.

11. S. Nojima, et al. *Jpn. Kokai Tokkyo Koho,* **1998**.

12. C. K. Narula, et al. *Ceram. Trans*. **1997**, *73*, 15.

13. M. Nakao, S. Nishiyama, S. Tsuruya, M. Masai, *Inorg. Chem*. **1992**, *31*, 4662.

14. M. Hartmann, C. Bischof *J. Phys. Chem. B*. **1999**, *103*, 6230.

15. H.-F. Chang, M. A. Saleque, W.-S. Hsu, W.-H. Lin, *J. Mol. Catal. A: Chem.* **1996**, *109*, 249.

16. T. J. Richardson, J. L. Slack, M. D. Rubin, *4th International Meeting on Electrochromism*, **2000**, Uppsala, Sweden.

17. T. Ishihara, M. Kagawa, F. Hadama, Y. Takita, *J. Catal*. **1997***, 169,* 93.

18. K. C. C. Kharas, D.-J. Liu, H. J. Robota, *Catal. Today* **1995***, 26*, 129.

19. T. W. Bog, Ph.D thesis, Technischen Universität München, Germany, **1999**.

20. T. Tabata, M. Kokitsu, H. Ohtsuka, O. Okada, L. M. F. Sabatino, G. Bellussi, *Catal. Today* **1996**, *27*, 91.

21. T. Tabata, H. Ohtsuka, L. M. F. Sabatino, G. Bellussi, *Micropor. Mesopor. Mater*. **1998**, *21*, 517.

22. O. Okada, T. Tabata, M. Kokitsu, H. Ohtsuka, L. M. F. Sabatino, G. Bellussi, *Appl. Surf. Sci.* **1997**, *121/122*, 267.

Chapter 6. Catalytic Application of Mesoporous Metal Oxides in Dehydrogenation of Benzyl Alcohol

6.1. Introduction

The oxidation of alcohols to the corresponding aldehydes and ketones is one of the most fundamental and important processes in organic synthesis and the chemical industry. From the economical and environmental points of view, the advantage of the gas-phase catalytic oxidation is apparent.[1] There has been considerable research in the field of alcohol dehydrogenation focusing on the SiO_2, Al_2O_3 and zeolites supported metal/metal ion/metal oxide catalysts.[2-11] In the chemical process industry, catalysts with high activity, selectivity and long lifetime are essential. To meet these requirements, catalysts should possess a large and thermally stable active surface area. Therefore, the newly generated mesoporous materials, *e.g.* mesoporous titania and alumina, should be promising candidates for catalyst supports. Among the metal oxide catalysts, basic oxides such as ZnO, MgO, Cr_2O_3 and CuO are active for alcohol dehydrogenation.[12] Thus we have prepared mesoporous titania and alumina supported CuO and ZnO catalysts, and investigated their promising applications in benzyl alcohol dehydrogenation (Equation 6.1).

$$(6.1)$$
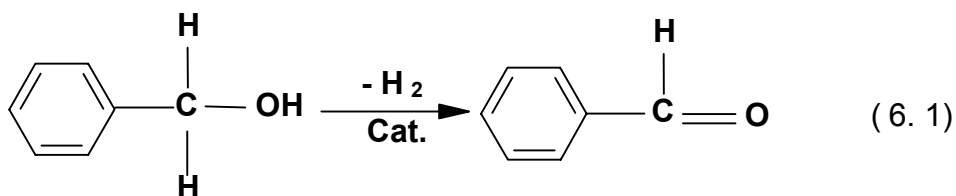
6.2. Results and Discussion

6.2.1. Synthesis and Characterization of Catalysts

6.2.1.1. Mesoporous Alumina Supported Catalysts

The mesoporous alumina supported CuO catalysts with various copper contents were prepared by a precipitation method. The catalysts were characterized by elemental analysis, XRD and N_2-adsorption-desorption method. The isotherm plots and the pore size distributions of the pure mesoporous alumina and the CuO/*meso*-Al_2O_3 catalysts containing various amounts of Cu are shown in Fig. 6.1. Type IV isotherms, similar to the pure mesoporous alumina, were obtained for the CuO/*meso*-Al_2O_3 catalysts, providing strong evidence that the mesoporous structure was retained throughout the grafting process. Moreover, the pore size distributions show that the well-defined bimodal mesoporous structure still exists upon grafting CuO. The pore volume data listed in Table 6.1 reveal that precipitation of CuO

Table 6.1 Elemental analysis and N_2-adsorption-desorption experiment results of CuO/*meso*-Al_2O_3 catalysts with various amounts of copper.

wt.%						S_{BET}	V^a	D^b
C	H	N	Al	Cl	Cu	m^2g^{-1}	cm^3g^{-1}	nm
0.43	1.33	0.00	39.9	0.10	8.8	355	0.585	5.2
0.30	1.60	0.00	40.6	0.05	6.4	353	0.559	5.0
0.51	1.73	0.00	42.0	0.00	4.0	365	0.591	5.1
0.66	2.3	0.00	41.0	0.00	0.0	413	0.645	5.1

[a] Pore volume; [b] Pore diameter.
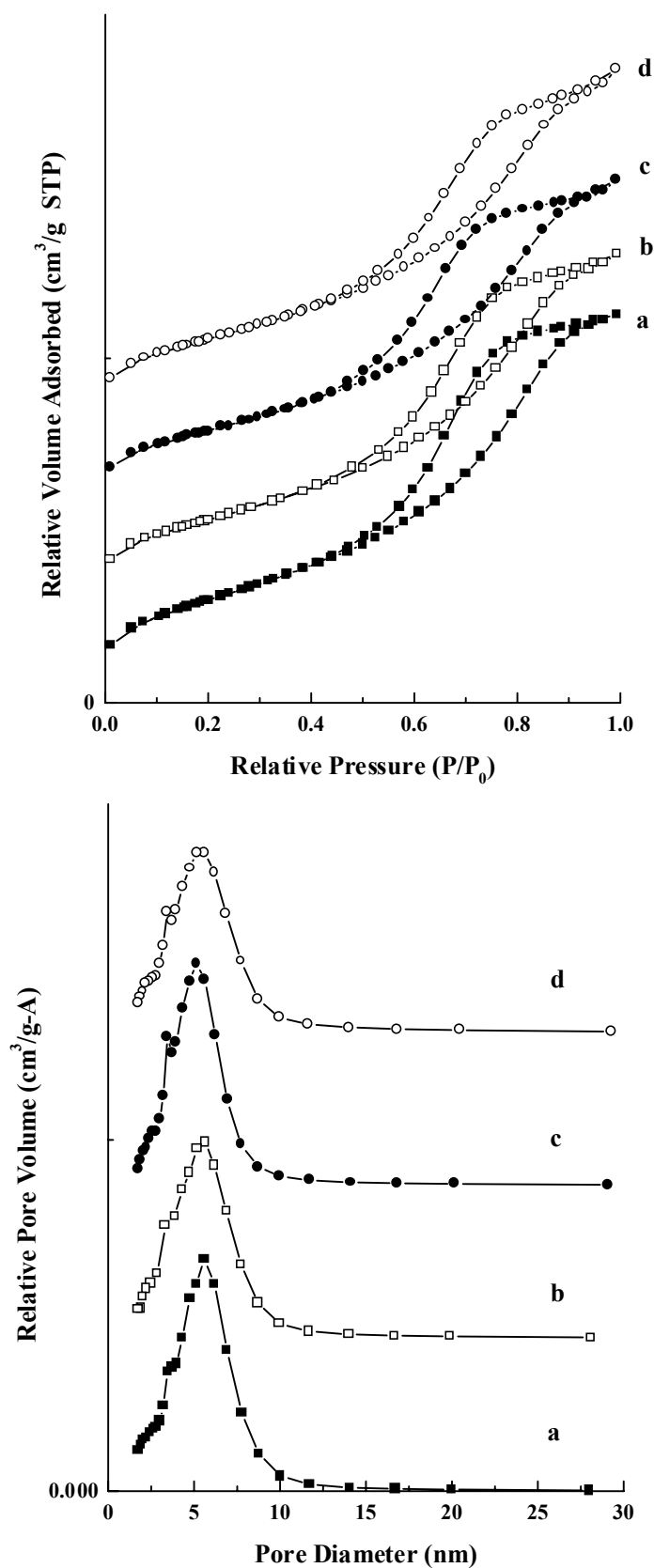
Figure 6.1 N_2-adsorption-desorption isotherm plots and pore size distributions of the pure mesoporous alumina catalyst (a), and CuO/*meso*-Al_2O_3 catalysts with Cu loadings of 4.0% (b), 6.4% (c) and 8.8% (d).
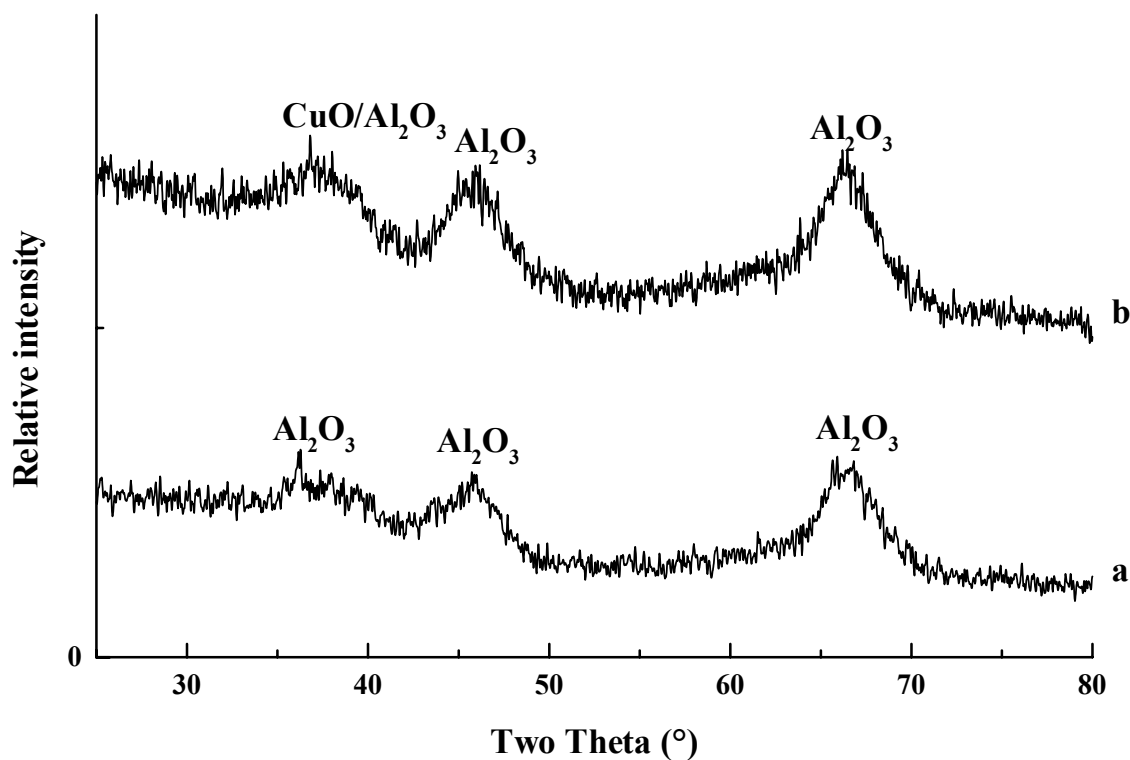
Figure 6.2 X-ray diffraction patterns of the pure mesoporous alumina (a), and the freshly prepared CuO/*meso*-Al$_2$O$_3$ (Cu wt.% = 6.4%) (b) in the range of 25-80°.

decrease pore volumes. In the X-ray diffraction patterns of the CuO/*meso*-Al$_2$O$_3$ catalysts shown in Fig. 6.2, the typical crystalline CuO reflections at 2θ of 35.6, 35.4 and 38.8° provide further evidence for the existence of CuO on mesoporous alumina.

The ZnO/*meso*-Al$_2$O$_3$ catalyst was also prepared by using a precipitation method. The synthesis and characterization are presented in Chapter 5.

6.2.1.2. Mesoporous Titania Supported Catalysts

The pure mesoporous titania, which was reported in Chapter 2, was applied as a catalyst in HC-SCR of nitrogen oxides (Chapter 5). Here the pure mesoporous titania catalyst is examined in catalytic dehydrogenation of benzyl alcohol. Moreover, CuO/*meso*-TiO$_2$

catalysts with various copper contents were prepared by using a precipitation method with pure mesoporous titania as a parent support. The mesoporous titania was suspended in an aqueous $CuCl_2$ solution. Dropwise addition of $NH_3.H_2O$ (25%) led to $Cu(OH)_2$ precipitation on the TiO_2 surface. The solid was washed with water until no Cl^- was detected, dried, and calcined at 400 °C. The obtained CuO/*meso*-TiO_2 catalyst powder was compressed into disks in a steel die of 10 mm diameter by applying a pressure of 500 N/mm^2, and the disks were crushed and sieved into pellets with diameters between 0.2 to 0.3 mm.

Table 6.2 N_2-adsorption-desorption analysis results of the mesoporous titania supported catalysts.

	Catalyst powder			Compressed catalyst		
Cu wt.%	S_{BET}/m^2g^{-1}	V^a/cm^3g^{-1}	D^b/nm	S_{BET}/m^2g^{-1}	V^a/cm^3g^{-1}	D^b/nm
9.3	227	0.273	3.54	243	0.254	3.37
7.2	176	0.233	3.94	198	0.236	3.69
4.9	211	0.257	3.59	209	0.222	3.42
2.4	258	0.291	3.43	221	0.241	3.47
1.2	258	0.295	3.48	254	0.259	3.30
0	230	0.285	3.84	300	0.298	3.90

[a] Pore volume; [b] Pore diameter.

These catalysts were characterized by elemental analysis and N_2-adsorption-desorption method (Table 6.2). As in the alumina case, it was found that grafting of CuO decreases the pore volumes and the average pore diameters, due to CuO covering the surfaces of the pores. The isotherm plots and the pore size distributions of the CuO/*meso*-TiO_2 before and after the mechanical treatment are shown in Fig. 6.3 and Fig. 6.4, respectively. All isotherm curves are
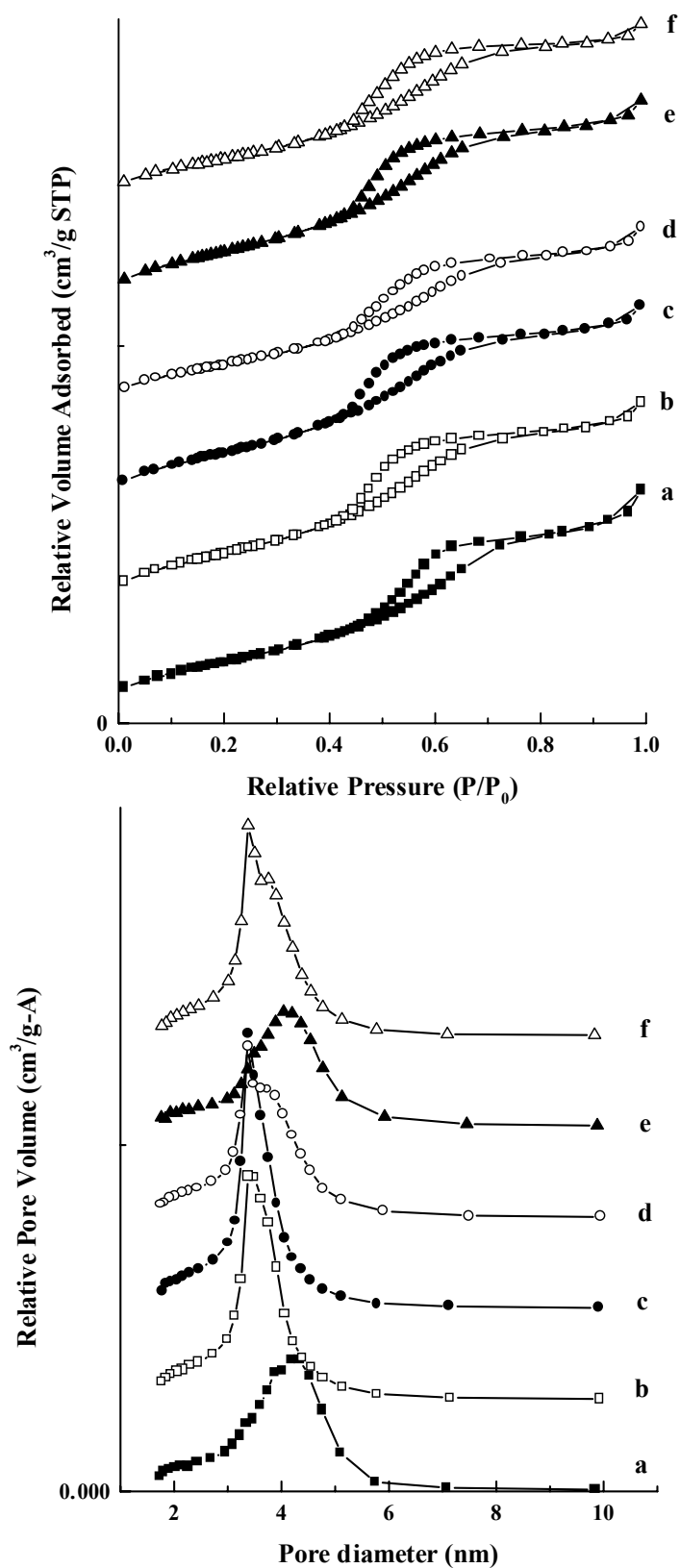
Figure 6.3 Isotherm plots and pore size distributions of the pure mesoporous titania (a), the CuO/*meso*-TiO₂ catalysts containing 1.2% (b), 2.4% (c), 4.9% (d), 7.2% (e) and 9.3% (f) of Cu. All the samples were measured before the mechanical treatment.
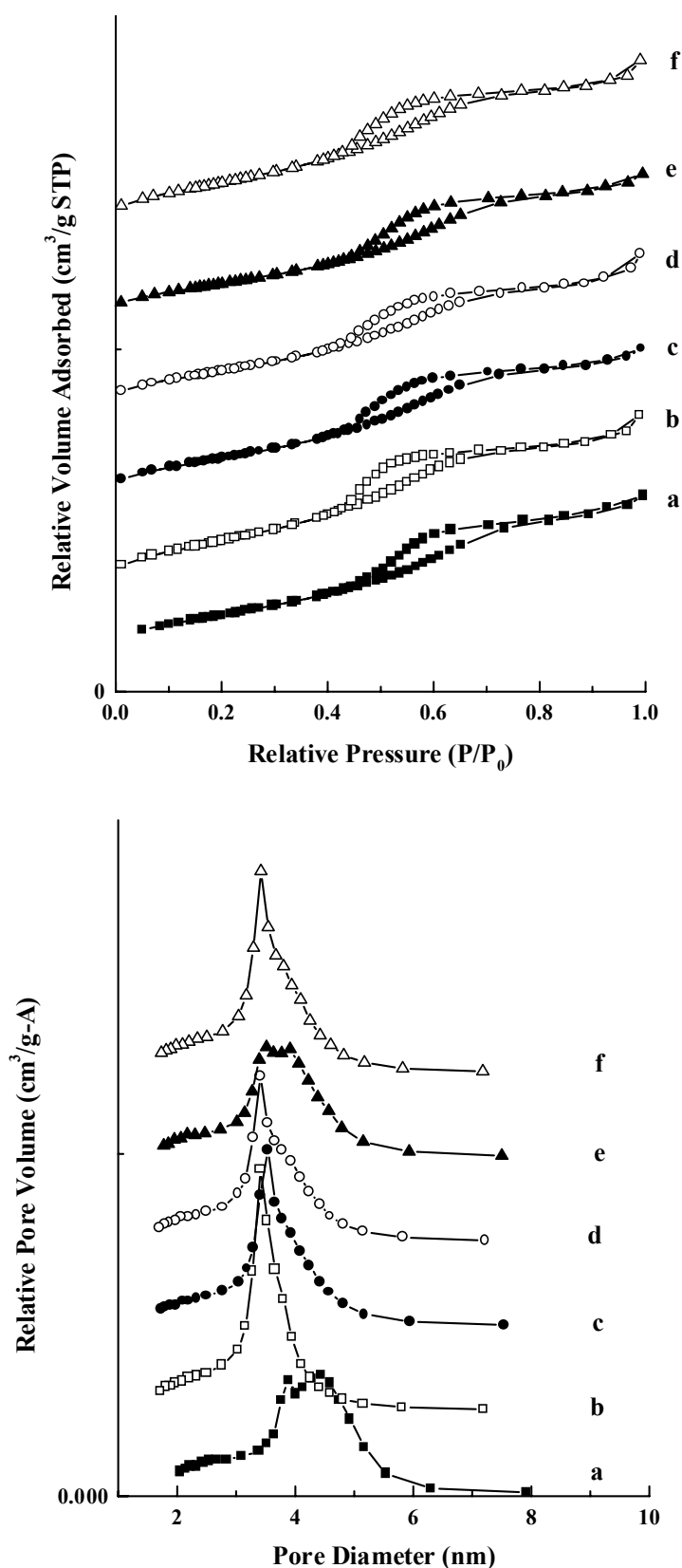
Figure 6.4 Isotherm plots and pore size distributions of the pure mesoporous titania (a), the CuO/*meso*-TiO$_2$ catalysts containing 1.2% (b), 2.4% (c), 4.9% (d), 7.2% (e) and 9.3% (f) of Cu. All the samples were measured after the mechanical treatment.

similar. The typical type IV isotherms, containing hysteresis loops, provide strong evidence for the existence of hexagonal mesoporous structure. Table 6.2 presents a comparison of BET surface area, pore volume and average pore diameter between catalyst power and compressed catalyst. It is found that pore volumes and average pore diameters are only slightly reduced by mechanical treatment. This is due to the blocking of some pores by other particles. A similar effect of mechanical treatment on the mesoporous structures of silica has been reported by Hartmann et al.[13]

A detailed comparison of pore size distributions between CuO/*meso*-TiO$_2$ powder (Fig. 6.3) and compressed catalyst (Fig. 6.4) reveals that, mechanical treatment does not change the center of the pore size distribution, but the shoulder is obviously reduced in size. The major part of pores is framework-structured mesopores that are not easily affected by mechanical pressure, as discussed above. On the other hand, shoulder in the pore size distribution comes from partially collapsed pores that are not as resistant to high pressure as framework-structured pores.

Comparing to the mesoporous titania case, the same mechanical treatment on CuO/*meso*-Al$_2$O$_3$ changed pore structural data significantly (section 5.2.1). The major reason was assumed to be the rearrangement of the textural structure under the high mechanical pressure. We presume, thereby, that such mechanical treatment can only significantly influence structures of inter particle pores; whereas pores with framework structures, e.g. in the cases of mesoporous titania and CuO/*meso*-TiO$_2$, can not be affected to a great extent.

6.2.2. Catalytic Applications in Dehydrogenation of Benzyl Alcohol

Initial attempts were carried out by using pure mesoporous titania and CuO/*meso*-TiO$_2$ as catalysts. The conversions of benzyl alcohol only reached 30-50%. One of the major problems related to their low activity is assumed to be due to deactivation by coke formation

and pore plugging that hinder the diffusion of reactants and products in and out the catalyst particles. A competition with the dehydrogenation of benzyl alcohol is reactions to form toluene and benzyl ether (Equation 6.2). As shown in Fig. 6.5, the main product is toluene when using pure mesoporous titania and CuO/*meso*-TiO$_2$ as catalysts. However, the selectivity to toluene decreases with increasing Cu content. In contrast, the selectivity to benzaldehyde increases when the content of Cu increases.

(6.2)
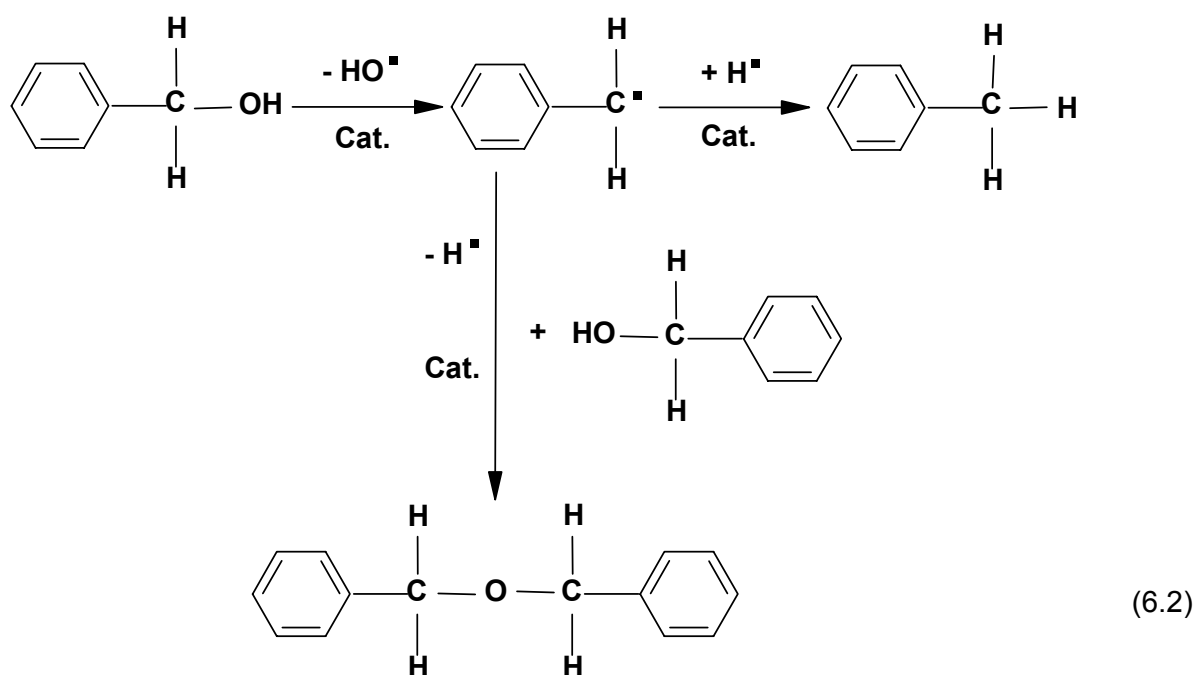
For a comparison, CuO/*ana*-TiO$_2$ with 6.3% of Cu was prepared by a similar methodology for CuO/*meso*-TiO$_2$, using anatase titania as support. The obtained catalyst was characterized by elemental analysis and N$_2$-adsorption-desorption method. The BET surface area is calculated as 188 m^{2}g^{-1}, comparable to that of CuO/*meso*-TiO$_2$. However, the pore volume of 0.268 cm^{3}g^{-1} is larger than that of CuO/*meso*-TiO$_2$. In particular the average pore diameter of 4.3 nm is significantly bigger than that of CuO/*meso*-TiO$_2$. Over CuO/*ana*-TiO$_2$ catalyst, the conversion of benzyl alcohol reaches 73.8%, and the selectivity to benzaldehyde, toluene and benzyl ether are 49.6%, 34.7% and 8.2%, respectively. The improved catalytic

activity is assumed mainly related to the larger pore volume and the bigger pore diameter compared to the CuO/*meso*-TiO$_2$ catalysts. Bigger pores reduce the degree of pore plugging by coke, and improve the diffusion of reactants and products through the catalyst particles.
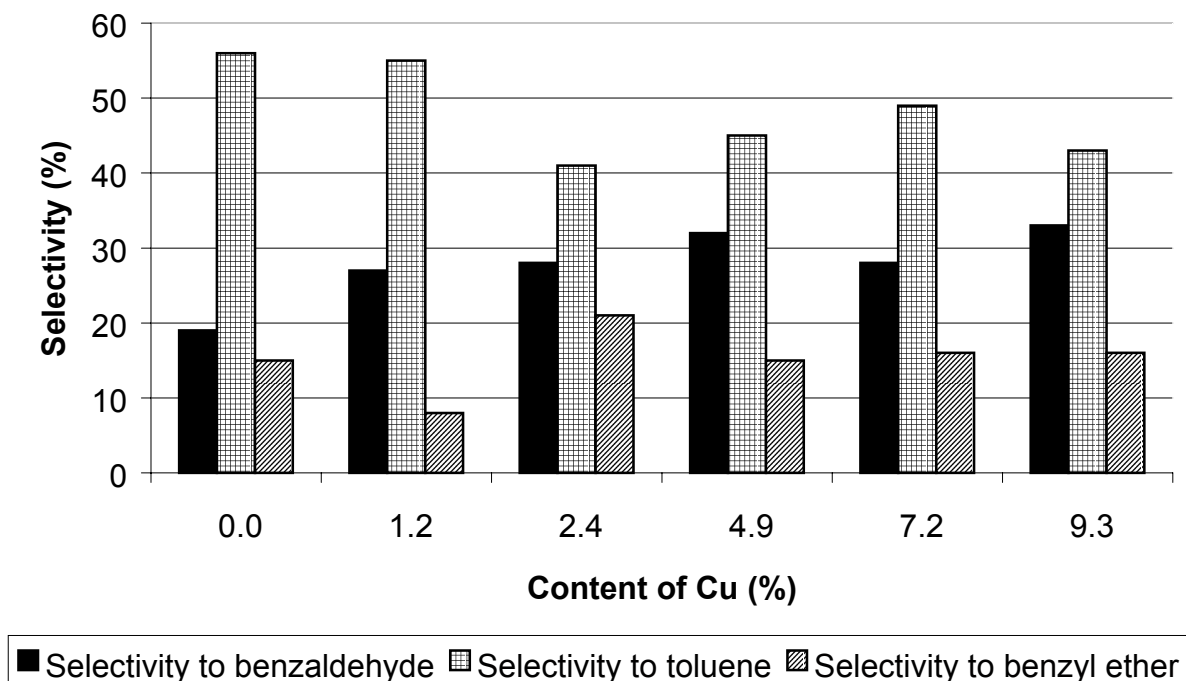
Figure 6.5 Selectivity of dehydrogenation of benzyl alcohol using pure mesoporous titania and CuO/*meso*-TiO$_2$ containing 1.2%, 2.4%, 4.9%, 7.2% and 9.3% of Cu as catalysts.

Table 6.3 Catalytic performances of CuO/*meso*-Al$_2$O$_3$ catalysts in the dehydrogenation of benzyl alcohol.

Cu wt.%	Conversion (%)	Selectivity (%)		
		benzaldehyde	toluene	benzyl ether
0	90.12	44.34	37.3	15.23
4.0	96.89	57.07	33.07	8.1
6.4	99.38	70.48	28.72	0.76
8.8	98.62	72.82	26.4	0.65

ZnO/*ana*-TiO$_2$ was also prepared and examined in catalytic dehydrogenation of benzyl alcohol, as a comparison to CuO/*ana*-TiO$_2$. In ZnO/*ana*-TiO$_2$ 8.1% of Zn was found by elemental analysis. N$_2$-adsorption-desorption study gives the BET surface area of 184 m^{2}g^{-1}, the pore volume of 0.263 cm^{3}g^{-1} and the average pore diameter of 4.3 nm. The structural data are very close to those in CuO/*ana*-TiO$_2$. The catalytic behavior is also similar. The conversion of benzyl alcohol reaches 76.9%, and the selectivity to benzaldehyde, toluene and benzyl ether are 42.8%, 21.4% and 30.7%, respectively.

As alumina was confirmed as a very active and useful catalyst and catalyst support,[14-18] we used mesoporous alumina as catalyst support instead of mesoporous titania.

Generally, acidic oxide catalysts accelerate reactions to form toluene and benzyl ether (Equation 6.2), whereas basic oxide catalysts accelerate dehydrogenation reaction (Equation 6.1). As summarized in Table 6.3, the selectivity to benzaldehyde over the pure mesoporous alumina is only 44%, although the conversion of benzyl alcohol reaches 90%. The selectivities to the byproducts toluene and benzyl ether are 37% and 15%, respectively. Grafting CuO on the mesoporous alumina surface increases basicity of the catalyst, so as to remarkably improve the selectivity to benzaldehyde. Moreover, the Cu content in the CuO/*meso*-Al$_2$O$_3$ catalysts has tremendous influence on the catalytic activity. The selectivity to benzaldehyde increases with the Cu content increasing in the investigated range between 4.0% and 8.8%. At the stage of 8.8% Cu, the selectivity to benzaldehyde reaches 73%, the selectivity to toluene is 26%, and only trace of benzyl ether is detected.

The catalytic behaviors of CuO/*meso*-Al$_2$O$_3$ (Cu wt.% = 6.4%) and ZnO/*meso*-Al$_2$O$_3$ (Zn wt.% = 7.7%) are distinguishable. CuO/*meso*-Al$_2$O$_3$ catalyst gives high conversion of benzyl alcohol up to 94% and high selectivity to benzaldehyde up to 76%. However, the selectivity to benzaldehyde over ZnO/*meso*-Al$_2$O$_3$ catalyst is only 18%, although the conversion of benzyl alcohol is up to 82%. A high selectivity over ZnO/*meso*-Al$_2$O$_3$ goes to benzyl ether, 72% is obtained. Thus, we assume that the CuO/*meso*-Al$_2$O$_3$ catalyst accelerates

dehydrogenation reaction (Equation 6.1), and the ZnO/*meso*-Al$_2$O$_3$ catalyst accelerates reactions towards toluene and benzyl ether (Equation 6.2).

Comparing the pore structural data between CuO/*meso*-Al$_2$O$_3$ catalysts and CuO/*meso*-TiO$_2$ catalysts (Table 6.1 and Table 6.2), CuO/*meso*-Al$_2$O$_3$ catalysts show their advantages in high BET surface area, high pore volume and large pore size. The major problem of CuO/*meso*-TiO$_2$ catalysts in coke formation and pore plugging is not remarkable when using CuO/*meso*-Al$_2$O$_3$ catalysts. No coke was observed in the catalysts after running the catalytic reaction for 1 h.

Catalytic dehydrogenation of cyclohexanol to cyclohexanone over Cu/Al$_2$O$_3$ catalysts was investigated by Chang et al.[6] The selectivity of cyclohexanone was impressively high up to 99%, however, the conversion of cyclohexanol was only 50%. The low conversion is probably due to the low BET surface area (130 m^{2}g^{-1}) and the relative small pore diameter (5.0 nm).

The catalytic activity in dehydrogenation of benzyl alcohol as a function of time on stream was examined, using CuO/*meso*-Al$_2$O$_3$ (Cu wt.% = 6.4%) catalyst as an example. As illustrated in Fig. 6.6, the conversion only slightly decreases with process time, from 99% in the first running hour to 90% in the tenth running hour. In the mean time, the selectivity to benzaldehyde decreases from 75% to 58%, the selectivity to the byproduct benzyl ether increases from 1% to 29%, and the selectivity to toluene was between 24% and 12%. The lifetime of the CuO/*meso*-Al$_2$O$_3$ catalyst is remarkably improved when compared to the reported Cu/SiO$_2$ catalysts, which showed sharp decreases in conversion and selectivity at early stages of time on stream.[5,9] Cu(II)-NaZSM-5 was investigated by Tsuruya in catalytic dehydrogenation of benzyl alcohol. Although both the conversion of benzyl alcohol and the selectivity to benzaldehyde were constant throughout process time of 5 h, the conversion and selectivity were below 50%.[2,4,7] The long lifetime of CuO/*meso*-Al$_2$O$_3$ catalyst is probably

attributed to a relatively high resistance to coke deposition on the mesoporous alumina surface.
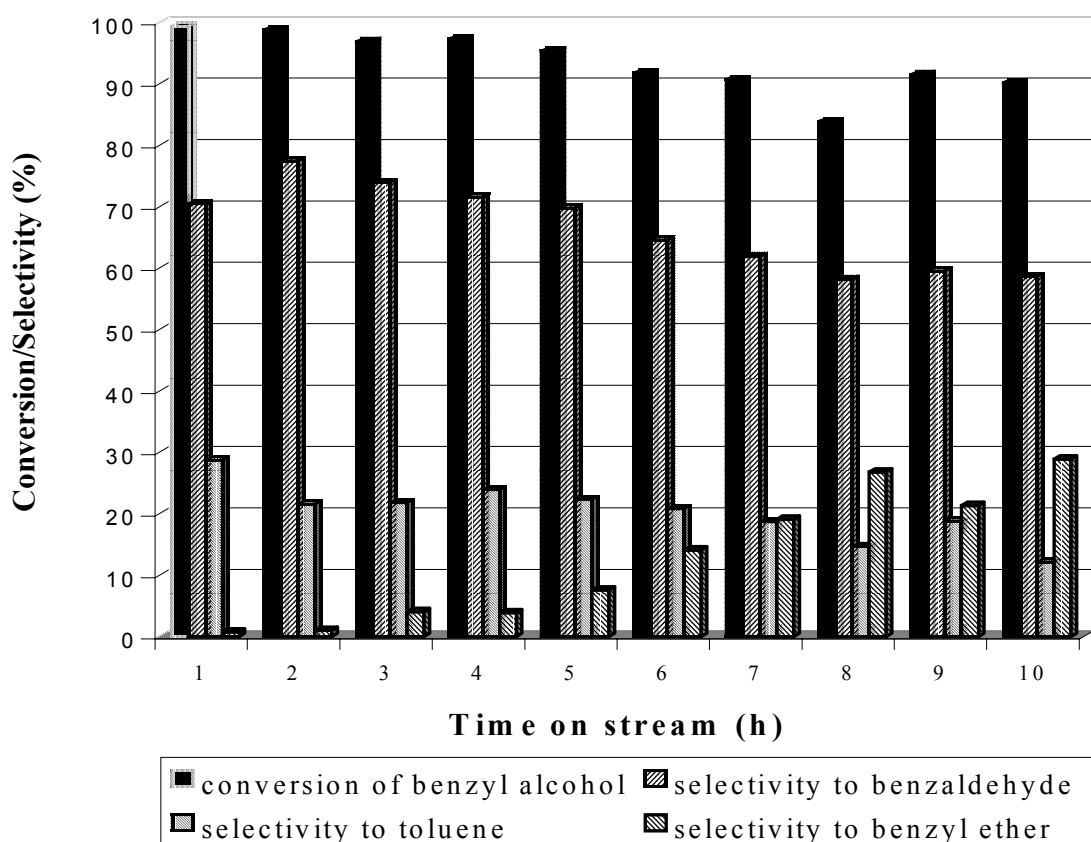
Figure 6.6 Conversion and selectivity *vs.* process time in the dehydrogenation of benzyl alcohol. Catalyst, ca. 1.6 g of CuO/*meso*-Al$_2$O$_3$ (Cu wt.% = 6.4%); benzyl alcohol flow rate, 5 ml h^{-1}; N$_2$ flow rate, 3.6 l h^{-1}; reaction temperature, 523 K.

For the CuO/*meso*-Al$_2$O$_3$ catalyst, we assume that alumina functions as an initial active species rather than CuO. The catalytic activity of mesoporous alumina in dehydrogenation of benzyl alcohol has been demonstrated (see above). The generated H$_2$ from the dehydrogenation reaction (Equation 6.1) reacts with CuO to produce metallic Cu that functions as a more active species in dehydrogenation than *meso*-Al$_2$O$_3$. That is probably the

reason why the selectivity to benzaldehyde is higher in the 2-4 running hours than in the first hour (Fig. 6.6). The existence of metallic Cu was confirmed by XRD (Fig. 6.8).
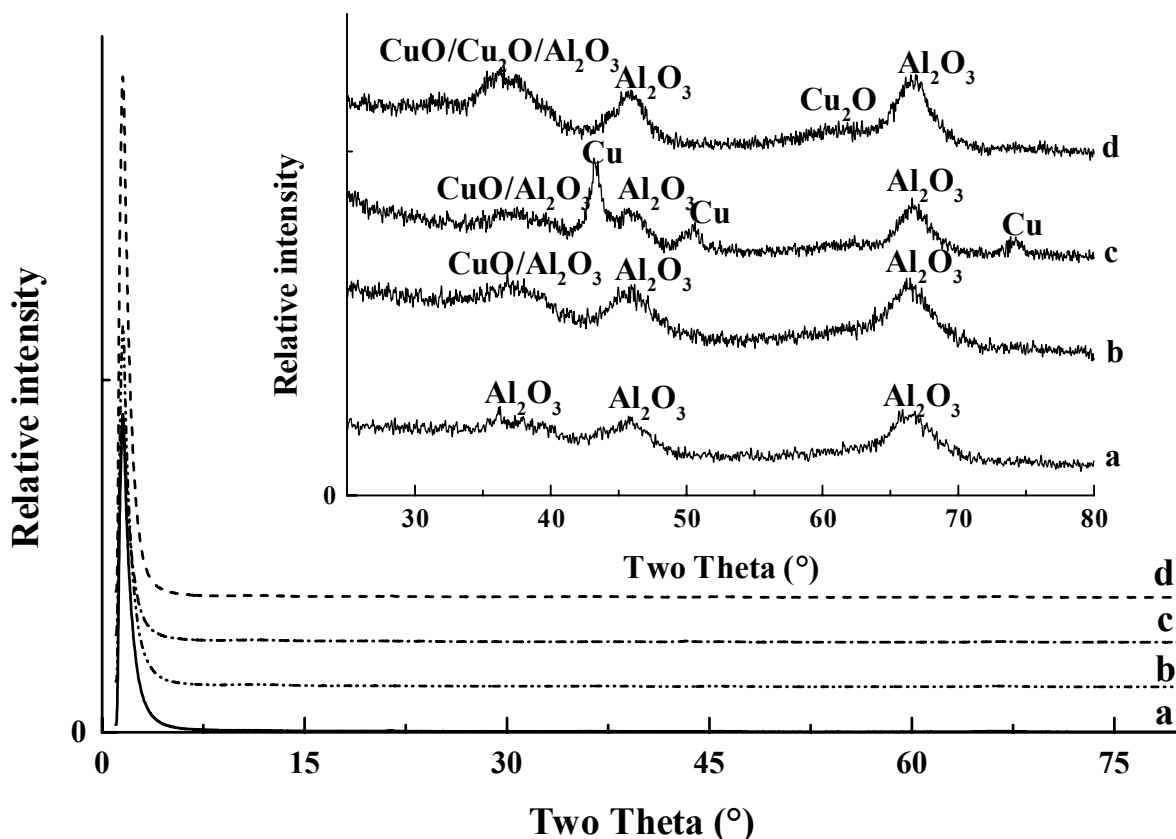
The decay of the CuO/*meso*-Al$_2$O$_3$ catalysts is considered being mainly caused by coke formation, suggested by the significant decrease of BET surface area and the black color of the used catalyst. After 10 h of catalysis running, the surface area of the CuO/*meso*-Al$_2$O$_3$ catalyst (Cu% = 6.4%) decreases from 353 m^{2}g^{-1} to 30 m^{2}g^{-1} (Fig. 6.7). Interestingly, it was observed that almost all the large pores (around 6.0 nm) were blocked but parts of the small pores (around 3.0 nm) were still visible. The XRD pattern of the used catalyst shows typical reflections of metallic Cu (Fig. 6.8c),[19] suggesting CuO is partially reduced to Cu during the catalytic dehydrogenation process. Taking into account that coke formation is mainly responsible for the deactivation of the catalyst, a very convenient and economical method was developed to effectively reactivate the catalyst: calcination at 400 °C for 2 h with sufficient air flow. Upon reactivation the metallic Cu is oxidized to CuO and Cu$_2$O, as evidenced by the XRD shown in Fig. 6.8d. The coke is burned away and the reactivated catalyst shows BET surface area of 311 m^{2}g^{-1} that is comparable to 353 m^{2}g^{-1} in the freshly prepared catalyst. The bimodal mesoporous structure appears again in the reactivated catalyst (Fig. 6.7c). The reactivated catalyst exhibits excellent catalytic activity, even better than the freshly prepared catalyst. In the first running hour over the reactivated catalyst, the conversion of benzyl alcohol reaches 98%, the selectivity to benzaldehyde is 80%, and the selectivities to toluene and benzyl ether are 16% and 4%, respectively.

It is interesting to note that the reactivated catalyst is more active than the freshly prepared catalyst. This is probably attributed to the generated Cu$_2$O through the process of reactivation. The existence of Cu$_2$O is evidenced by XRD (Fig. 6.8d). The fact that Cu$_2$O catalysts are more active than Cu catalysts was demonstrated by Fridman and Davydov in the dehydrogenation of cyclohexanol.[20]
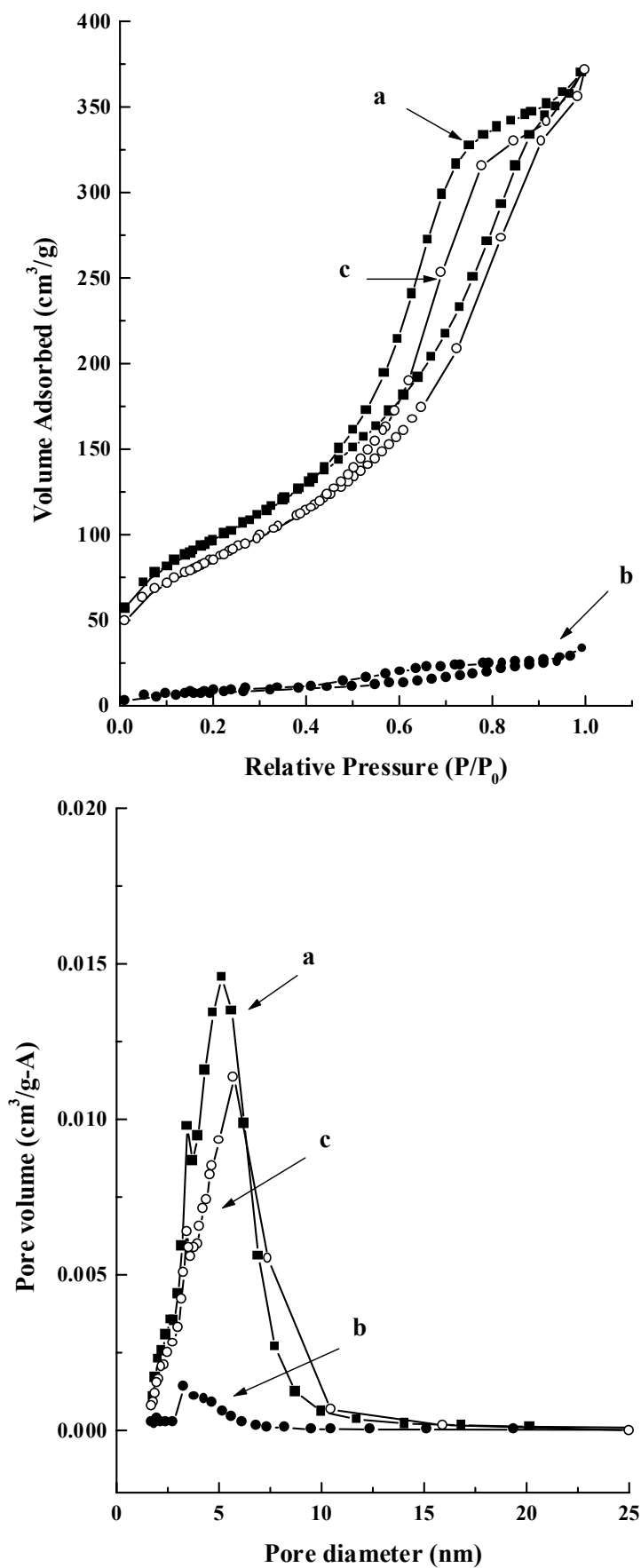
Figure 6.7 Isotherm plots and pore size distributions of CuO/*meso*-Al$_2$O$_3$ catalyst (Cu wt.% =

6.4%): (a) freshly prepared, (b) used for 10 h, and (c) reactivated.

Figure 6.8 XRD patterns of the pure mesoporous alumina (a) and the CuO/*meso*-Al$_2$O$_3$ catalyst (Cu wt.% = 6.4%) being freshly prepared (b), used for 4 h (c) and reactivated (d).

In conclusion, CuO/*meso*-Al$_2$O$_3$ catalyst shows improved catalytic activity and selectivity in the gas-phase catalytic dehydrogenation of benzyl alcohol to benzaldehyde. The general problem of coke formation that deactivates catalytic activity has been overcome by using mesoporous alumina as catalyst support. The feature of high surface area, high pore volume and large pore size of mesoporous alumina helps the diffusion of reactants and products through the catalyst, so as to increase the catalytic activity. There are distinct advantages in the Cu/meso Ai$_2$O$_3$ catalysts namely their straightforward preparation, high activity and high selectivity and are inexpensive. Moreover a further important feature is their long lifetime, together with the fact that the catalyst may be easily reactivated after use. All these features offer a promising potential for their application in the chemical industry.

References

1. R. A. Sheldon, J. K. Kochi, *Metal-catalyzed Oxidations of Organic Compounds*, Academic Press, New York, **1981**.

2. M. Nakao, S. Nishiyama, S. Tsuruya, M. Masai, *Inorg. Chem*. **1992**, *31*, 4662.

3. G. R. Dube, V. S. Darshane, *J. Chem. Soc., Faraday Trans.,* **1992**, *88*, 1299.

4. H. Hayashibara, S. Nishiyama, S. Suruya, M. Masai, *J. Catal.* **1995**, *153*, 254.

5. M. Arai, A. Nishiyama, S. Tsuruya, M. Masai, *J. Chem. Soc., Faraday Trans.,* **1996**, *92*, 2631.

6. H.-F. Chang, M. A. Saleque, W.-S. Hsu, W.-H. Lin, *J. Mol. Catal. A: Chem.* **1996**, *109*, 249.

7. M. Genta, S. Nishiyama, S. Tsuruya, M. Masai, *J. Chem. Soc., Faraday Trans.* **1996**, *92*, 1267.

8. H.-F. Chang, C-F. Yang, *Ind. Eng. Chem. Res.,* **1997**, *36*, 2080.

9. Y.-J. Tu, Y.-W. Chen, *Ind. Eng. Chem. Res*., **1998**, *37*, 2618.

10. W. Aquila, H. Fuchs, O. Worz, W. Ruppel, K. Halbritter, US patent 6013843, **2000**.

11. J. Wulff-Doring, J.-P. Melder, G. Schulz, G. Voit, G. Frank, W. Harder, US patent 6046359, **2000**.

12. K. Tanabe, M. Misono, Y. Ono, H. Hattori, *New Solid Acids and Bases, Their Catalytic Properties*, Kodansha Ltd.: Tokyo, **1989**, pp 317-322.

13. M. Hartmann, C. Bischof, *J. Phys. Chem. B*. **1999**, *103*, 6230.

14. P. T. Tanev, T. J. Pinnavaia, *Science,* **1995**, *267*, 865.

15. S. A. Bagshow, E. Prouzet, T. J. Pinnavaia, *Science,* **1995**, *269*, 1242.

16. S. A. Bagshow, T. J. Pinnavaia, *Angew. Chem. Int. Ed. Engl.* **1996**, *35*, 1102.

17. F. Vaudry, S. Khodabandeh, M. E. Davis, *Chem. Mater*. **1996**, *8*, 1451.

18. S. Cabrera, J. El Haskouri, J. Alamo, A. Beltrán, D. Beltrán, S. Mendioroz, M. Dolores Marcos, P. Amorós, *Adv. Mater*. **1999**, *11*, 379.

19. T. J. Richardson, J. L. Slack, M. D. Rubin, *the 4th International Meeting on Electrochromism*, **2000**, Uppsala, Sweden.

20. V. Z. Fridman and A. A. Davydov, *J. Catal*. **2000**, *195*, 20.

Chapter 7. Summary

In this thesis, the synthesis of mesoporous titanium oxide and its derivatives, mesoporous alumina, and porous zirconium oxide is described. Of these, mesoporous titania and alumina were examined as catalysts or catalyst supports in DeNO$_x$ and dehydrogenation of benzyl alcohol.

The mesoporous titanium oxide molecular sieves, namely titanium oxo-phosphate, "Na$_2$O" doped titania and pure titania, were synthesized by a ligand-assisted templating method. Titanium isopropoxide was used as metal center and 1-dodecylamine or 1-dodecanol as template. The strong covalent bonding between the metal center and the template head group provides a basis for the high-quality mesoporous materials. Surfactant was removed by a combination of acid/base washing and calcination.

The stabilization effect of the post-synthetic treatment with phosphoric acid/polyphosphoric acid has been demonstrated. As far as we know, it is the first example of using polyphosphoric acid to stabilize mesoporous structures. The rigid long chain of polyphosphoric acid may increase order degree of mesoporous structures thereby enhancing thermal stability. Post-synthetic treatment with phosphoric acid/polyphophoric acid and calcination produced mesoporous titanium oxo-phosphate molecular sieves that show a BET surface area as high as to 503 m^{2}g^{-1} and thermal stability of 626 °C.

Sodium hydroxide treatment of mesoporous titanium oxo-phosphate removes the phosphate group, and subsequent calcination produces "Na$_2$O" doped mesoporous titania. The material shows BET surface area greater than 300 m^{2}g^{-1} and thermal stability above 530 °C. Furthermore, the thermal stability can be tuned by the variation of sodium content: thermal stability increases with increasing of sodium content.

Treatment with aqueous HCl to the NaOH treated material opens a new approach to prepare thermally stable pure mesoporous titania. After calcination, the synthesized pure mesoporous titania shows a BET surface area of 461 m^2g^{-1} and thermal stability of 490 °C.

In general, the mesoporous titanium oxides reported in this thesis exhibit remarkably higher thermal stability than the reported analogues in the literature.

We attempted to extend this successful ligand-assisted templating methodology to the synthesis of mesoporous zirconium oxides. Porous zirconium oxo-phosphate (BET surface area of 336 m^2g^{-1} and average pore diameter of ca. 2.2 nm) and pure zirconium oxide (BET surface area of 242 m^2g^{-1} and average pore diameter of ca. 2.2 nm) were produced, although the pore sizes are between micro- and mesopores. The synthesis of a zirconium analogue of "Na_2O" doped mesoporous titania failed.

Unusual bimodal mesoporous alumina was prepared by a neutral surfactant templating method. The smaller pores are distributed at around 30 Å and the larger range from 60 to 200 Å in diameter. These materials are thermally stable up to 950 °C. The mesopore structure is influenced by template size, and reaction, aging and calcination temperatures, etc. The variation of template size only affects the structure of small pores, but not the size of large pores. High reaction temperature helps to increase the BET surface area and pore size. Low aging temperature benefits the pore structure and thermal stability. Higher calcination temperature enhances the condensation of the pore walls, however, much higher temperatures (over 750 °C) lead to pore structure partially or completely collapsing.

The high surface area and high thermal stabilitiy displayed by mesoporous titania and alumina are among the most important features with respect to the majority of possible catalytic applications. In an initial exploration of their applications, we examined their catalytic behaviour in $DeNO_x$ and dehydrogenation of benzyl alcohol.

Mesoporous alumina and titania indeed show promising advantages as a catalyst or a catalyst support in C_3H_8-SCR of NO_x. Mesoporous alumina catalyst (BET surface area ca. 400 m^2g^{-1}) was found to be more active than commercial alumina catalyst (200 m^2g^{-1}), especially at high temperature of 550 °C. Moreover, the conversion of NO_x to N_2 over a CuO grafted mesoporous alumina, namely CuO/*meso*-Al_2O_3 catalyst, is higher than over pure mesoporous Al_2O_3 at low temperatures in the range of 300 to 400 °C. Mesoporous titania catalyst (BET surface area ca. 300 m^2g^{-1}) also exhibits remarkably higher conversion of NO_x to N_2 at low temperatures in the range of 300 to 400 °C, in comparison to the non-mesoporous titania catalyst.

CuO/*meso*-Al_2O_3 catalyst shows excellent catalytic activity and selectivity in the gas-phase catalytic dehydrogenation of benzyl alcohol to benzaldehyde. The general problem of coke formation that deactivates catalytic activity has been overcome by using mesoporous alumina as catalyst support. The selectivity towards benzaldehyde over the pure mesoporous alumina is only 44%, although the conversion of benzyl alcohol reached 90%. Grafting CuO onto the mesoporous alumina surface remarkably improves the selectivity to benzaldehyde. Moreover, the selectivity to benzaldehyde increases with the Cu content increasing in the investigated range between 4.0% and 8.8%. At 8.8% Cu, the selectivity to benzaldehyde reaches 73%. The CuO/*meso*-Al_2O_3 catalysts show the high activity and high selectivity to benzaldehyde. Conversion of benzyl alcohol is high up to 90%, and selectivity to benzaldehyde is high up to 70%. Comparing to the CuO/non-*meso*-Al_2O_3 catalysts, a very important feature is their longer lifetime, together with the fact that the catalyst may be easily reactivated after deactivation.

Nevertheless, it should be noted that $DeNO_x$ and the dehydrogenation of benzyl alcohol are merely a few examples of the applications of mesoporous alumina and titania. The

potential of mesoporous materials in heterogeneous catalysis has been demonstrated, and the

research in this field will continue to grow.

Chapter 8. Experimental Part

8.1. General Techniques and Methods

Infrared Spectroscopy (IR)

The IR spectra were measured using KBr pellets in a Perkin Elmer FT-IR 1650 instrument. The vibrational frequencies are given in wavenumbers (cm^{-1}) and described as vs (very strong), s (strong), m (medium), w (weak), br (broad), sh (shoulder).

Nuclear Magnetic Resonance Spectroscopy (NMR)

The ^{1}H-NMR spectra were measured in a Bruker DPX 400 spectrometer. The solvent signal is used as internal standard. The chemical shifts are given in ppm and described as s (singlet), d (doublet), t (triplet), q (quartet), m (multiplet).

Thermal Analysis (TGA & DSC))

TGA was performed using a Perkin-Elmer TGA 7 Thermogravimetric Analyzer. Samples in 5 to 10 mg were heated in He from 50 to 600 ^{o}C with a heating rate of 10 ^{o}C min^{-1}.

DSC measurement was performed using a Netzsch DSC 404. Samples in 5 to 10 mg were heated in He from 50 to 1000 ^{o}C with a heating rate of 10 ^{o}C min^{-1}.

Elemental Analysis (EA)

Elemental analyses were performed in the microanalytical laboratory of our institute (director: Mr. Barth).

Powder X-ray Diffraction (XRD)

X-ray powder diffraction spectra were recorded on a Huber G600 diffractometer using Cu-K$_\alpha$ radiation (λ = 1.54 Å) and a scintillation detector. All the XRD spectra were compared with their backgrounds, in order to make sure that the reflections were not from the background. Fig. 8.1 presents an example.
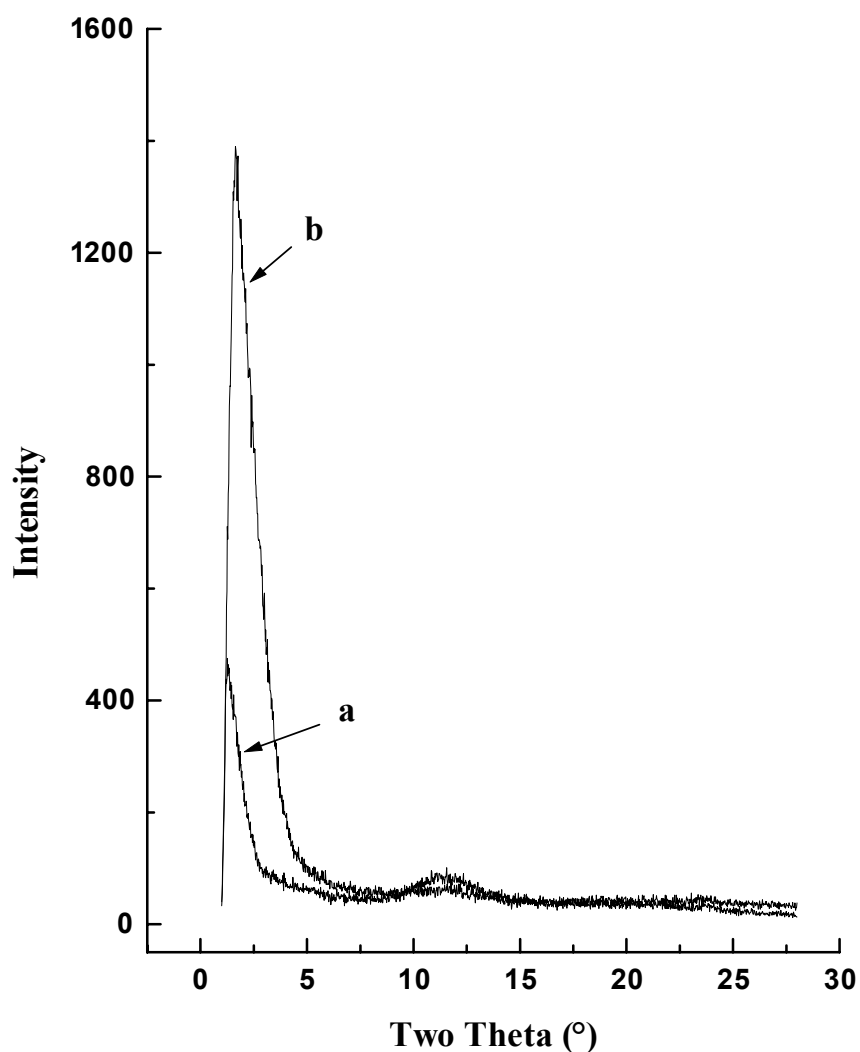
Figure 8.1 XRD patterns of mesoporous titanium oxo-phosphate (b) and the background (a).

Nitrogen Adsorption-Desorption Studies

Nitrogen adsorption-desorption isotherms were recorded on a Micrometritics ASAP 2000 adsorption analyzer. Samples were degassed at 250 °C at 10^{-3} torr before running.

The adsorption properties of molecular sieves materials give substantial information on the structure of these materials. The most fundamental property is the pore volume that is determined by testing the ability to absorb molecules of different radius size. Typical adsorbates are air, oxygen, water, nitrogen, carbon dioxide and a number of alkanes ranging from C_2 to C_7. In order to obtain the total pore volume, samples should be thermally dehydrated prior to measurement.

According to IUPAC the shapes of adsorption isotherms (Fig. 8.2) are classified into six groups.[1] Type I isotherm is given by a microporous solid, e.g. zeolites and activated carbon, having a relatively small external surface. Type II isotherm represents unrestricted monolayer-multilayer adsorption on a non-porous or macroporous adsorbent. Type VI represents stepwise multiplayer adsorption on a uniform non-porous surface, whereas type III and V are associated with weak adsorbent-adsorbent interactions. The characteristic features of the type IV isotherm are its hysteresis loop and the limiting uptake at high P/P_0. These features are associated with capillary condensation taking place in mesopores.[1,2]

The surface area, pore volume and pore size distribution are calculated using the experimental isotherm which has the volume of adsorbed gas plotted versus relative pressure. The BET (Brunauer, Emmett and Teller) procedure is used to calculate the surface area,[1] in which the following equation is used:

$$\frac{P}{n \times (P_0 - P)} = \frac{1}{n_m \times c} + \frac{c - 1}{n_m \times c} \times \frac{P}{P_0}$$

where n is the number of moles of adsorptive gas on 1 g of dehydrated adsorent (mol g^{-1}), n_m is the monolayer capacity (number of moles adsorbed as a monolayer on 1 g of adsorbent, mol g^{-1}), P/P_0 ratio is the relative pressure, P_0 is the saturation vapour pressure of adsorptive gas at
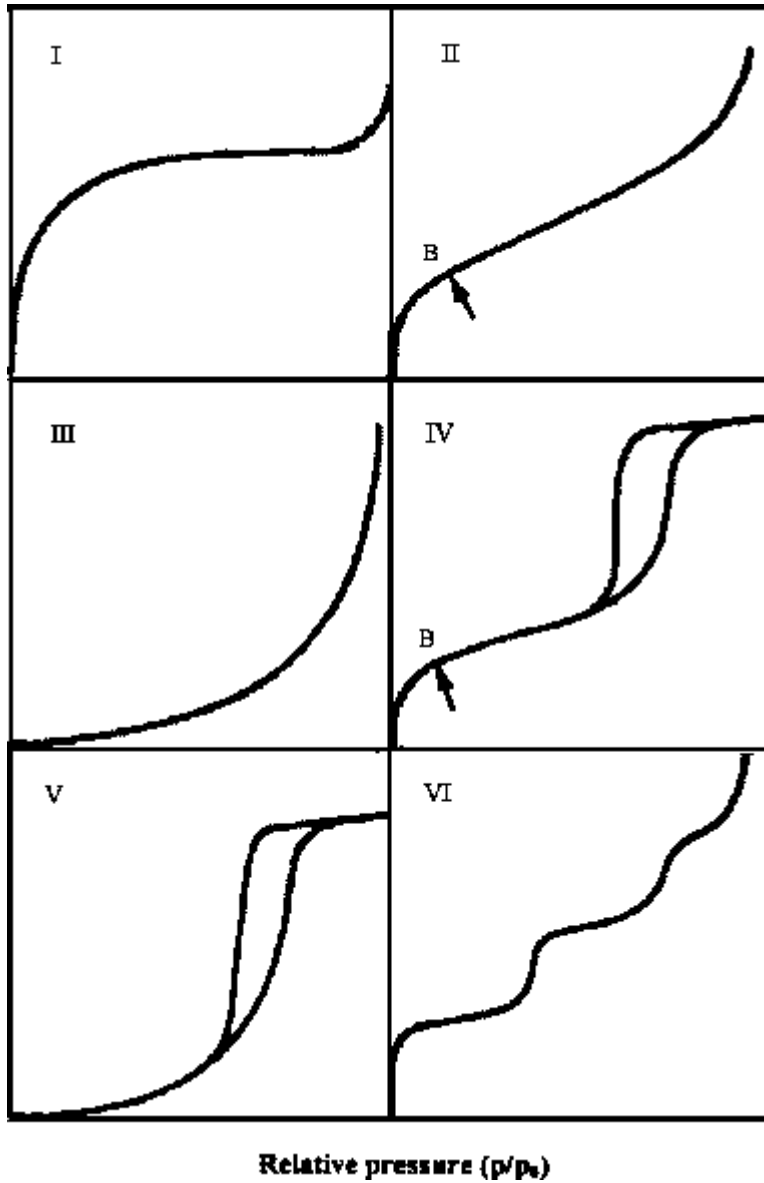
Figure 8.2 IUPAC shapes of adsorption isotherms.

adsorption temperature, c is the experimental constant retated to the net heat of adsorption of the molecules in the monolayer.

By plotting $P/n \times (P_0-P)$ versus P/P_0 it is possible to get n_m from the slope and intercept of the liner regression, and calculate the specific surface area (S_{BET}) using the following equation

$$S_{BET} = n_m \times N_0 \times a_m \qquad (m^2g^{-1})$$

where N_0 is the Avogadro constant (6.022×10^{23} mol^{-1}), a_m represents the area occupied by an adsorbate molecule in the completed monolayer (m^2).

The gas adsorption method of estimating the pore volume from the adsorption isotherm is based upon the fact that the gases condense to liquid in the narrow pores at pressures less than the saturation vapour pressure of the adsorbate. Assuming that all pores are filled with condensate at the highest relative pressure recorded, the total pore volume (V) can be calculated using the Gurvitsch equation:

$$V = n_{sat} \times V_M \qquad (cm^3 g^{-1})$$

where n_{sat} is the number of moles of adsorbate per gram of dehydrated adsorbent near satuation ($P \approx P_0$), V_M represents the molar volume of the adsorbate in the liquid phase (for N_2, V_M is 34.6 cm^{3}mol^{-1}).

8.2. Synthesis and Characterization of Mesoporous Materials and Catalysts

8.2.1. Mesoporous Titanium Oxide Materials

As-synthesized material using 1-dodecylamine as template

A mixture of titanium isopropoxide (Aldrich, 17.04 g, 60.0 mmol) and 1-dodecylamine (Merck, 11.12 g, 60.0 mmol) was stirred at room temperature until giving a homogeneous yellow solution (ca. 30 min.). By distillation off isopropanol the analytically pure compound $Ti(OC_3H_7)_3[HN(CH_2)_{11}CH_3]$ was obtained (equation 2.1).

EA   Calcd.: C 61.60, H 11.57, N 3.42, Ti 11.69% for $C_{21}H_{47}NO_3Ti$ (408.9).

                Found: C 61.59, H 12.29, N 3.10, Ti 10.27%.

^{1}H-NMR (CDCl$_3$, RT): δ 0.84 (t, 3H), 0.98 (s, 1H), 1.22 (t, 37H), 1.39 (m, 2H), 2.63 (t, 2H), 4.45 (m, 3H).

To the compound was added 150 ml of isopropanol and subsequently 150 ml of water, white precipitate formed immediately. After the mixture was aged at room temperature for 1 d and at 80 °C for 5 d, the as-synthesized material was collected by suction filtration, washed with water, ethanol and diethyl ether, and dried in an oven at 120 °C for 1 d.

EA Found: C 34.74, H 6.67, N 3.00%.

IR (KBr, cm^{-1}): 3415 (br), 2923 (vs), 2854 (s), 1631 (m), 1462 (m), 677 (s), 485 (s).

TGA 43.8% weight loss between 210 and 570 ^{o}C after desorption of water (Fig. 2.2a).

XRD A single broad reflection centered at d = 3.2 nm (Fig. 2.1a).

As-synthesized material using 1-dodecanol as template

A mixture of titanium isopropoxide (5.0 g, 17.6 mmol) and 1-dodecanol (Merck, 3.28 g, 17.6 mmol) was stirred at room temperature for ca. 30 min, leading to a homogeneous yellow solution. By distillation off isopropanol the analytically pure compound Ti(OC$_3$H$_7$)$_3$[O(CH$_2$)$_{11}$CH$_3$] was obtained (Equ. 2.2).

EA Calcd.: C 61.45, H 11.30, Ti 11.66% for C$_{21}$H$_{46}$O$_4$Ti (409.9).

Found: C 61.89, H 11.34, Ti 11.75%.

^{1}H-NMR (CDCl$_3$, RT): δ 4.49 (m, 3H), 4.20 (t, 2H), 1.60 (m, 2H), 1.26-1.20 (m, 36H), 0.84 (t, 3H).

The hydrolysis of this complex was carried out in an aqueous hydrochloric acid solution (pH = 0.5). The generated isopropanol was evaporated under vacuum. The mixture was aged at room temperature for two days, then, without purification, was used as precursor for the synthesis of mesoporous titanium oxo-phosphate.

Mesoporous titanium oxo-phosphate stabilized by phosphoric acid

2.5 g of the as-synthesized material, prepared from 1-dodecylamine, was added to a solution of 4.1 g of phosphoric acid in 120 ml of water and 120 ml of ethanol (pH ≈ 0.5). The mixture was stirred at room temperature for 2 h. The solid was collected by suction filtration, washed with water until a pH value of 7 was reached, and then washed with ethanol and diethyl ether, and dried in an oven at 120 °C for 2 h.

EA   Found: C 20.77, H 4.61, N 2.01%.

IR   (KBr, cm^{-1}): 3418 (br), 2961 (m), 2920 (s), 2850 (m), 1630 (m), 1468 (m),
1024 (vs), 512 (s).

TGA   A weight loss of 29.7% between 50 and 600 °C (Fig. 2.2b).

XRD   A broad reflection centered at d = 3.6 nm (Fig. 2.1b).

The retained surfactant was removed by calcination at 400 °C for 6 h, leading to a mesoporous titanium oxo-phosphate.

EA   Found: C 0.42, H 1.11, N 0.14, P 14.1, Ti 36.3%.

IR   (KBr, cm^{-1}): 3405 (br), 1624 (m), 1044 (vs), 784 (m), 615 (m), 461 (m).

TGA   No obvious weight loss in the temperature range of 50 to 600 $^{\circ}$C
(Fig. 2.2c).

DSC An exothermal peak at 594 °C (Fig. 2.6c).

XRD A single reflection centered at d = 5.4 nm (Fig. 2.1c).

N₂-Adsorption The BET surface area is 368 m^2g^{-1} determined by BJH desorption curve,

-Desorption the pore volume is 0.186 cm^3g^{-1}, the average pore diameter is 2.0 nm

(Fig. 2.3).

Mesoporous titanium oxo-phosphate stabilized by polyphosphoric acid

1.0 g of the as-synthesized material, prepared from 1-dodecanol, was treated with 2.0 g of polyphosphoric acid in 50 ml of water (pH ≈ 0.5) for 2 h. The solid was collected by suction filtration, washed with water until a pH of 7 was reached, and then washed with ethanol and diethyl ether, and dried in an oven at 120 °C overnight. Calcination at 450 °C in a stream of air for 4 h yielded a mesoporous titanium oxo phosphate.

EA Found: C 0.1, H 1.69, P 12.29%.

IR (KBr, cm^{-1}): 1048 (s).

TGA No weight loss is identified above 200 °C.

DSC Two sharp exothermic peaks at 626 °C and 787 ° (Fig. 2.6d).

XRD A single reflection centered at d = 5.6 nm (Fig. 2.5b).

N₂-Adsorption The BET surface area is 503 m^2g^{-1}, the pore volume is 0.357 cm^3g^{-1},

-Desorption and the average pore diameter is 2.7 nm determined by the desorption

branch of BJH curve (Fig. 2.4).

"Na₂O" doped mesoporous titanium oxide

The as-synthesized material using 1-docecylamine as template was used as the precursor to prepare "Na₂O" doped mesoporous titanium oxide. After post-synthetic treatment

with phosphoric acid/polyphosphoric acid, 2.2 g of the sample was treated with 100 ml of aqueous sodium hydroxide solution (10%) overnight. Then the solid was collected by suction filtration. Exhaustively washing with water removed all phosphate and partial surfactants. In the IR spectra no P-O vibrations were identified. It was nevertheless found that sodium was introduced into the material even when exhaustive washing with water until a pH of 7 was reached.

Calcination at 350 °C for 8 h removed remaining surfactants completely, and a "sodium oxide" doped mesoporous titania was produced. The TGA curves of the calcined samples only show desorption of physiadsorbed water.

The Na content in the material can be tuned by controlling the pH value of the water filtrate. The materials with various sodium contents, namely 4.9%, 5.5% and 7.1%, were obtained.

"Na$_2$O" doped mesoporous titanium oxide containing 4.9% of Na

EA   Found: C 0.27, H 0.86, N 0.05, Na 4.9, P 0.06, Ti 47.0%.

DSC   An exothermal peak at 530 ^{o}C (Fig. 2.10b).

XRD   A single reflection centered at d = 5.7 nm.

N$_2$-Adsorption   The BET surface area is 334 m^{2}g^{-1}, the pore volume is 0.301 cm^{3}g^{-1},

-Desorption   the pore size distribution is narrow and the average pore diameter is

3.2 nm determined according to the desorption branch of BJH.

"Na$_2$O" doped mesoporous titanium oxide containing 5.5% of Na

EA   Found: C 0.24, H 0.23, N 0.06, Na 5.52, P 0.08, Ti 52.24%.

DSC   An exothermal peak at 550 ^{o}C (Fig. 2.10c).

XRD   A single reflection centered at d = 5.7 nm (Fig. 2.7d)

N$_2$-Adsorption   The BET surface area is 390 m^{2}g^{-1}, the pore volume is 0.301 cm^{3}g^{-1},

-Desorption   the pore size distribution is narrow and the average pore diameter is

3.0 nm determined according to the desorption branch of BJH (Fig. 2.8).

"Na$_2$O" doped mesoporous titanium oxide containing 7.1% of Na

EA   Found: C 0.43, H 0.73, N 0.0, Na 7.1, P 0.02, Ti 48.8%.

DSC   An exothermal peak at 575 ^{o}C (Fig. 2.10d).

XRD   A single reflection centered at d = 5.7 nm.

N$_2$-Adsorption   The BET surface area is 301 m^{2}g^{-1}, the pore volume is 0.265 cm^{3}g^{-1},

-Desorption   the pore size distribution is narrow and the average pore diameter is

3.3 nm determined according to the desorption branch of BJH.

Pure mesoporous titanium oxide

Route 1:

0.5 g of the as-synthesized material, prepared from Ti(O^{i}Pr)$_4$ and 1-dodecylamine, was added to a solution of 100 ml of 5 M NaOH and 100 ml of ethanol. The mixture was stirred overnight at room temperature. The solid was collected and washed with water exhaustively until pH = 7, dried in an over at 120 °C for 2 h. The pale-yellow coloured "Na$_2$O" doped mesoporous titania was obtained.

EA   Found: C 1.59, H 1.81, N 0.1, Na 5.2%.

XRD   A single reflection centered at d = 5.7 nm.

N$_2$-Adsorption   The BET surface area is 354 m^{2}g^{-1}, the pore volume is 0.194 cm^3/g

-Desorption   and the average pore diameter is 2.5 nm obtained from BJH desorption

branch (Fig. 2.12a and Fig. 2.13a).

160 mg of the "Na$_2$O" doped mesoporous titania described above was added to a solution of 50 ml of aqueous HCl (1%) and 50 ml of ethanol. The mixture was stirred at room temperature for 2 h. The solid was filtered off and washed with water until a pH of 7 was reached and no more Cl$^-$ detected, and then dried in an over at 120 °C for 2 h.

N$_2$-Adsorption   The BET surface area is 418 m^{2}g^{-1}, the pore volume is 0.300 cm^{3}g^{-1}, and

-Desorption   the average pore diameter is 2.8 nm obtained from BJH desorption branch.

The above sample was calcined at 350 °C for 8 h, the pure mesoporous titania was obtained.

EA   Found: C 0.06, H 1.03, Cl 0.01, N 0.00, Na 0.1, Ti 51.42%.

DSC   An exothermal peak at 490 °C (Fig. 2.6a).

XRD   A single reflection centered at d = 5.66 nm.

N$_2$-Adsorption   The BET surface area is 342 m^{2}g^{-1}, the pore volume is 0.241 cm^{3}g^{-1} and

-Desorption   the average pore diameter is 2.9 nm obtained from BJH desorption branch

(Fig. 2.12b and Fig. 2.13b).

Route 2:

2.5 g of the as-synthesized material, prepared from 1-dodecylamine, was added to a solution of 4.1 g of phosphoric acid in 120 ml of water and 120 ml of ethanol (pH ≈ 0.5). The

mixture was stirred at room temperature for 2 h. The solid was collected by suction filtration, washed with water until a pH value of 7 was reached, and then washed with ethanol and diethyl ether, and dried in an oven at 120 °C for 2 h.

2.2 g of the above product was treated with 100 ml of 10% NaOH overnight at room temperature. The solid was filtered off and washed with water until a pH value of 7 was reached, and then washed with ethanol and diethyl ether, and dried in an oven at 120 °C for 2 h.

EA	Found: C 13.19, H 3.40, N 0.94, Na 4.0, P 0.06, Ti 40.06%.
TGA	A weight loss of 17% between 50 and 600 °C.
XRD	A single reflection centered at d = 5.7 nm.
N_2-Adsorption	The BET-surface area is 587 m^2g^{-1}, the pore volume is 0.509 cm^3g^{-1}, and
-Desorption	the average pore diameter is 3.4 nm obtained from BJH desorption branch.

Pure mesoporous titania was then obtained by calcination at 350 °C for 8 h.

EA	Found: C 0.15, H 0.66, Cl <0.1, N 0, Na 0.1, P 0.02%.
TGA	Only a weight loss of ca. 4% below 200 °C (Fig.2.14d).
DSC	An exothermal peak at 490 °C (Fig. 2.6).
XRD	A single reflection centered at d = 5.7 nm (Fig. 2.15d).
N_2-Adsorption	The BET surface area is 461 m^2g^{-1}, the pore volume is 0.459 cm^3g^{-1} and
-Desorption	the pore diameter is 3.45 nm obtained from BJH desorption branch (Fig. 2.16).

8.2.2. Mesoporous Zirconium Oxide Materials

As-synthesized mesoporous zirconia

Zirconium ethoxide (Aldrich, 1.36 g, 5.0 mmol) and 1-dodecylamine (Merck, 0.93 g, 5.0 mmol) was added to 50 ml of ethanol. The mixture was stirred at 50 °C until a homogeneous solution was obtained. By distillation off isopropanol at 50 °C under reduced pressure, the analytically pure compound $Zr(OC_2H_5)_3[HN(CH_2)_{11}CH_3]$ was obtained (Equ. 3.1).

^{1}H NMR   (CDCl$_3$, RT): δ 0.84 (t, 3H), 1.16-1.24 (m, 26H), 1.40 (m, 2H),

2.65 (t, 2H), 3.97-4.08 (m, 6H).

To the complex $Zr(OCH_2CH_3)_3[HN(CH_2)_{11}CH_3]$ was added 25 ml of ethanol and subsequently 25 ml of water. After being stirred at room temperature for 1 h, the mixture was aged at room temperature for 1 d and at 70 °C for 5 d. The solid was collected, washed with water, ethanol and diethyl ether, and dried at 120 °C overnight.

TGA   A 15% weight loss below 120 °C and a 15-18% weight loss between 120

and 600 °C (Fig. 3.1a).

XRD   A single reflection centered at d = 5.4 nm (Fig. 3.2a).

N$_2$-Adsorption   The BET surface area is 711 m^2g^{-1}, the pore volume is 0.459 cm^3g^{-1} and

-Desorption   the pore diameter is 2.4 nm obtained from BJH desorption branch

(Fig. 3.3a).

Mesoporous zirconium oxo-phosphate

1.50 g of the as-synthesized material was added to a solution of 3.0 g phosphoric acid in 80 ml of water and 80 ml of ethanol (pH = 0.5). The mixture was stirred at room temperature for 3 h. The solid was collected by suction filtration, washed with water until a pH value of 7 was reached, and then washed with ethanol and diethyl ether, and dried in an oven at 120 °C for 2 h. After calcination at 400 °C for 1 h, the mesoporous zirconium oxo-phosphate was obtained.

EA	Found: C 0.10, H 0.89, N 0.0%.
IR	(KBr, cm-1): 1030 (s).
XRD	A single reflection centered at d = 5.6 nm (Fig. 3.2b).
N$_2$-Adsorption	The BET surface area is 336 m^{2}g^{-1}, the pore volume is 0.206 cm^{3}g^{-1}, and
-Desorption	the average pore diameter is ca. 2.2 nm calculated from the pore size distribution based on the BJH desorption branch (Fig. 3.3b).

Pure mesoporous zirconium oxide

Route 1:

Calcination of the as-synthesized material at 400 °C for 1 h gave pure mesoporous zirconium oxide.

EA	Found: C 0.24, H 0.80, N < 0.01%.
XRD	A single reflection centered at d = 5.5 nm (Fig. 3.2c).

N₂-Adsorption   The BET surface area is 228 m^2g^{-1}, the pore volume is 0.138 cm^3g^{-1}, and

-Desorption   the average pore diameter is ca. 2.2 nm obtained from the pore size

    distribution based on the BJH desorption branch (Fig. 3.3c).

Route 2:

The sample of mesoporous zirconium oxo-phosphate before calcination was used to prepare pure mesoporous zirconium oxide. 0.46 g of the sample was treated with a solution of 20 ml of 10% NaOH and 20 ml of ethanol overnight at room temperature. The solid was filtered off and washed with water until a pH value of 7 was reached, and then washed with ethanol and diethyl ether, and dried in an oven at 120 °C for 2 h. The obtained solid was added to a solution of 20 ml of 1% aqueous HCl and 20 ml of ethanol. After stirring at room temperature for 2 h, the solid was collected and washed with water until a pH value of 7 was reached and no Cl^- was detected, and then washed with ethanol and diethyl ether, and dried in an oven at 120 °C for 2 h.

XRD   A single reflection centered at d = 5.6 nm.

N₂-Adsorption   The BET surface area is 526 m^2g^{-1}, the pore volume is 0.24 cm^3g^{-1}, and

-Desorption   the average pore diameter is ca. 2.3 nm obtained from the pore size

    distribution based on the BJH desorption branch.

The above sample was subsequently calcined at 350 °C for 2 h, the pure mesoporous zirconium oxide was obtained.

EA   Found: C 0.82, H 1.16, N 0.0%.

XRD   A single reflection centered at d = 5.6 nm.

N$_2$-Adsorption   The BET surface area is 242 m^{2}g^{-1}, the pore volume is 0.140 cm^{3}g^{-1}, and

-Desorption   the average pore diameter is ca. 2.2 nm obtained from the pore size

distribution based on the BJH desorption branch.

8.2.3. Bimodal Mesoporous Alumina

As-synthesized mesoporous alumina

A mixture of aluminium isopropoxide (Aldrich, 10.21 g, 50 mmol) and 1-dodecylamine (Merck, 9.26 g, 50 mmol) was stirred at 80 °C for 3 h, leading to the formation of adduct Al(OC$_3$H$_7$)$_3$[NH$_2$(CH$_2$)$_{11}$CH$_3$] (Equatiom 4.1).

^{1}H-NMR   (CDCl$_3$, RT): δ 0.83 (t, 3H), 1.13-1.22 (m, 36H), 1.39 (m, 2H),

2.64 (t, 2H), 4.43 (m, 3H) ppm.

At 80 °C, 100 ml of isopropoxide at 80 °C was added to the adduct, subsequently 100 ml of water at 80 °C was added slowly. The mixture was stirred at 80 °C for 2 h, and then aged at room temperature for 5 d. The solid was collected and washed exhaustively with water, and then washed with ethanol and diethyl ether, and dried in an oven at 120 °C for 2 h. The as-synthesized mesoporous alumina was obtained.

EA   Found: C 5.44, H 3.50, N 0.31%.

TGA   An 8-10% weight loss below 120 °C and a 20-25% weight loss between

120 and 700 °C (Fig. 4.1a).

XRD   A single reflection centered at d = 5.6 nm (Fig. 4.2a).

N$_2$-Adsorption   The BET surface area is 335 m^{2}g^{-1}, the pore volume is 0.733 cm^{3}g^{-1}, and

-Desorption   the average pore diameter is ca. 5.9 nm obtained from the pore size

distribution based on the BJH desorption branch (Fig. 4.3a).

Bimodal mesoporous alumina

The bimodal mesoporous alumina was obtained by calcinations of the as-synthesized

material at 450 °C for 6 h.

EA   Found: C 0.14, H 1.33, N 0.0%.

TGA   A 6% weight loss between 50 and 700 °C (Fig. 4.1b).

XRD   A single reflection centered at d = 5.7 nm (Fig. 4.2b).

N$_2$-Adsorption   The BET surface area is 449 m^{2}g^{-1}, the pore volume is 0.989 cm^{3}g^{-1}, and

-Desorption   the average pore diameter is ca. 6.9 nm obtained from the pore size

distribution based on the BJH desorption branch (Fig. 4.3b).

8.2.4. Bimodal Mesoporous Alumina Supported Catalysts

Pure mesoporous alumina catalyst

The pure mesoporous alumina powder was compressed into disks in a steel die of 10

mm diameter by applying a pressure of 500 N/mm^2, and the disks were crushed and sieved

into pellets with diameters between 0.2 to 0.3 mm. This mechanical treatment procedure was

applied to all the catalysts reported in this thesis.

N$_2$-Adsorption   Before mechanical treatment:

-Desorption   The BET surface area is 414 m^{2}g^{-1}, the pore volume is 0.951 cm^{3}g^{-1}, and

the average pore diameter is ca. 6.9 nm obtained from the pore size

distribution based on the BJH desorption branch (Fig. 5.1a).

After mechanical treatment:

The BET surface area is 412 m^{2}g^{-1}, the pore volume is 0.654 cm^{3}g^{-1}, and

the average pore diameter is ca. 5.1 nm obtained from the pore size

distribution based on the BJH desorption branch (Fig. 5.1b).

CuO/*meso*-Al$_2$O$_3$ catalysts

5.0 g of mesoporous alumina was suspended in 200 ml aqueous solution of

CuCl$_2$·2H$_2$O (1.5 g). 5.0 g of aqueous NH$_3$·H$_2$O (25%) was added drop by drop. After stirring

at room temperature for 1 h, the solid was filtered off, washed with water until no Cl$^-$ was

detected, dried at 120 °C for 3 h, and calcined at 400 °C for 2 h. The CuO/*meso*-Al$_2$O$_3$

catalyst containing 6.4% of Cu was obtained.

By the similar method, using 0.61 g of CuCl$_2$·2H$_2$O and 1.0 g of NH$_3$·H$_2$O (25%) gave

CuO/*meso*-Al$_2$O$_3$ with Cu loading of 4.0%, and 1.5 g of CuCl$_2$·2H$_2$O and 2.5 g of NH$_3$·H$_2$O

(25%) gave CuO/*meso*-Al$_2$O$_3$ with Cu loading of 8.8%.

CuO/*meso*-Al$_2$O$_3$ catalyst containing 4.0% of Cu (after mechanical treatment)

EA   Found: C 0.51, H 1.73, Al 42.0, Cl 0.0, Cu 4.0, N 0.0%.

N$_2$-Adsorption   The BET surface area is 365 m^{2}g^{-1}, the pore volume is 0.591 cm^{3}g^{-1} and

-Desorption   the average pore diameter is 5.1 nm obtained from the pore size

distribution based on the BJH desorption branch (Fig. 6.1b).

CuO/*meso*-Al₂O₃ catalyst containing 6.4% of Cu

EA	Found: C 0.30, H 1.61, Al 40.6, Cl <0.05, Cu 6.4, N, 0.0%.

N₂-Adsorption   Before mechanical treatment:

-Desorption   The BET surface area is 403 m^2g^{-1}, the pore volume is 0.731 cm^3g^{-1} and the average pore diameter is 5.7 nm obtained from the pore size distribution based on the BJH desorption branch.

After mechanical treatment:

The BET surface area is 353 m^2g^{-1}, the pore volume is 0.559 cm^3g^{-1} and the average pore diameter is 5.0 nm obtained from the pore size distribution based on the BJH desorption branch (Fig. 6.1c).

CuO/*meso*-Al₂O₃ catalyst containing 8.8% of Cu (after mechanical treatment)

EA   Found: C 0.43, H 1.33, Al 39.9, Cl 0.10, Cu 8.8, N, 0.0%.

N₂-Adsorption   The BET surface area is 355 m^2g^{-1}, the pore volume is 0.585 cm^3g^{-1} and

-Desorption   the average pore diameter is 5.2 nm obtained from the pore size distribution based on the BJH desorption branch (Fig. 6.1d).

ZnO/*meso*-Al₂O₃ catalyst

5.0 g of mesoporous alumina was suspended in 200 ml aqueous solution of $ZnCl_2$ (1.2 g). 4.9 g of aqueous $NH_3 \cdot H_2O$ (25%) was added drop by drop. After stirring at room temperature for 1 h, the solid was filtered off, washed with water until no Cl⁻ was detected, dried at 120 °C for 3 h, and calcined at 400 °C for 2 h. The ZnO/*meso*-Al₂O₃ catalyst containing 7.7% of Zn was obtained.

EA   Found: C 0.38, H 1.68, Al 39.1, Cl 0.05, N, 0.0, Zn 7.7%.

N$_2$-Adsorption   Before mechanical treatment:

-Desorption   The BET surface area is 395 m^{2}g^{-1}, the pore volume is 0.739 cm^{3}g^{-1} and

the average pore diameter is 6.0 nm obtained from the pore size

distribution based on the BJH desorption branch (Fig. 5.4a).

After mechanical treatment:

The BET surface area is 263 m^{2}g^{-1}, the pore volume is 0.425 cm^{3}g^{-1} and

the average pore diameter is 5.1 nm obtained from the pore size

distribution based on the BJH desorption branch (Fig. 5.4b).

8.2.5. Mesoporous Titania Supported Catalysts

Pure mesoporous titania catalyst

N$_2$-Adsorption   Before mechanical treatment:

-Desorption   The BET surface area is 230 m^{2}g^{-1}, the pore volume is 0.282 cm^{3}g^{-1} and

the average pore diameter is 3.8 nm obtained from the pore size

distribution based on the BJH desorption branch (Fig. 6.3a).

After mechanical treatment:

The BET surface area is 300 m^{2}g^{-1}, the pore volume is 0.298 cm^{3}g^{-1} and

the average pore diameter is 3.9 nm obtained from the pore size

distribution based on the BJH desorption branch (Fig. 6.4a).

CuO/*meso*-TiO$_2$ catalysts

5.7 g of pure mesoporous titania before calcination was suspended in 200 ml ethanol

solution of CuCl$_2$·2H$_2$O (1.3 g). 3.3 g of aqueous NH$_3$·H$_2$O (25%) was added drop by drop.

After stirring at room temperature for 1 h, the solid was filtered off, washed with water until no Cl$^-$ was detected, dried at 120 °C for 3 h, and calcined at 400 °C for 1 h. The CuO/*meso*-TiO$_2$ catalyst containing 9.3% of Cu was obtained.

By the similar method, using 0.13 g of CuCl$_2$·2H$_2$O and 0.20 g of NH$_3$·H$_2$O (25%) gave CuO/*meso*-Al$_2$O$_3$ with Cu loading of 1.2%, 0.33 g of CuCl$_2$·2H$_2$O and 0.51 g of NH$_3$·H$_2$O (25%) gave Cu loading of 2.4%, 0.62 g of CuCl$_2$·2H$_2$O and 1.54 g of NH$_3$·H$_2$O (25%) gave Cu loading of 4.1%, and 1.0 g of CuCl$_2$·2H$_2$O and 1.5 g of NH$_3$·H$_2$O (25%) gave Cu loading of 7.2%.

CuO/*meso*-TiO$_2$ catalyst containing 1.2% of Cu

EA　　　　　　　Found: C 0.10, H 0.77, Cl 0.10, Cu 1.2, N, 0.0, Ti 53.1%.

N$_2$-Adsorption　　Before mechanical treatment:

-Desorption　　　The BET surface area is 258 m^{2}g^{-1}, the pore volume is 0.295 cm^{3}g^{-1} and the average pore diameter is 3.5 nm obtained from the pore size distribution based on the BJH desorption branch (Fig. 6.3b).

After mechanical treatment:

The BET surface area is 254 m^{2}g^{-1}, the pore volume is 0.259 cm^{3}g^{-1} and the average pore diameter is 3.3 nm obtained from the pore size distribution based on the BJH desorption branch (Fig. 6.4b).

CuO/*meso*-TiO$_2$ catalyst containing 2.4% of Cu

EA　　　　　　　Found: C 0.10, H 0.73, Cl 0.10, Cu 2.4, N, 0.0, Ti 52.4%.

N$_2$-Adsorption Before mechanical treatment:

-Desorption The BET surface area is 258 m^{2}g^{-1}, the pore volume is 0.291 cm^{3}g^{-1} and the average pore diameter is 3.4 nm obtained from the pore size distribution based on the BJH desorption branch (Fig. 6.3c).

After mechanical treatment:

The BET surface area is 221 m^{2}g^{-1}, the pore volume is 0.241 cm^{3}g^{-1} and the average pore diameter is 3.5 nm obtained from the pore size distribution based on the BJH desorption branch (Fig. 6.4c).

CuO/*meso*-TiO$_2$ catalyst containing 4.9% of Cu

EA Found: C 0.10, H 0.51, Cl 0.0, Cu 4.9, N, 0.0, Ti 52.8%.

N$_2$-Adsorption Before mechanical treatment:

-Desorption The BET surface area is 211 m^{2}g^{-1}, the pore volume is 0.257 cm^{3}g^{-1} and the average pore diameter is 3.6 nm obtained from the pore size distribution based on the BJH desorption branch (Fig. 6.3d).

After mechanical treatment:

The BET surface area is 209 m^{2}g^{-1}, the pore volume is 0.222 cm^{3}g^{-1} and the average pore diameter is 3.4 nm obtained from the pore size distribution based on the BJH desorption branch (Fig. 6.4d).

CuO/*meso*-TiO$_2$ catalyst containing 7.2% of Cu

EA Found: C 0.10, H 0.62, Cl 0.05, Cu 7.2, N, 0.01, Ti 49.0%.

N$_2$-Adsorption   Before mechanical treatment:

-Desorption   The BET surface area is 176 m^{2}g^{-1}, the pore volume is 0.233 cm^{3}g^{-1} and the average pore diameter is 3.9 nm obtained from the pore size distribution based on the BJH desorption branch (Fig. 6.3e).

After mechanical treatment:

The BET surface area is 198 m^{2}g^{-1}, the pore volume is 0.236 cm^{3}g^{-1} and the average pore diameter is 3.7 nm obtained from the pore size distribution based on the BJH desorption branch (Fig. 6.4e).

CuO/*meso*-TiO$_2$ catalyst containing 9.3% of Cu

EA   Found: C 0.10, H 0.76, Cl 0.00, Cu 9.3, N, 0.00, Ti 48.5%.

N$_2$-Adsorption   Before mechanical treatment:

-Desorption   The BET surface area is 227 m^{2}g^{-1}, the pore volume is 0.273 cm^{3}g^{-1} and the average pore diameter is 3.5 nm obtained from the pore size distribution based on the BJH desorption branch (Fig. 6.3f).

After mechanical treatment:

The BET surface area is 243 m^{2}g^{-1}, the pore volume is 0.254 cm^{3}g^{-1} and the average pore diameter is 3.4 nm obtained from the pore size distribution based on the BJH desorption branch (Fig. 6.4f).

8.3. Catalytic Examinations

8.3.1. Hydrocarbon Selective Catalytic Reduction (HC-SCR) of Nitrogen Oxides

Catalytic measurements were performed on a fully computer-controlled microreactor system, as shown in Fig. 8.3. Standard experiments were carried out at atmospheric pressure using 800 mg of catalyst. C_3H_8 was used as a reducing agent. The samples were pretreated at 450 °C for 25 min. with a flow of He before measurements. The reactant gas mixture, containing 1000 ppm of NO_x, 1000 ppm of C_3H_8, 1000 ppm of O_2 and carrier gas He, was passed through the catalyst bed at a constant flow rate of 150 ml min^{-1}. Steady-state measurements of the temperature dependence of the catalytic activity were performed by raising the temperature from 250 to 650 °C in steps of 50 °C, with a typical duration of the isothermal steps of 30 min. The products were analyzed by CLD (NO and NO_x analyser), GC and MS.

8.3.2. Dehydrogenation of Benzyl Alcohol

Catalytic examination was performed in a gas-phase catalytic microreactor system as shown in Fig. 8.4. The gas-phase catalytic dehydrogenation of benzyl alcohol was conducted under atmospheric pressure using a continuous, U-shaped glass microreactor with ca.10 mm diameter. For each run about 1.6 g of the catalyst was loaded into the reactor, maintaining the reactant flow rate at 5 ml h^{-1}. N_2 was used as carrier gas at a constant flow rate of 60 ml min^{-1}. The catalytic experiments were performed at 523 K. The products were collected by a cooling system and analyzed by GC.
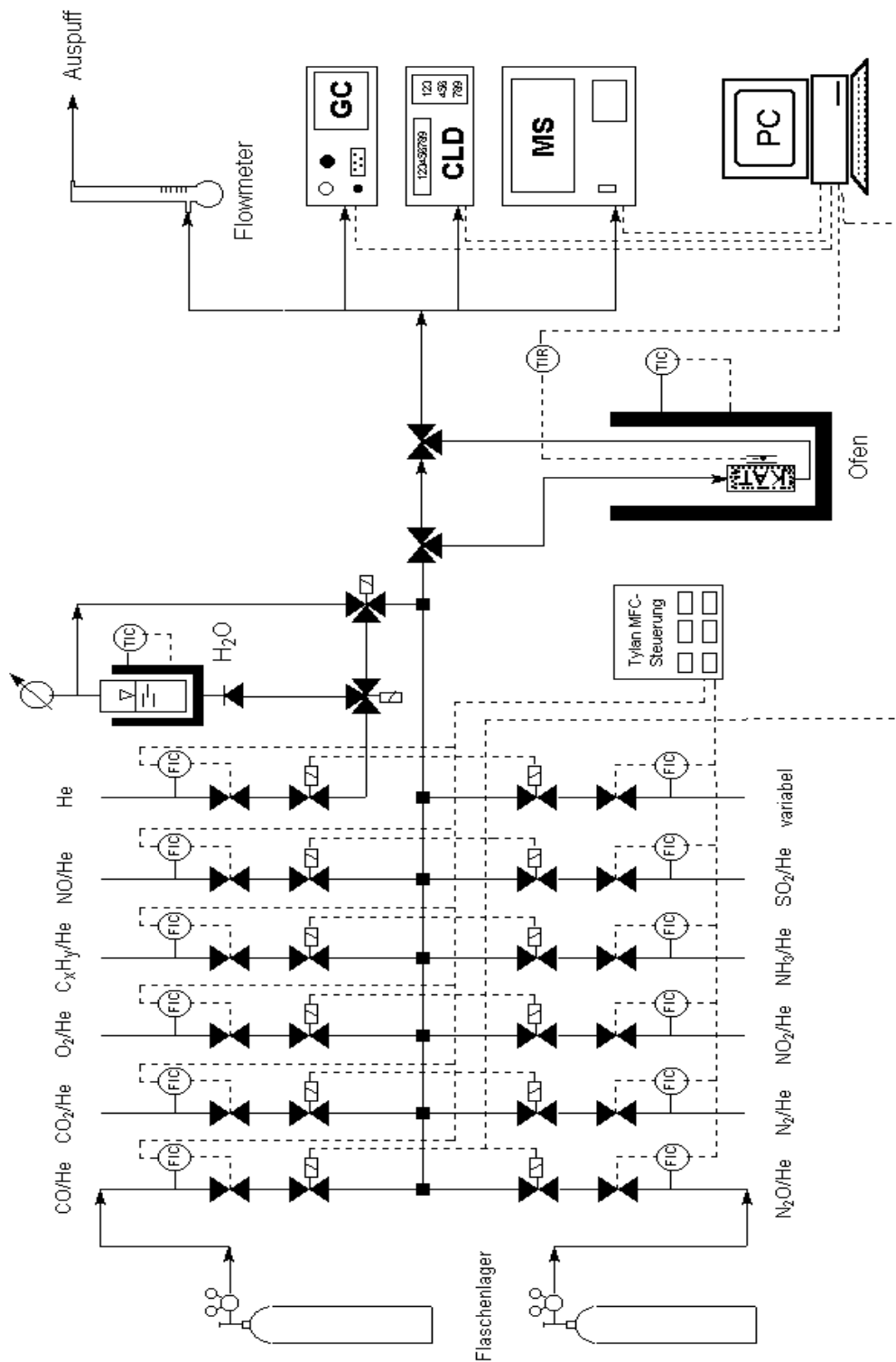
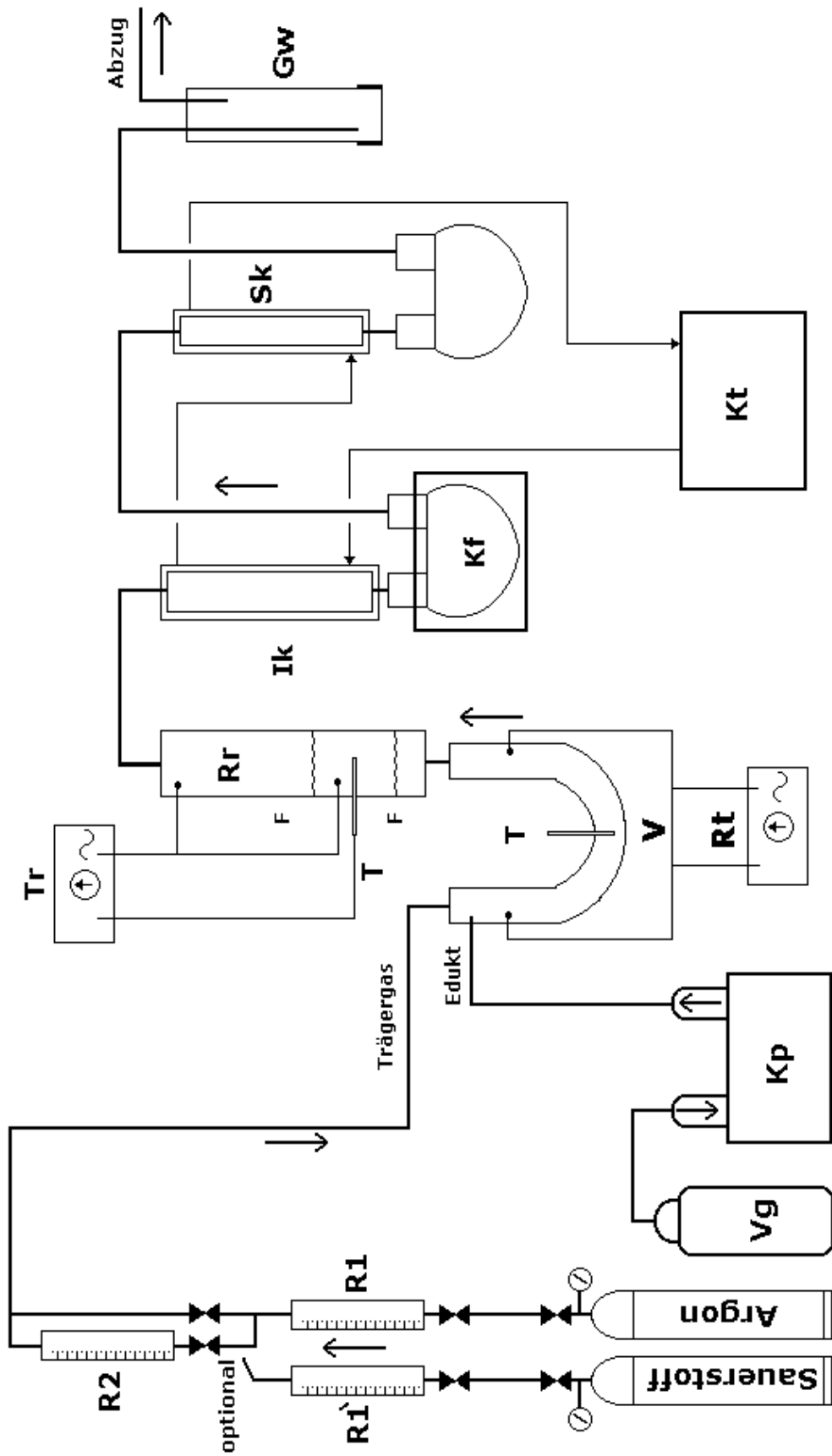**Figure 8.3** HC-SCR-DeNO$_x$ microreactor system.[3]

Figure 8.4 The gas-phase catalytic microreactor system.

References

1. K. S. W. Sing, *Adsorption: Science and Technology*, Eds. A. E. Rodrigues *et al*., Kluwer Academic Publishers, London, **1989**.

2. P. Schneider, *Appl. Catal. A*, **1995**, *129*, 157.

3. T. W. Bog, Ph.D thesis, Technischen Universität München, Germany, **1999**.

List of Publications:

(1) Mesoporous Titania Nanostructures Thermally Stabilized by Doping Sodium Oxide, Q. Li, P. Härter, W.-M. Xue, W. A. Herrmann, accepted by *Journal of Chemical Society, Dalton Transactions*, **2001**.

(2) Bimodal Mesoporous Alumina Molecular Sieves, Q. Li, P. Härter, W.-M. Xue, W. A. Herrmann, to be submitted to *Micro. And Meso*.

(3) Mesoporous Titanium Oxo Phosphate Thermally Stabilized by Polyphosphoric Acid, Q. Li, P. Härter, W.-M. Xue, W. A. Herrmann, to be submitted to *Chemistry of Materials*.

(4) Highly Thermal Stable Mesoporous Titanium Oxide Molecular Sieves, Q. Li, P. Härter, W.-M. Xue, and W. A. Herrmann, to be submitted to *Chemistry of Materials*.

(5) Synthesis, Characterization and Catalytic Application of Bimodal Mesoporous Aluminia, Q. Li, M. Gittar, P. Härter, W.-M. Xue, and W. A. Herrmann, , submitted to *Appl. Catal.*.

Curriculum Vitae

Name: Quanchang Li

Date of Birth: 27 January, 1965

Place of Birth: P. R. China

Nationality: P. R. China

Marriage Status: Married

                           wife: Dr. Wen-Mei Xue

                           son: David He Li

1973-1978:   Elementary School of Xi'an University of Technology in Xi'an, P. R. China

1978-1983:   Middle School of Xi'an University of Technology in Xi'an, P. R. China

1983-1987:   B.Sc., Department of Chemistry at Lanzhou University in Lanzhou,

                          P. R. China

1987-1990:   M.Sc., Department of Chemistry at Lanzhou University in Lanzhou,

                          P. R. China

1990-1998:   Chemical Engineer, Lanzhou Petroleum and Chemical Complex in

                          Lanzhou, P. R. China

1999-2001:   Ph.D., in the Group of Prof. Dr. Dr. h.c. mult. W. A. Herrmann,

                          Anorganisch-Chemisches Institut der Technischen Universität München in

                          Munich, Germany